

World Journal of *Radiology*

World J Radiol 2022 August 28; 14(8): 249-318



OPINION REVIEW

- 249 Augmenting prostate magnetic resonance imaging reporting to incorporate diagnostic recommendations based upon clinical risk calculators
Gupta K, Perchik JD, Fang AM, Porter KK, Rais-Bahrami S

MINIREVIEWS

- 256 Advanced magnetic resonance imaging findings in salivary gland tumors
Gökçe E, Beyhan M
- 272 Amebic liver abscess: Clinico-radiological findings and interventional management
Priyadarshi RN, Kumar R, Anand U
- 286 Progress in interventional radiology treatment of pulmonary embolism: A brief review
Posa A, Barbieri P, Mazza G, Tanzilli A, Iezzi R, Manfredi R, Colosimo C

ORIGINAL ARTICLE**Retrospective Study**

- 293 Imaging volumes during COVID-19: A Victorian health service experience
Pinson JA, Diep ML, Krishnan V, Aird C, Cooper C, Leong C, Chen J, Ardley N, Paul E, Badawy MK
- 311 Triple rule-out computed tomography angiography: Evaluation of acute chest pain in COVID-19 patients in the emergency department
Bahadir S, Aydın S, Kantarci M, Unver E, Karavas E, Şenbil DC

ABOUT COVER

Editorial Board Member of *World Journal of Radiology*, Alexander B Kononov, PhD, Associate Professor, Leading Scientist, Russian Federal Nuclear Center - Zababakhin Institute of Applied Physics, Snezninsk 456770, Russia. a_konov@mail.vega-int.ru

AIMS AND SCOPE

The primary aim of *World Journal of Radiology (WJR, World J Radiol)* is to provide scholars and readers from various fields of radiology with a platform to publish high-quality basic and clinical research articles and communicate their research findings online.

WJR mainly publishes articles reporting research results and findings obtained in the field of radiology and covering a wide range of topics including state of the art information on cardiopulmonary imaging, gastrointestinal imaging, genitourinary imaging, musculoskeletal imaging, neuroradiology/head and neck imaging, nuclear medicine and molecular imaging, pediatric imaging, vascular and interventional radiology, and women's imaging.

INDEXING/ABSTRACTING

The *WJR* is now abstracted and indexed in PubMed, PubMed Central, Emerging Sources Citation Index (Web of Science), Reference Citation Analysis, China National Knowledge Infrastructure, China Science and Technology Journal Database, and Superstar Journals Database. The 2022 edition of Journal Citation Reports® cites the 2021 Journal Citation Indicator (JCI) for *WJR* as 0.48.

RESPONSIBLE EDITORS FOR THIS ISSUE

Production Editor: Rui-Rui Wu, Production Department Director: Xu Guo, Editorial Office Director: Jia-Ping Yan.

NAME OF JOURNAL

World Journal of Radiology

ISSN

ISSN 1949-8470 (online)

LAUNCH DATE

January 31, 2009

FREQUENCY

Monthly

EDITORS-IN-CHIEF

Thomas J Vogl

EDITORIAL BOARD MEMBERS

<https://www.wjgnet.com/1949-8470/editorialboard.htm>

PUBLICATION DATE

August 28, 2022

COPYRIGHT

© 2022 Baishideng Publishing Group Inc

INSTRUCTIONS TO AUTHORS

<https://www.wjgnet.com/bpg/gerinfo/204>

GUIDELINES FOR ETHICS DOCUMENTS

<https://www.wjgnet.com/bpg/GerInfo/287>

GUIDELINES FOR NON-NATIVE SPEAKERS OF ENGLISH

<https://www.wjgnet.com/bpg/gerinfo/240>

PUBLICATION ETHICS

<https://www.wjgnet.com/bpg/GerInfo/288>

PUBLICATION MISCONDUCT

<https://www.wjgnet.com/bpg/gerinfo/208>

ARTICLE PROCESSING CHARGE

<https://www.wjgnet.com/bpg/gerinfo/242>

STEPS FOR SUBMITTING MANUSCRIPTS

<https://www.wjgnet.com/bpg/GerInfo/239>

ONLINE SUBMISSION

<https://www.f6publishing.com>

Augmenting prostate magnetic resonance imaging reporting to incorporate diagnostic recommendations based upon clinical risk calculators

Karisma Gupta, Jordan D Perchik, Andrew M Fang, Kristin K Porter, Soroush Rais-Bahrami

Specialty type: Radiology, nuclear medicine and medical imaging

Provenance and peer review: Invited article; Externally peer reviewed.

Peer-review model: Single blind

Peer-review report's scientific quality classification

Grade A (Excellent): 0
Grade B (Very good): 0
Grade C (Good): C, C
Grade D (Fair): 0
Grade E (Poor): 0

P-Reviewer: Andrejic-Visnjic B, Serbia; Liang L, China

Received: March 22, 2022

Peer-review started: March 22, 2022

First decision: June 16, 2022

Revised: June 27, 2022

Accepted: July 25, 2022

Article in press: July 25, 2022

Published online: August 28, 2022



Karisma Gupta, Department of Radiology, University of Washington, Seattle, WA 98195, United States

Jordan D Perchik, Kristin K Porter, Soroush Rais-Bahrami, Department of Radiology, University of Alabama at Birmingham, Birmingham, AL 35233, United States

Andrew M Fang, Soroush Rais-Bahrami, Department of Urology, University of Alabama at Birmingham, Birmingham, AL 35233, United States

Soroush Rais-Bahrami, O'Neal Comprehensive Cancer Center, University of Alabama at Birmingham, Birmingham, AL 35233, United States

Corresponding author: Soroush Rais-Bahrami, MD, Associate Professor, Departments of Urology and Radiology, University of Alabama at Birmingham, Faculty Office Tower 1107 510 20th Street South, Birmingham, AL 35233, United States. soroushraisbahrami@gmail.com

Abstract

Risk calculators have offered a viable tool for clinicians to stratify patients at risk of prostate cancer (PCa) and to mitigate the low sensitivity and specificity of screening prostate specific antigen (PSA). While initially based on clinical and demographic data, incorporation of multiparametric magnetic resonance imaging (MRI) and the validated prostate imaging reporting and data system suspicion scoring system has standardized and improved risk stratification beyond the use of PSA and patient parameters alone. Biopsy-naïve patients with lower risk profiles for harboring clinically significant PCa are often subjected to uncomfortable, invasive, and potentially unnecessary prostate biopsy procedures. Incorporating risk calculator data into prostate MRI reports can broaden the role of radiologists, improve communication with clinicians primarily managing these patients, and help guide clinical care in directing the screening, detection, and risk stratification of PCa.

Key Words: Prostatic adenocarcinoma; Multiparametric magnetic resonance imaging; Nomograms; Risk calculators; Biopsy

©The Author(s) 2022. Published by Baishideng Publishing Group Inc. All rights reserved.

Core Tip: Incorporating risk calculator data into prostate magnetic resonance imaging reports can broaden the role of radiologists, improve communication with clinicians primarily managing these patients, and help guide clinical care in directing the screening, detection, and risk stratification of prostate cancer.

Citation: Gupta K, Perchik JD, Fang AM, Porter KK, Rais-Bahrami S. Augmenting prostate magnetic resonance imaging reporting to incorporate diagnostic recommendations based upon clinical risk calculators. *World J Radiol* 2022; 14(8): 249-255

URL: <https://www.wjgnet.com/1949-8470/full/v14/i8/249.htm>

DOI: <https://dx.doi.org/10.4329/wjr.v14.i8.249>

INTRODUCTION

Prostate cancer (PCa) is the most common solid organ malignancy in American men and the second cause of cancer-related death in the United States[1]. Due to increased awareness, nearly 20 million men in the United States engage in screening and early detection discussions (National Comprehensive Cancer Network). Prostate specific antigen (PSA) made large-scale screening for PCa feasible, but lacked accuracy, with 15%-25% false negatives and 60% false positives[2,3]. Since PSA has proven to be an unreliable biomarker for clinically significant prostate cancer [csPCa; Grade Group (GG) \geq 2], a large percentage of patients continue to undergo prostate biopsies with either benign or clinically indolent PCa (GG 1). Prostate biopsies are an invasive diagnostic procedure with well-established risks, such as hematuria, hemospermia, rectal bleeding, urinary tract infections, and recognized risk of sepsis[4-7]. Furthermore, potentially unnecessary biopsies and over treatment of low-risk prostate cancer has placed an undue psychological burden on patients[8].

The role of multiparametric magnetic resonance imaging (mpMRI) in prostate cancer diagnosis, surveillance, and treatment has significantly evolved and is growing in popularity as a tool to potentially avoid unnecessary biopsies in biopsy-naive patients. Controversy remains due to significant variability across patient cohorts and institutions. Risk calculators combining mpMRI with clinical variables can limit this variation and have been shown to improve predictive models[9,10]. An individualized screening algorithm using a patient's clinical history can result in a considerable reduction in unnecessary biopsy sessions. A validated clinical risk calculator that could be incorporated into MRI reporting and aid in the decision to pursue prostate biopsies in biopsy-naive patients is needed[11]. However, such a risk calculator must be carefully validated to ensure its reliable performance and applicability to a broad population of patients undergoing prostate cancer screening when including MRI in the screening algorithm.

OVERVIEW OF RISK CALCULATORS

Historical perspective

One of the first algorithms to predict the risk of prostate cancer on prostate biopsy was the European Randomized Study for Screening of Prostate Cancer (ERSPC) risk calculator. The ERSPC has six calculators, two of which are used by patients and the remaining four used by physicians. The RC3/RC4 combined calculator uses PSA levels, digital rectal exam (DRE) exam, previous prostate biopsy history, prostate volume, and now incorporates MRI prostate imaging reporting and data system (PI-RADS) v 1.0 score to predict the detectable risk of prostate cancer on biopsy. The calculator stratifies the risk of detecting cancer to assist clinicians with the decision to pursue biopsy (<https://www.prostatecancer-riskcalculator.com/>). Several external validation studies have been performed for these RCs. The discriminative ability of detecting positive prostate biopsy (PBx) in biopsy-naive or previously biopsied patients using the ERSPC RC3 or RC4 was assessed, showing area under the curve (AUC) values in the range of 0.71-0.88[12-16].

Thompson *et al*[17] developed one of the first online individualized predictive assessments of prostate cancer before prostate biopsy extrapolated from the 5519 patients in the Prostate Cancer Prevention Trial (PCPT). It was found that PSA, family history, DRE findings, African American race, and history of a prior negative prostate biopsy provided independent predictive value to the calculation of risk of a biopsy that showed presence of cancer. The first calculator became known as the Prostate Cancer Prevention Trial Risk Calculator (PCPTRC) and has been used widely online at <https://riskcalc.org/PCPTRC/>. In 2012, an updated PCPTRC 2.0 was released with the added capability to provide prediction of indolent low-grade (Gleason grade $<$ 7) vs high-grade (GG \geq 2) PCa. Both versions of the online PCPT risk calculator were externally validated in 2014.

Independent validation and comparisons between the ERSPC and PCPTRC calculators demonstrated comparable calibration in their agreement between predicted and observed risks of prostate cancer. However, the AUC for predicting clinically significant sPCa was higher for the ERSPC risk calculator compared with the PCPTRC (0.73 *vs* 0.70; $P = 0.043$)[18]. The PCPTRC has been replaced by a more contemporary risk calculator developed by the Prostate Biopsy Collaborative Group (PBCG) that incorporates age, PSA level, DRE results, family history, race, and a history of negative biopsy along with more contemporary biopsy schemes[19]. The study demonstrates a greater inclusion of patients with diverse backgrounds and PBCG model outperformed the PCPTRC in predicting csPCa on both internal (AUC, 75.5% *vs* 72.3%; $P < 0.0001$) and external validation (AUC, 72.9% *vs* 69.7%; $P < 0.0001$). Furthermore, the PBCG model was found to be well calibrated and offered a higher net clinical benefit than the PCPT risk calculator: it led to 2.7% fewer biopsies without missing any csPCa.

Advent of imaging

Prior to 2017, mpMRI of the prostate was not commonly used in the PCa workup worldwide due to the high cost and limited availability of prostate MRI. In 2019, Alberts *et al*[20] published a study on the use of risk calculators and biopsy results to avoid unnecessary prostate MRI. Alberts *et al*[20] suggested that mpMRI of the prostate provided an opportunity to enhance the non-invasive portion of the PCa workup and introduced a nomogram integrating PI-RADS data into the ERSPC risk calculator. Alberts *et al*[20] demonstrated a superior nomogram compared to the ERSPC standard, achieving an AUC of 0.84, which was significantly increased compared to ERSPC calculators that did not incorporate imaging data.

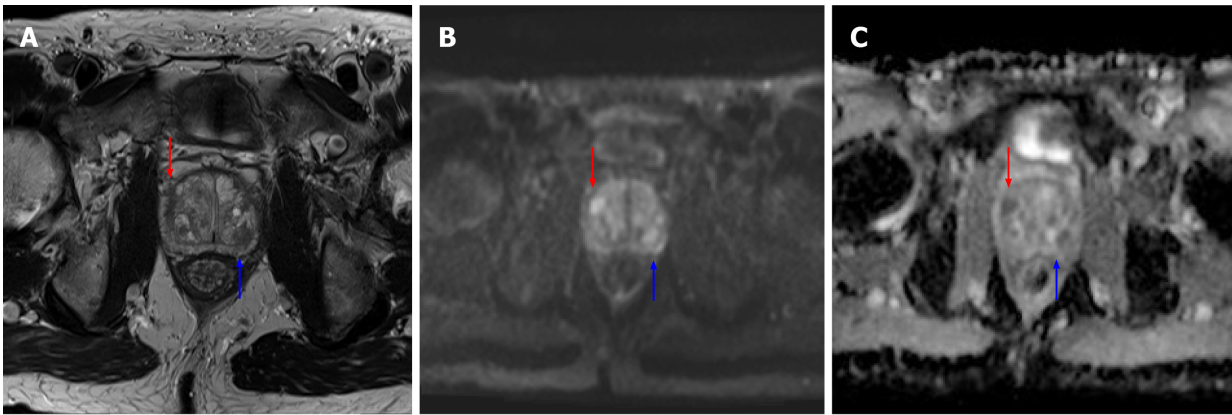
As mpMRI of the prostate became more widely available and the Urology community became more aware of the potential impact of PI-RADS score on risk calculator development, prostate MRI data was more widely incorporated into PCa risk nomograms. PI-RADS data, scored on a zero to five Likert scale, is easily incorporated into nomograms due to its objective, defined numerical values. In 2019, Alberts *et al*[20] refined the ERSPC-RC-3/4 risk calculators, developing MRI-ERSPC-RC-3/4 by adding mpMRI examination results. The addition of MRI to the ERSPC calculators increased the discriminative ability for high-grade PCa [AUC of 0.84 (95% CI 0.81-0.88) and 0.85 (95% CI 0.81-0.89) for the MRI-ERSPC-RC3 and MRI-ERSPC-RC4, respectively][20]. Beyond the established clinical based calculators like the ERSPC and the PBCG, novel risk calculators were developed across the globe, with several large multicenter trials occurring in North America, the United Kingdom, and Australia, such as the Stanford Prostate Cancer Calculator (SPCC)[21], the PLUM cohort[22], the PCRC-MRI[23], MRI study by Chau *et al*[24], and the study done by van Leeuwen *et al*[25] PI-RADS integrated clinical calculators consistently demonstrated superior performance to calculators using clinical data alone[23-27]. Of note, due to the wide variety in study location, practice type, and timing of data collection, some of these risk calculators use data from PI-RADS v1.0 and PI-RADS 2.0. The SPCC notes that its calculator is validated for both PI-RADS v1.0 and v2.0[21].

For biopsy-naive patients, the superior performance of imaging integrated risk calculators represents a possibility to avoid invasive biopsy for low risk PCa. Trials specific to the biopsy-naive population have demonstrated promising results with high sensitivity and specificity and high net benefit. Radtke *et al*[27] and Chau *et al*[24] attained high AUC values, both in excess of 0.8, and both were trained on patient populations from the United Kingdom. The van Leeuwen *et al*'s risk calculator has an AUC of 0.90 and demonstrates one of the most substantial net benefits, avoiding 28.6% of biopsies at 10% risk tolerance, missing only 2.6% of PCa[25]. Additional external validation studies have demonstrated high AUC for the van Leeuwen and ERSPC based models, however both studies conclude that the use of MRI integrated risk calculators to avoid biopsy remains controversial[28,29].

DISCUSSION

Risk calculators and nomograms provide a valuable tool in risk stratification of patients with abnormal screening PSA levels potentially allowing selection of cases to avoid biopsy in patients at low risk for harboring csPCa. Incorporation of risk calculator data into radiology reports could represent an opportunity for radiologists to add value to the patient evaluation and mitigate ambiguity of borderline results, especially PI-RADS 3 Lesions found on prostate indication MRI studies (Figures 1 and 2). In collaboration with the referring clinician, the radiologist could incorporate patient clinic and demographic information, along with the lesion PI-RADS score, calculate the percent risk of csPCa, and include this information in the final diagnostic imaging report.

Three PI-RADS integrated calculators, the SPCC[21], the PLUM Prostate cancer risk calculator, and the MRI-ERSPC-R-3/4 published open access online calculators, allowing a more streamlined integration into workflow. For biopsy-naive patients, the PLUM calculator demonstrated the highest sensitivity and specificity with an AUC value of 0.87 and a net benefit of avoiding 18.1% of biopsies without missing any csPCa in biopsy-naive patients at a 15% tolerance. The MRI-ERSPC-R-3/4 calculator reported an AUC of 0.84 in its initial study from Alberts *et al*'s net benefit for biopsy-naive patients was not reported in the Alberts *et al*'s study[20], but in Petersmann *et al*[29], which compared the MRI-ERSPC-R-3/4 calculator to the calculator described in van Leeuwen *et al*[25], the MRI/ERSPC-



DOI: 10.4329/wjr.v14.i8.249 Copyright ©The Author(s) 2022.

Figure 1 Axial magnetic resonance imaging images of the prostate. A: T2 weighted image; B: b1200 diffusion weighted imaging (DWI) image; C: Calculated apparent dispersion coefficient (ADC) image. A mostly encapsulated T2-hypointense transitional zone lesion is demonstrated in the left posterior central gland, measuring 10 mm (blue arrows) with focal moderate low ADC, high DWI signal, designated prostate imaging reporting and data system (PI-RADS) 3 per PI-RADS version 2.1. An additional 8 mm PI-RADS 4 Lesion of the anterior right transitional zone is present (red arrow), demonstrating non-circumscribed moderate T2 hypointensity and marked focal ADC hypointensity and DWI hyperintensity.

PROSTATE:

Focal lesion(s): []
 Lesion # 1 (index lesion):
 Key image: image [] series []
 Size: [] mm
 Location: [] [] [] []
 T2WI: [] DWI: [] DCE (early and focal enhancement): []
 PI-RADS v2.1 score: []
 Likelihood of extraprostatic extension: [] []
 Likelihood of seminal vesicle invasion: [] []
 Diffuse prostate abnormalities: []
 Other prostate findings: [None]

RISK CALCULATOR:

Prostate Volume: []
 PSA: []
 PSA density: []
 Clinical data (DRE, family history, prior biopsy, etc): [] []
 Demographic information: []
 PIRADS v2.1 score: []

% risk of csPCa: []
 Recommendation: []

DOI: 10.4329/wjr.v14.i8.249 Copyright ©The Author(s) 2022.

Figure 2 Sample structured report for prostate lesion reporting with integrated risk calculator reporting. The calculated percent risk of clinically significant prostate cancer is included in the lesion evaluation findings with recommendations for biopsy or observation in the conclusion. csPCa: Clinically significant prostate cancer; DRE: Digital rectal exam; DWI: Diffusion weighted imaging; PI-RADS: Prostate imaging reporting and data system; PSA: Prostate specific antigen.

R-3/4 nomogram avoids only 9% of biopsies in biopsy-naive patients while missing 3% at a 15% risk threshold. The SPCC trial did not report a specific AUC or net benefit for biopsy-naive patients but reported AUC values ranging from 0.78-0.83 and a net benefit of avoiding 10.3% of biopsies while missing csPCa in 0.8% of patients with a risk tolerance of 20% [21].

Additional notable nomograms have demonstrated promising results for biopsy-naive patients that outperform some of the larger and more established risk calculators. The van Leeuwen *et al* [25] nomogram demonstrated the highest AUC of all evaluated risk calculators and reported one of the highest net benefits, avoiding 28.6% of biopsies while missing only 2.6% of csPCa, but was developed on a smaller and more homogenous patient population (393 patients from Australia) than many of the other noted calculators. However in the external validation study by Petersmann *et al* [29], the van Leeuwen nomogram was demonstrated to maintain high performance, and even outperformed the ERSPC in net benefit. Petersmann *et al* [29] compared ERSPC and van Leeuwen risk calculator. This study showed comparable AUC values between the two studies, 0.81 for ERSPC and 0.82 for van Leeuwen, however the van Leeuwen calculator demonstrated a greater net benefit from a risk threshold

of 10%-15%, avoiding 24% of biopsies while missing 6% of csPCa, compared to 14% and 5% for the MRI-ERSP-RC-3/4, respectively. Notably the ERSPC calculator had a near perfect calibration, with a calibration slope of 0.94 compared to the van Leeuwen model, 0.70. The Petersmann *et al*'s study population came from a hospital system in Nuremberg, Germany and likely reflected a similar demographic to the ERSPC training population, whereas the van Leeuwen study was performed in Australia[29]. The gaps in calibration between these two studies may indicate future pitfalls in generalizability, and clinicians need to be aware of the training data and population demographics when applying these calculators to their own patient population.

Novel imaging technologies such as prostate cancer directed PET imaging may further aid in refining these risk calculators, allowing for additional improvements in pre-biopsy patient risk stratification. Radiomics, a subset of clinical artificial intelligence (AI), is a promising tool on the horizon of prostate imaging and prostate cancer classification. Prostate MRI has represented a prolific area of AI research in the past decade, with algorithms demonstrating improved prostate cancer detection, classification, and upstream applications, such as deep learning reconstruction and its role in instituting abbreviated protocols. In a systematic review, Ferro *et al*[30] discuss 21 manuscripts related to radiomics and the detection of csPCa. These publications have demonstrated the capability of radiomics to extract salient features and develop models that predict csPCa that significantly outperform clinical models[31] and combined clinical and imaging models[32]. While these results are encouraging, the algorithms to date are often trained at a single institution and are limited by a lack of external validation and heterogeneity of the extracted radiomics features. Although further refinement and broader, multi-institution testing is needed, early successes of radiomics models suggest a promising future for AI in the evaluation, diagnosis, risk stratification, and treatment decision making in the management of csPCa.

CONCLUSION

Risk calculators have enabled physicians and patients to make a more informed decision when considering pursuit of a prostate biopsy. When evaluating biopsy-naïve patients, multiple risk calculators can be applied, each with their own strengths. The role of imaging using MRI in the diagnosis of csPCa has significantly evolved and is growing in popularity. The PI-RADS system has become a component of many currently available pre-biopsy prostate cancer risk calculators. Artificial intelligence shows promise in further advancing the role of imaging in csPCa risk assessment. Further incorporation of imaging in clinical risk calculators shows promise in aiding the decision to pursue prostate biopsies with improved confidence and patient-centric goals.

FOOTNOTES

Author contributions: Porter KK and Rais-Bahrami S contributed equally to this work; Porter KK and Rais-Bahrami S designed the study; Gupta K, Perchik JD, Fang AM, Porter KK, and Rais-Bahrami S contributed to authoring the manuscript and critically reviewing and revising the manuscript; all authors have read and approved the final manuscript.

Conflict-of-interest statement: Rais-Bahrami S serves as a consultant to Philips/InVivo Corp, Genomic Health Inc, Blue Earth Diagnostics, Bayer Healthcare, UroViu Corp, and Intuitive Surgical.

Open-Access: This article is an open-access article that was selected by an in-house editor and fully peer-reviewed by external reviewers. It is distributed in accordance with the Creative Commons Attribution NonCommercial (CC BY-NC 4.0) license, which permits others to distribute, remix, adapt, build upon this work non-commercially, and license their derivative works on different terms, provided the original work is properly cited and the use is non-commercial. See: <https://creativecommons.org/licenses/by-nc/4.0/>

Country/Territory of origin: United States

ORCID number: Andrew M Fang 0000-0002-2390-7575; Soroush Rais-Bahrami 0000-0001-9466-9925.

S-Editor: Gong ZM

L-Editor: A

P-Editor: Gong ZM

REFERENCES

- 1 Siegel RL, Miller KD, Fuchs HE, Jemal A. Cancer Statistics, 2021. *CA Cancer J Clin* 2021; **71**: 7-33 [PMID: 33433946 DOI: 10.3322/caac.21654]

- 2 **Gambert SR.** Screening for prostate cancer. *Int Urol Nephrol* 2001; **33**: 249-257 [PMID: [12092637](#) DOI: [10.1023/a:1015290429403](#)]
- 3 **Thompson IM, Pauler DK, Goodman PJ, Tangen CM, Lucia MS, Parnes HL, Minasian LM, Ford LG, Lippman SM, Crawford ED, Crowley JJ, Coltman CA Jr.** Prevalence of prostate cancer among men with a prostate-specific antigen level < or =4.0 ng per milliliter. *N Engl J Med* 2004; **350**: 2239-2246 [PMID: [15163773](#) DOI: [10.1056/NEJMoa031918](#)]
- 4 **Halpern JA, Sedrakyan A, Dinerman B, Hsu WC, Mao J, Hu JC.** Indications, Utilization and Complications Following Prostate Biopsy: New York State Analysis. *J Urol* 2017; **197**: 1020-1025 [PMID: [27856226](#) DOI: [10.1016/j.juro.2016.11.081](#)]
- 5 **Loeb S, Carter HB, Berndt SI, Ricker W, Schaeffer EM.** Complications after prostate biopsy: data from SEER-Medicare. *J Urol* 2011; **186**: 1830-1834 [PMID: [21944136](#) DOI: [10.1016/j.juro.2011.06.057](#)]
- 6 **Loeb S, Vellekoop A, Ahmed HU, Catto J, Emberton M, Nam R, Rosario DJ, Scattoni V, Lotan Y.** Systematic review of complications of prostate biopsy. *Eur Urol* 2013; **64**: 876-892 [PMID: [23787356](#) DOI: [10.1016/j.eururo.2013.05.049](#)]
- 7 **Ravi P, Sammon J, Meskawi M, Sun M, Karakiewicz PI, Trinh QD.** Re: Complications after prostate biopsy: data from SEER-Medicare: S. Loeb, H. B. Carter, S. I. Berndt, W. Ricker and E. M. Schaeffer *J Urol* 2011; **186**: 1830-1834. *J Urol* 2012; **188**: 677-678 [PMID: [22704450](#) DOI: [10.1016/j.juro.2012.04.021](#)]
- 8 **Loeb S, Bjurlin MA, Nicholson J, Tammela TL, Penson DF, Carter HB, Carroll P, Etzioni R.** Overdiagnosis and overtreatment of prostate cancer. *Eur Urol* 2014; **65**: 1046-1055 [PMID: [24439788](#) DOI: [10.1016/j.eururo.2013.12.062](#)]
- 9 **Bjurlin MA, Rosenkrantz AB, Sarkar S, Lepor H, Huang WC, Huang R, Venkataraman R, Taneja SS.** Prediction of Prostate Cancer Risk Among Men Undergoing Combined MRI-targeted and Systematic Biopsy Using Novel Pre-biopsy Nomograms That Incorporate MRI Findings. *Urology* 2018; **112**: 112-120 [PMID: [29155186](#) DOI: [10.1016/j.urology.2017.09.035](#)]
- 10 **Radtke JP, Wiesenfarth M, Kesck C, Freitag MT, Alt CD, Celik K, Distler F, Roth W, Wieczorek K, Stock C, Duensing S, Roethke MC, Teber D, Schlemmer HP, Hohenfellner M, Bonekamp D, Hadaschik BA.** Combined Clinical Parameters and Multiparametric Magnetic Resonance Imaging for Advanced Risk Modeling of Prostate Cancer-Patient-tailored Risk Stratification Can Reduce Unnecessary Biopsies. *Eur Urol* 2017; **72**: 888-896 [PMID: [28400169](#) DOI: [10.1016/j.eururo.2017.03.039](#)]
- 11 **Fang AM, Rais-Bahrami S.** Magnetic resonance imaging-based risk calculators optimize selection for prostate biopsy among biopsy-naive men. *Cancer* 2022; **128**: 25-27 [PMID: [34427940](#) DOI: [10.1002/cncr.33872](#)]
- 12 **Cavadas V, Osório L, Sabell F, Teves F, Branco F, Silva-Ramos M.** Prostate cancer prevention trial and European randomized study of screening for prostate cancer risk calculators: a performance comparison in a contemporary screened cohort. *Eur Urol* 2010; **58**: 551-558 [PMID: [20580483](#) DOI: [10.1016/j.eururo.2010.06.023](#)]
- 13 **Gayet M, Mannaerts CK, Nieboer D, Beerlage HP, Wijkstra H, Mulders PFA, Roobol MJ.** Prediction of Prostate Cancer: External Validation of the ERSPC Risk Calculator in a Contemporary Dutch Clinical Cohort. *Eur Urol Focus* 2018; **4**: 228-234 [PMID: [28753781](#) DOI: [10.1016/j.euf.2016.07.007](#)]
- 14 **Trottier G, Roobol MJ, Lawrentschuk N, Boström PJ, Fernandes KA, Finelli A, Chadwick K, Evans A, van der Kwast TH, Toi A, Zlotta AR, Fleshner NE.** Comparison of risk calculators from the Prostate Cancer Prevention Trial and the European Randomized Study of Screening for Prostate Cancer in a contemporary Canadian cohort. *BJU Int* 2011; **108**: E237-E244 [PMID: [21507190](#) DOI: [10.1111/j.1464-410X.2011.10207.x](#)]
- 15 **van Vugt HA, Roobol MJ, Kranse R, Määttänen L, Finne P, Hugosson J, Bangma CH, Schröder FH, Steyerberg EW.** Prediction of prostate cancer in unscreened men: external validation of a risk calculator. *Eur J Cancer* 2011; **47**: 903-909 [PMID: [21163642](#) DOI: [10.1016/j.ejca.2010.11.012](#)]
- 16 **Yoon DK, Park JY, Yoon S, Park MS, Moon du G, Lee JG, Schröder FH.** Can the prostate risk calculator based on Western population be applied to Asian population? *Prostate* 2012; **72**: 721-729 [PMID: [21837777](#) DOI: [10.1002/pros.21475](#)]
- 17 **Thompson IM, Ankerst DP, Chi C, Goodman PJ, Tangen CM, Lucia MS, Feng Z, Parnes HL, Coltman CA Jr.** Assessing prostate cancer risk: results from the Prostate Cancer Prevention Trial. *J Natl Cancer Inst* 2006; **98**: 529-534 [PMID: [16622122](#) DOI: [10.1093/jnci/djj131](#)]
- 18 **Poyet C, Nieboer D, Bhandi B, Kulkarni GS, Wiederkehr C, Wettstein MS, Largo R, Wild P, Sulser T, Hermanns T.** Prostate cancer risk prediction using the novel versions of the European Randomised Study for Screening of Prostate Cancer (ERSPC) and Prostate Cancer Prevention Trial (PCPT) risk calculators: independent validation and comparison in a contemporary European cohort. *BJU Int* 2016; **117**: 401-408 [PMID: [26332503](#) DOI: [10.1111/bju.13314](#)]
- 19 **Ankerst DP, Straubinger J, Selig K, Guerrios L, De Hoedt A, Hernandez J, Liss MA, Leach RJ, Freedland SJ, Kattan MW, Nam R, Haese A, Montorsi F, Boorjian SA, Cooperberg MR, Poyet C, Vertosick E, Vickers AJ.** A Contemporary Prostate Biopsy Risk Calculator Based on Multiple Heterogeneous Cohorts. *Eur Urol* 2018; **74**: 197-203 [PMID: [29778349](#) DOI: [10.1016/j.eururo.2018.05.003](#)]
- 20 **Alberts AR, Roobol MJ, Verbeek JFM, Schoots IG, Chiu PK, Osses DF, Tijsterman JD, Beerlage HP, Mannaerts CK, Schimmöller L, Albers P, Arsov C.** Prediction of High-grade Prostate Cancer Following Multiparametric Magnetic Resonance Imaging: Improving the Rotterdam European Randomized Study of Screening for Prostate Cancer Risk Calculators. *Eur Urol* 2019; **75**: 310-318 [PMID: [30082150](#) DOI: [10.1016/j.eururo.2018.07.031](#)]
- 21 **Wang NN, Zhou SR, Chen L, Tibshirani R, Fan RE, Ghanouni P, Thong AE, To'o KJ, Ghabili K, Nix JW, Gordetsky JB, Sprengle P, Rais-Bahrami S, Sonn GA.** The stanford prostate cancer calculator: Development and external validation of online nomograms incorporating PIRADS scores to predict clinically significant prostate cancer. *Urol Oncol* 2021; **39**: 831.e19-831.e27 [PMID: [34247909](#) DOI: [10.1016/j.urolonc.2021.06.004](#)]
- 22 **Patel HD, Koehne EL, Shea SM, Bhanji Y, Gerena M, Gorbonos A, Quek ML, Flanigan RC, Goldberg A, Gupta GN.** Risk of prostate cancer for men with prior negative biopsies undergoing magnetic resonance imaging compared with biopsy-naive men: A prospective evaluation of the PLUM cohort. *Cancer* 2022; **128**: 75-84 [PMID: [34427930](#) DOI: [10.1002/cncr.33875](#)]
- 23 **Kinnaird A, Brisbane W, Kwan L, Priester A, Chuang R, Barsa DE, Delfin M, Sisk A, Margolis D, Felker E, Hu J, Marks LS.** A prostate cancer risk calculator: Use of clinical and magnetic resonance imaging data to predict biopsy outcome in North American men. *Can Urol Assoc J* 2022; **16**: E161-E166 [PMID: [34672937](#) DOI: [10.5489/auaj.7380](#)]

- 24 **Chau EM**, Russell B, Santaolalla A, van Hemelrijck M, McCracken S, Page T, Liyanage SH, Aning J, Gnanapragasam VJ, Acher P. MRI-based nomogram for the prediction of prostate cancer diagnosis: A multi-centre validated patient-physician decision tool. *J Clin Urol* 2022; E-Pub ahead of Print [DOI: [10.1177/20514158211065949](https://doi.org/10.1177/20514158211065949)]
- 25 **van Leeuwen PJ**, Hayen A, Thompson JE, Moses D, Shnier R, Böhm M, Abuodha M, Haynes AM, Ting F, Barentsz J, Roobol M, Vass J, Rasiah K, Delprado W, Stricker PD. A multiparametric magnetic resonance imaging-based risk model to determine the risk of significant prostate cancer prior to biopsy. *BJU Int* 2017; **120**: 774-781 [PMID: [28207981](https://pubmed.ncbi.nlm.nih.gov/28207981/) DOI: [10.1111/bju.13814](https://doi.org/10.1111/bju.13814)]
- 26 **Mehralivand S**, Shih JH, Rais-Bahrami S, Oto A, Bednarova S, Nix JW, Thomas JV, Gordetsky JB, Gaur S, Harmon SA, Siddiqui MM, Merino MJ, Parnes HL, Wood BJ, Pinto PA, Choyke PL, Turkbey B. A Magnetic Resonance Imaging-Based Prediction Model for Prostate Biopsy Risk Stratification. *JAMA Oncol* 2018; **4**: 678-685 [PMID: [29470570](https://pubmed.ncbi.nlm.nih.gov/29470570/) DOI: [10.1001/jamaoncol.2017.5667](https://doi.org/10.1001/jamaoncol.2017.5667)]
- 27 **Radtke JP**, Giganti F, Wiesenfarth M, Stabile A, Marengo J, Orczyk C, Kasivisvanathan V, Nyarangi-Dix JN, Schütz V, Dieffenbacher S, Görtz M, Stenzinger A, Roth W, Freeman A, Punwani S, Bonekamp D, Schlemmer HP, Hohenfellner M, Emberton M, Moore CM. Prediction of significant prostate cancer in biopsy-naïve men: Validation of a novel risk model combining MRI and clinical parameters and comparison to an ERSPC risk calculator and PI-RADS. *PLoS One* 2019; **14**: e0221350 [PMID: [31450235](https://pubmed.ncbi.nlm.nih.gov/31450235/) DOI: [10.1371/journal.pone.0221350](https://doi.org/10.1371/journal.pone.0221350)]
- 28 **Mannaerts CK**, Gayet M, Verbeek JF, Engelbrecht MRW, Savci-Heijink CD, Jager GJ, Gielens MPM, van der Linden H, Beerlage HP, de Reijke TM, Wijkstra H, Roobol MJ. Prostate Cancer Risk Assessment in Biopsy-naïve Patients: The Rotterdam Prostate Cancer Risk Calculator in Multiparametric Magnetic Resonance Imaging-Transrectal Ultrasound (TRUS) Fusion Biopsy and Systematic TRUS Biopsy. *Eur Urol Oncol* 2018; **1**: 109-117 [PMID: [31100233](https://pubmed.ncbi.nlm.nih.gov/31100233/) DOI: [10.1016/j.euo.2018.02.010](https://doi.org/10.1016/j.euo.2018.02.010)]
- 29 **Petersmann AL**, Remmers S, Klein T, Manava P, Huettenbrink C, Pahernik SA, Distler FA. External validation of two MRI-based risk calculators in prostate cancer diagnosis. *World J Urol* 2021; **39**: 4109-4116 [PMID: [34169337](https://pubmed.ncbi.nlm.nih.gov/34169337/) DOI: [10.1007/s00345-021-03770-x](https://doi.org/10.1007/s00345-021-03770-x)]
- 30 **Ferro M**, de Cobelli O, Vartolomei MD, Lucarelli G, Crocetto F, Barone B, Sciarra A, Del Giudice F, Muto M, Maggi M, Carrieri G, Busetto GM, Falagarì U, Terracciano D, Cormio L, Musi G, Tataru OS. Prostate Cancer Radiogenomics-From Imaging to Molecular Characterization. *Int J Mol Sci* 2021; **22** [PMID: [34576134](https://pubmed.ncbi.nlm.nih.gov/34576134/) DOI: [10.3390/ijms22189971](https://doi.org/10.3390/ijms22189971)]
- 31 **Li M**, Chen T, Zhao W, Wei C, Li X, Duan S, Ji L, Lu Z, Shen J. Radiomics prediction model for the improved diagnosis of clinically significant prostate cancer on biparametric MRI. *Quant Imaging Med Surg* 2020; **10**: 368-379 [PMID: [32190563](https://pubmed.ncbi.nlm.nih.gov/32190563/) DOI: [10.21037/qims.2019.12.06](https://doi.org/10.21037/qims.2019.12.06)]
- 32 **Deniffel D**, Abraham N, Namdar K, Dong X, Salinas E, Milot L, Khalvati F, Haider MA. Using decision curve analysis to benchmark performance of a magnetic resonance imaging-based deep learning model for prostate cancer risk assessment. *Eur Radiol* 2020; **30**: 6867-6876 [PMID: [32591889](https://pubmed.ncbi.nlm.nih.gov/32591889/) DOI: [10.1007/s00330-020-07030-1](https://doi.org/10.1007/s00330-020-07030-1)]

Advanced magnetic resonance imaging findings in salivary gland tumors

Erkan Gökçe, Murat Beyhan

Specialty type: Radiology, nuclear medicine and medical imaging

Provenance and peer review: Invited article; Externally peer reviewed.

Peer-review model: Single blind

Peer-review report's scientific quality classification

Grade A (Excellent): 0
Grade B (Very good): B
Grade C (Good): C
Grade D (Fair): 0
Grade E (Poor): 0

P-Reviewer: Kurokawa R, Japan;
Wang WCY, Taiwan

Received: January 12, 2022

Peer-review started: January 12, 2022

First decision: March 16, 2022

Revised: March 22, 2022

Accepted: August 7, 2022

Article in press: August 7, 2022

Published online: August 28, 2022



Erkan Gökçe, Murat Beyhan, Department of Radiology, Faculty of Medicine, Tokat Gaziosmanpasa University, Tokat 60100, Turkey

Corresponding author: Erkan Gökçe, MD, Professor, Department of Radiology, Faculty of Medicine, Tokat Gaziosmanpasa University, Kaleardı Neighborhood, Muhittin Fisunoglu Street, Tokat 60100, Turkey. drerkangokce@gmail.com

Abstract

Salivary gland tumors (SGTs) make up a small portion (approximately 5%) of all head and neck tumors. Most of them are located in the parotid glands, while they are less frequently located in the submandibular glands, minor salivary glands or sublingual gland. The incidence of malignant or benign tumors (BTs) in the salivary glands varies according to the salivary gland from which they originate. While most of those detected in the parotid gland tend to be benign, the incidence of malignancy increases in other glands. The use of magnetic resonance imaging (MRI) in the diagnosis of SGTs is increasing every day. While conventional sequences provide sufficient data on the presence, localization, extent and number of the tumor, they are insufficient for tumor specification. With the widespread use of advanced techniques such as diffusion-weighted imaging, semi-quantitative and quantitative perfusion MRI, studies and data have been published on the differentiation of malignant or BTs and the specificity of their subtypes. With diffusion MRI, differentiation can be made by utilizing the cellularity and microstructural properties of tumors. For example, SGTs such as high cellular Warthin's tumor (WT) or lymphoma on diffusion MRI have been reported to have significantly lower apparent diffusion values than other tumors. Contrast agent uptake and wash-out levels of tumors can be detected with semi-quantitative perfusion MRI. For example, it is reported that almost all of the pleomorphic adenomas show an increasing enhancement time intensity curve and do not wash-out. On quantitative perfusion MRI studies using perfusion parameters such as K_{trans} , K_{ep} , and V_e , it is reported that WTs can show higher K_{ep} and lower V_e values than other tumors. In this study, the contribution of advanced MRI to the diagnosis and differential diagnosis of SGTs will be reviewed.

Key Words: Salivary gland tumors; Magnetic resonance imaging; Diffusion-weighted imaging; Dynamic contrast-enhanced imaging; Perfusion-weighted magnetic resonance imaging

Core Tip: Conventional magnetic resonance imaging (MRI) provides more data than other radiological modalities in determining the extent of tumor extension and evaluating its relationship with vascular and neural structures in salivary gland tumors (SGTs). Advanced MRI techniques, which have been increasingly used in the radiological evaluation of SGTs in recent years, contribute to obtaining more information about the nature of the lesion compared to conventional sequences. Different features such as cellularity, microstructural features and vascularity of tumors can be evaluated by diffusion MRI or perfusion MRI techniques, and they can contribute to the differentiation of benign or malignant tumors.

Citation: Gökçe E, Beyhan M. Advanced magnetic resonance imaging findings in salivary gland tumors. *World J Radiol* 2022; 14(8): 256-271

URL: <https://www.wjgnet.com/1949-8470/full/v14/i8/256.htm>

DOI: <https://dx.doi.org/10.4329/wjr.v14.i8.256>

INTRODUCTION

Salivary gland tumors (SGTs) account for approximately 3%-5% of all head and neck tumors[1-3]. The majority of SGTs occur in the parotid glands, followed by those arising from the submandibular glands, minor salivary glands, and sublingual glands[3-6]. While the majority of those developing from the parotid glands are benign, the incidence of malignancy increases in tumors in other glands. In SGTs for which operation is planned, it is essential to determine the preoperative characterization of the tumor, its number, location (localization in the superficial or deep lobe for the parotid gland), extension to the surrounding tissues and lymphatic involvement[7]. The most effective radiological method in operative planning is magnetic resonance imaging (MRI). Conventional sequences may be insufficient to characterize SGTs. For this reason, in recent years, it has been tried to characterize tumors with advanced MRI applications [diffusion-weighted imaging (DWI) MRI, dynamic contrast-enhanced (semi-quantitative) MRI, perfusion (quantitative) MRI, diffusion tensor imaging (DTI), MR spectroscopy (MRS) *etc.*][1-5]. In this review, it is aimed to evaluate the imaging findings detected in advanced MRI applications of SGTs.

DWI

DWI is an imaging method that detects the motion of water molecules and allows calculation with the apparent diffusion coefficient (ADC). DWI, which can determine the cellularity and microstructural properties of tissues, can contribute to the differentiation of tumors[8-11]. When the studies on SGT were reviewed, some studies stated that the ADC values of malignant and benign tumors (BTs) were significantly different[12-16], while in some studies no significant difference was found[17,18], but in most of these studies, it was reported that ADC values were more effective in separating subgroups [pleomorphic adenomas (PMAs), Warthin's tumors (WTs) and lymphoma]. In the literature, mean ADC values of malignant SGTs are $(0.8-1.53) \times 10^{-3} \text{ mm}^2/\text{s}$ that of benign SGTs is $(1.04-1.72) \times 10^{-3} \text{ mm}^2/\text{s}$ reported in the range[16-21]. Although ADC values overlap in some SGTs due to the nature of the components they contain, we can generalize the mean ADC values of SGTs as malignant lymphomas < WTs < carcinomatous malignant tumors (MTs) < PMAs.

SEMI-QUANTITATIVE DYNAMIC CONTRAST-ENHANCED MRI

Dynamic contrast-enhanced (DCE) MRI in tumoral lesions is the acquisition of multiple T1-weighted images (T1WI) within a few minutes following contrast material administration to monitor contrast agent uptake and wash-out. On DCE MRI, the time intensity curve (TIC) is obtained in connection with the signal changes that occur with the passage of the contrast material through the tissues and the wash-out processes from the tissues. Slope, signal intensity (SI) peak, time to peak (Tpeak), enhancement ratio and wash-out ratio (WR) values can be obtained semi-quantitatively from the TIC curve. In the literature, different TIC patterns have been defined based on the Tpeak and wash-out values of SGTs[14, 22-27]. The most preferred TIC patterns were those described by Yabuuchi *et al*[24]. Tumor cellularity and vascularity are correlated with TIC patterns. Tpeak is related to the microvessel number and tends to be short when the microvessel count is high. Wash-out is dependent on the cellularity and stromal grade, with cellular tumors being wash-out more rapidly[3,24]. When we evaluate the TIC patterns of

SGTs, in general, PMAs tend to demonstrate progressive enhancement due to low microvessel content and cellularity-stromal grade. WTs and lymphomas show rapid enhancement and wash-out because of their high microvessel content and cellularity-stromal grade. MTs show rapid enhancement and wash-out due to high microvessel count and lower cellularity-stromal grade, but they tend to have a lower and slower wash-out compared to WTs[3]. TIC analysis can reveal physiological characterizations of different tissues using the blood flow properties of SGTs[26,28]. Despite overlapping TIC patterns in some SGTs, semi-quantitative DCE MRI is an imaging modality that can help differentiate subtypes of SGTs.

QUANTITATIVE DCE PERFUSION MRI

On DCE MRI, in addition to semi-quantitative examination with TIC parameters, quantitative perfusion MRI can be performed. In the literature, perfusion parameters such as K_{trans} [volume transfer constant between blood plasma and extracellular extravascular space (EES)], K_{ep} (flux rate constant between the EES and plasma), and V_e (EES fractional volume) have been studied in SGTs on quantitative DCE perfusion MRI[29]. In the literature, the K_{trans} values of PMAs were found to be lower than the K_{trans} values of other SGTs. However, while some studies stated that the K_{trans} values of PMAs differ significantly from those of other SGTs[29,30], some studies could not detect a significant difference[31]. In studies in the literature, K_{ep} values were found to be lowest in PMAs and highest in WTs. In some studies[29,31], the K_{ep} values of PMAs, WTs and MTs differed significantly, while in some studies only the K_{ep} values of WTs differed significantly from the other SGTs[30]. In the literature, it was found that mean V_e values of WTs were significantly lower than the V_e values of other SGTs[29-31].

DYNAMIC SUSCEPTIBILITY CONTRAST PERFUSION-WEIGHTED MRI

Dynamic susceptibility contrast (DSC) perfusion-weighted MRI measures signal loss during passage of a non-invasive contrast bolus through a tumor and can be performed using the bolus tracking technique that follows the first passage of contrast material through a capillary bed. DSC perfusion-weighted MRI is increasingly used as a diagnostic and research tool and to assess the extent of capillaries and microvasculature, mostly in central nervous system tumors. DSC perfusion-weighted MRI contributes to the assessment of tumor angiogenesis as the degree of signal loss depends on the volume of the intravascular space within a tumor and the concentration of injected contrast material in the blood[32]. There is a limited number of studies in the literature that have performed DSC perfusion-weighted MRI for SGTs and differing results have been obtained. In the study of Abdel Razek and Mukherji[33] on parotid tumors, it was reported that the mean DSC % values of both MTs and all BTs as well as PMAs, WTs and MTs were significantly different. Park *et al*[32] found that WTs tended to have higher DSC % values than malignant parotid tumors, although there was no significant difference. The parameters used in the evaluation of SGTs on some advanced MRI techniques are shown in Table 1.

PSEUDO/PULSED CONTINUOUS ARTERIAL SPIN LABELING PERFUSION MRI

Arterial spin labeling (ASL) provides measurement of tumor blood flow (TBF) using the magnetization of protons in arterial blood as an intrinsic tracer without the use of contrast material[34,35]. High vascularity, increased tumor blood volume, arterio-venous shunt formation, altered capillary transit time and increased the capillary permeability may lead to high TBF values in MTs. There is a limited number of studies in the literature that have performed ASL perfusion-weighted MRI for SGTs[35]. Razek[35] reported that TBF values of malignant SGTs were significantly higher than benign SGTs.

DTI

DTI provides the ability to distinguish between different tissue compartments at the cellular level, with different matrices that reflect the micromovement of water molecules. The most common DTI metrics used are fractional anisotropy (FA) and mean diffusivity (MD). MD is the average diffusivity along three orthogonal planes in the x, y, z directions of the tensor, equal to the mean of the three eigenvalues and equal to the ADC value. As the cellularity of the tumor increases, the MD value decreases. FA indicates the level of directionality of tissue microstructure in water diffusion and correlates with structural tissue orientations. FA correlates linearly with tumor cellularity and grade of malignancy. Abdel Razek *et al*[33] found a significant difference between the MD values of malignant and benign SGTs. At the same time, significant differences were found between the FA values of MTs and BTs in

Table 1 Evaluation on advance magnetic resonance imaging techniques of salivary gland tumors

	Advance magnetic resonance imaging techniques			
	Lymphoma	Warthin's tumor	Malign tumor	Pleomorphic adenoma
Diffusion weighted imaging (ADC values)	$< 0.8 \times 10^{-3} \text{ mm}^2/\text{s}$	$(0.8-1.0) \times 10^{-3} \text{ mm}^2/\text{s}$	$(1.0-1.2) \times 10^{-3} \text{ mm}^2/\text{s}$	$> 1.2 \times 10^{-3} \text{ mm}^2/\text{s}$
Dynamic contrast-enhanced MRI	50 s < Tpeak < 90 s, WR < 30%	Tpeak < 50 s, WR \geq 30%	Tpeak < 120 s, WR < 30%	Tpeak > 120 s, WR: Non-washout
Quantitative dynamic contrast-enhanced perfusion MRI		Ktrans < 0.8 min ⁻¹ , Kep > 1 min ⁻¹ , Ve < 0.2	Ktrans < 0.5 min ⁻¹ , Kep < 1 min ⁻¹ , Ve > 0.3	Ktrans < 0.3 min ⁻¹ , Kep < 0.6 min ⁻¹ , Ve < 0.9

ADC: Apparent diffusion coefficient; MRI: Magnetic resonance imaging; Tpeak: Time to peak; WR: Wash-out ratio; Ktrans: Volume transfer constant between blood plasma and extracellular extravascular space; Kep: Flux rate constant between the extracellular extravascular space and plasma; Ve: Extracellular extravascular space fractional volume.

DTI studies performed for SGTs[20]. WTs, which are rich in lymphoid content and have high anisotropy, have the highest FA levels among benign SGTs[20,33].

DIFFUSION KURTOSIS IMAGING

Diffusion kurtosis imaging (DKI) is a complex method that uses the non-Gaussian movement of water molecules in tissues. The MRIs are obtained based on the diffusion and microstructural features resulting from the organization of water molecules. A minimum of three *b* values are required on the DKI[36]. In the literature, some authors reported that DKI is useful in defining benign and malign SGTs, while some authors reported that no significant difference was found in distinguishing BTs and MTs. However, some of these authors reported that DKI parameters [ADC (D_{app}) and apparent kurtosis coefficient (K_{app})] differ significantly in PMAs compared to other SGTs[30,37].

INTRAVOXEL INCOHERENT MOTION MRI

Intravoxel incoherent motion (IVIM) provides both true molecular diffusion and motion of water molecules in the capillary network can be estimated with a single diffusion-weighted acquisition technique. Microvascular volume fraction (*f*), pure diffusion coefficient (*D*), and perfusion-related incoherent microcirculation (D^*) parameters are used on IVIM. Single-shot spin-echo echo-planar imaging with multiple *b* values usually ranging from 0-800 s/mm² is used to generate IVIM MRI. Sumi and Nakamura[26] reported that WTs had significantly higher *f* values than PMAs. In addition, Sumi and Nakamura[26] reported that *D* and D^* values contribute to the differentiation of WTs, PMAs, and MTs, and even the use of these parameters together provides 100% diagnostic accuracy.

PROTON MRS

Metabolite concentration in tissues and organs is measured in Proton MRS (1H-MRS) and used to characterize metabolic changes associated with tumors. Proton MRS in neoplasms uses a diagnostic algorithm based predominantly on the detection of high levels of choline compounds. Choline is an indicator of cellular proliferation and cell membrane transformation[38]. A limited number of studies have been conducted in the literature with MRS in SGTs[39]. King *et al*[39] reported that Cho/Cr ratios were significantly different between PMAs and WTs, and between BTs and MTs.

SGTS

According to the 4th edition of the World Health Organization (WHO)'s head and neck tumors classification published in 2017, SGTs are classified as MTs, BTs, non-neoplastic epithelial lesions, benign soft tissue lesions and haematolymphoid tumors[40]. WHO's head and neck tumors classification version 4 is given in Table 2. Despite efforts to simplify this classification, there are still more than 30 entities. MTs were divided into 20, BTs 11, non-neoplastic epithelial lesions 4, benign soft tissue lesions 3 subgroups. Two new entities have been added to this classification: Secretory carcinoma [known as mammary

Table 2 World Health Organization classification of salivary gland tumors 2017

Salivary gland tumors	
Malignant tumors	Benign tumors
Mucoepidermoid carcinoma	Pleomorphic adenoma
Adenoid cystic carcinoma	Myoepithelioma
Acinic cell carcinoma	Basal cell adenoma
Polymorphous adenocarcinoma	Warthin's tumor
Clear cell carcinoma	Oncocytoma
Basal cell adenocarcinoma	Lymphadenoma
Intraductal carcinoma	Cystadenoma
Adenocarcinoma, NOS	Sialadenoma papilliferum
Salivary duct carcinoma	Ductal papillomas
Myoepithelial carcinoma	Sebaceous adenoma
Epithelial-myoepithelial carcinoma	Canalicular adenoma and other ductal adenomas
Carcinoma ex pleomorphic adenoma	Non-neoplastic epithelial lesions
Secretory carcinoma	Sclerosing polycystic adenosis
Sebaceous adenocarcinoma	Nodular oncocytic hyperplasia
Carcinosarcoma	Lymphoepithelial sialadenitis
Poorly differentiated carcinoma	Haemangioma
Lymphoepithelial carcinoma	Lipoma/sialolipoma
Squamous cell carcinoma	Nodular fasciitis
Oncocytic carcinoma	Haematolymphoid tumors
Sialoblastoma	Extranodal marginal zone lymphoma of mucosa-associated lymphoid tissue

NOS: Not otherwise specified.

analogue secretory carcinoma (MASC)] and sclerosing polycystic adenosis to non-neoplastic epithelial lesions[41].

SALIVARY GLAND BTS

Pleomorphic adenoma (benign mixed tumor)

Pleomorphic adenoma is the most frequently observed SGT. Great majority of them are located in the parotid gland, and about 80%-90% is found on the surface of the gland[42-44]. PMAs are slowly growing, painless masses observed in 30-60 years of age and more frequently in women (ratio 2:1)[43, 44]. Multicentricity of PMAs is less than 1%[43]. At cellular level, morphological diversity characterized by a mixture of both epithelial and mesenchymal components is a characteristic feature of PMAs[44,45]. Ratio of these components varies greatly in PMAs, and MRI features vary based on the distribution of these components[44,46]. Stromal components in PMAs could be myxomatous, chondromatous, lipomatous, hyalinized, fibrous, calcified, or osseous, myxoid stroma being the most frequent (94.2%) [44,45]. Tsushima *et al*[47] mentioned that high intensity signals on T2WI represented myxoid histology. Classical appearance on T2WI of MRI is generally well bordered, microlobule contoured masses with prominently high signal confined by hypointense fibrous capsule[10,44,46-48]. Zaghi *et al*[49] evaluated the diagnostic efficiency of conventional MRI in differentiating PMAs using five different criteria. They found that masses with bright T2 signal, sharp borders, heterogeneous nodular enhancement, lobulated contours and a T2 dark rim were predictive of PMAs with a sensitivity of 43.9% and a specificity of 95%. Cellular variants of PMAs featured intermediate SI on T2WI due to their epithelial components, while the ones with fibrous stroma were hypointense. PMAs with hypointense signals on T2WI could represent malignancy, but the presence of complete capsule and lobulated contour are good indications of PMAs[44]. Cystic degeneration was observed in 29%-40% of parotid gland PMAs[50]. Due to their heterogeneous composition of epithelial, myoepithelial and stromal cells with fluid areas within

epithelial glandular regions, PMAs have unrestricted diffusion and high ADC values. ADC values of PMAs were reported to vary between $(0.66-2.86) \times 10^{-3} \text{ mm}^2/\text{s}$ [19-21,51], while ADC_{mean} values varied from $(1.35-2.15) \times 10^{-3} \text{ mm}^2/\text{s}$ [19,20,51-53]. Cellular variants of PMAs could have lower ADC values in the range of $(1.0-1.3) \times 10^{-3} \text{ mm}^2/\text{s}$ [44,54]. Average Dapp value of $(1.525 \pm 0.396) \times 10^{-3} \text{ mm}^2/\text{s}$ and average Kapp value of 0.394 ± 0.172 were reported for PMAs on DKI[37]. Huang *et al*[30] reported the mean *D* value as $1.81 \times 10^{-3} \text{ mm}^2/\text{s}$ and the *K* value as 0.51 on DKI. Zheng *et al*[52] reported that a great majority of PMAs featured type A TIC pattern (persistent and $T_{\text{peak}} > 120 \text{ s}$) because of unbroken capillary endothelial cells and more complex nature of stroma in tumor (Figure 1). They also mentioned slow flow of contrast medium into extracellular space. However, cellular variants of PMAs showed atypical gradual wash-out pattern on DCE MR due to their high epithelium content and low myxoid stroma[52]. Frequency of this atypical pattern in all PMA TIC patterns was reported to be about 17%-18%[24,44,55].

Regarding T_{peak} values of PMAs on DCE MRI, Tsushima *et al*[23] observed T_{peak} was equal to or greater than 260 s while Sumi and Nakamura[26] found T_{peak} values of 120 s or longer in 92.9% of the cases and less than 120 s in 7.1% of them. Similarly, Zheng *et al*[52] measured 120 s or over in 88.9% of the cases and less than 120 s in 11.1%. Tao *et al*[14], on the other hand, found 58 s or longer T_{peak} values in 82.0% of the cases whereas in 18% it was less than 58 s. For WR values of PMAs, Tsushima *et al*[23] reported no wash-out while Zheng *et al*[52] reported no wash-out in 88.9% of the patients and less than 30% WR in 11.1% of the cases. The literature contains a few studies on quantitative DCE perfusion MRI parameters (*K*_{trans}, *K*_{ep} and *V*_e) in SGTs. In these studies, mean *K*_{trans} value of PMAs was 0.101 ± 0.069 to 0.217 ± 0.036 ; mean *K*_{ep} values 0.245 ± 0.160 to 0.567 ± 0.048 ; mean and values were determined as 0.380 ± 0.192 to 0.590 ± 0.478 [3,7,30].

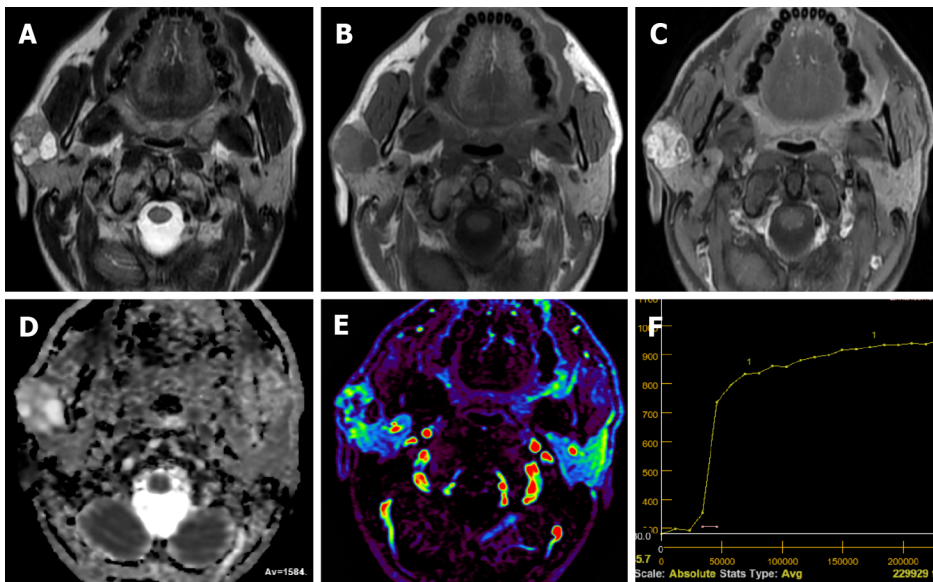
WT

WT is the second most commonly observed benign SGT[43,48]. It is mostly observed in middle-age or older men in the parotid gland or periparotid region and more commonly in the inferior pole of the parotid gland[56,57]. Smoking, autoimmune disease and radiation exposure were reported to increase WT risk[43,48,56]. About 20% of WTs tend to be bilateral and multicentric[43,56]. They generally have a spherical to ovoid shape of 2-4 cm diameter, and their surface is smooth. WT is basically an adenoma with mucoid or brown fluid filled cysts of variable number. The cysts are made of two layered papillary proliferations of oncocytic epithelium and supporting stroma made of an abundant follicle carrying lymphoid tissue. They may have focal hemorrhage and necrosis[57]. Transformation of WTs to malignancy is extremely rare (0.3%)[43,56]. Intermediate or hypointense areas on short tau inversion recovery and T2WI, and hyperintense area on T1WI on MRI suggest WTs[48,57,58]. Solid WT components result in iso-intensity or hypo-intensity on T2WI because histopathologically WT is made of epithelial cells and lymphoid stroma with fibrovascular tissue[56]. About 30%-60% of WTs are partly or predominantly cystic[50,56,58]. WTs may resemble other less frequently observed benign lesions such as myoepitheliomas and basal cell adenomas (BCAs) which may also carry cystic components and tend to involve superficial lobe of parotid gland[48,59,60]. WTs were reported to have low ADC values (Figure 2) due to their epithelial and lymphoid stroma contents which have microscopic slit-like cysts containing proteinous fluid[56,57]. In different studies, ADC values of WTs ranged from $(0.69-1.36) \times 10^{-3} \text{ mm}^2/\text{s}$ and ADC_{mean} was about $(0.74-1.02) \times 10^{-3} \text{ mm}^2/\text{s}$ [19,52,53,56,57]. Only two studies in the literature reported ADC_{mean} values higher than $1.0 \times 10^{-3} \text{ mm}^2/\text{s}$, while others had lower values. A study reported that mean *D*_{app} and mean *K*_{app} values of WTs on DKI were $(0.808 \pm 0.227) \times 10^{-3} \text{ mm}^2/\text{s}$ and 0.999 ± 0.228 , respectively[37]. Huang *et al*[30] reported the mean *D* value of WTs as $0.97 \times 10^{-3} \text{ mm}^2/\text{s}$ and the mean *K* value as 0.99 on DKI.

In terms of T_{peak} values of WT in studies on the literature dealing with DCE MRI, Tsushima *et al*[23] reported $< 20 \text{ s}$, Hisatomi *et al*[61] in the range of 30-45 s, Sumi and Nakamura[26] $< 120 \text{ s}$, while Tao *et al*[14] found that in 97.6% of the cases T_{peak} was less than 58 s and in 2.4% of the cases T_{peak} was equal to or greater than 58 s. For WR values of WTs, Hisatomi *et al*[61] mentioned that WR was prominent in the first 30 s after *T*_{max}. On the other hand, Sumi and Nakamura[26] found that WR ranged from 30%-70%, while Zheng *et al*[52] found WR values equal to or larger than 30%. Tao *et al*[14] found that WR values were 22.6% or over in 85.4% of the cases, less than 22.6% in 12.2% and no wash-out was observed in 2.4% of the cases. In the literature, quantitative DCE perfusion MRI values in WTs mean *K*_{trans} values 0.105 ± 0.064 to 0.464 ± 0.036 ; mean *K*_{ep} values 0.729 ± 0.112 to 2.299 ± 1.312 ; mean *V*_e values are reported in the range of 0.1439 ± 0.093 to 0.272 ± 0.013 [29-31].

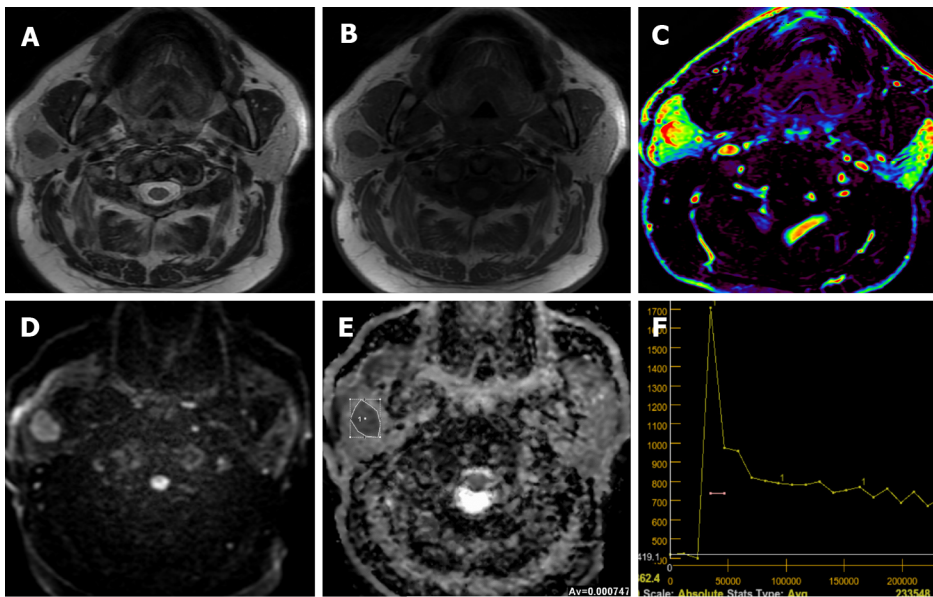
Oncocytoma

Oncocytomas are well bordered, benign epithelial neoplasms of homogeneous solid structure consisting of mitochondria-rich oncocytes[48,60]. They constitute about 1% of parotid tumors, but about 80% of them are observed in the parotid gland[48,56,60]. They are commonly observed in people in their 60 s and 80 s, and are slightly more common in women. Because they have high cellularity and low free water content, conventional MRI findings of oncocytomas resemble those of WTs[62]. In addition, with their lower ADC content, fast enhancement and wash-out on dynamic MRI, findings of DWI and DCE MRI could overlap. However, oncocytomas usually have higher ADC values than WTs[56]. Oncocytomas were reported to have ADC values ranging from $(0.8-1.16) \times 10^{-3} \text{ mm}^2/\text{s}$ [56,63]. Hisatomi *et*



DOI: 10.4329/wjr.v14.i8.256 Copyright ©The Author(s) 2022.

Figure 1 Twenty-nine years old male patient with smooth lobule contoured pleomorphic adenoma located on the superficial lobe of right parotid gland. A: The lesion contains prominent hyperintense components and mixed signals on T2-weighted image; B: The lesion contains heterogeneous hypointense signal on T1-weighted image; C: The lesion appears to have marked heterogeneous enhancement on the contrast-enhanced image; D: The apparent diffusion coefficient (ADC) value of mass was $1.58 \times 10^{-3} \text{ mm}^2/\text{s}$ on ADC map; E: Hypo-hyper perfused areas on perfusion magnetic resonance imaging color map; F: The time intensity curve of mass is seen increasing contrast-enhancement towards late phases.



DOI: 10.4329/wjr.v14.i8.256 Copyright ©The Author(s) 2022.

Figure 2 Sixty-five years old male patient with smooth lobule contoured Warthin's tumor located on the superficial lobe of right parotid gland. A and B: Hypointense signal of the lesion compared to the gland on T2-weighted image and T1-weighted image; C: The mass is hyperperfused on the color-coded perfusion image; D: The mass appears to be slightly heterogenous hyperintense on the diffusion-weighted image, E: The apparent diffusion coefficient (ADC) value of mass was $0.74 \times 10^{-3} \text{ mm}^2/\text{s}$ on the ADC map; F: The time intensity curve of mass has a wash-out ratio of 50%.

al[61] found that oncocytomas have similar contrasting dynamics to WT, and consequently, they cannot be differentiated from WTs using DCE MRI alone.

BCA

BCAs are made of basaloid cells carrying eosinophilic cytoplasm, and they have no clear cell borders. Their nuclei are round-to-oval. They have solid, trabecular, tubular and membranous distribution patterns. Although most tumors carry one of these patterns predominantly, some of them may have more than one pattern. Membranous BCAs have different biological characteristics from other BCA

variants because they carry microfocal adenomas, incomplete capsules or no capsule. Besides, they may recur after operation and they have malignant transformation characteristics. Their frequency is higher after 50 years of age, and women have a slightly higher prevalence[51]. BCAs most frequently arise from the parotid gland and are more frequently located in the superficial lobe[31,51]. They tend to have clearly defined borders[3,31,51]. BCAs may have cystic or hemorrhagic components[51]. In MRI of BCAs, signal intensities on T1WIs are relatively low while on T2WIs intensity varies between hypointense to slightly intense. In studies in the literature, mean ADC values of BCAs were found to be $[(1.21 \pm 0.20)-(1.24 \pm 0.18)] \times 10^{-3} \text{ mm}^2/\text{s}$ [31,51]. On dynamic MRI, on the other hand, they feature rapid and prolonged enhancement[51]. Mukai *et al*[51] found that on DCE MRI, 12 of 14 BCAs (85.7%) had TIC patterns of either $T_{\text{peak}} > 120 \text{ s}$ or $T_{\text{peak}} < 120 \text{ s}$ and wash-out $< 30\%$. Yabuuchi *et al*[31] reported $T_{\text{peak}} < 120 \text{ s}$ and wash-out $< 30\%$ in 61.5% of BCAs in DCE MRI, and $T_{\text{peak}} > 120 \text{ s}$ and no wash-out in 15.3% of them.

Myoepithelioma

Myoepitheliomas are responsible only for about 1%-1.5% of all salivary neoplasms. Their primary location is parotid gland (about 40%) but they may also appear on other salivary gland parts (about 21%)[59,64]. Differentiated myoepithelial cells in the form of spindle, plasmacytoid, epithelioid, or clear cells constitute most of myoepithelioma[59]. Myoepithelial cells were proposed to have contractile units helping to excrete glandular secretions. Myoepitheliomas need to be differentiated from parotid cyst, abscess, mucocele, schwannoma, leiomyoma, neurofibroma, rhabdomyosarcoma, smooth muscle neoplasms, extramedullary plasmacytoma, benign fibrous histiocytoma, PMA, mucoepidermoid carcinoma (MEC) and myoepithelial carcinoma[64]. They feature homogeneous isointense signal based on muscle tissue on T1WI and homogeneous iso-hyperintense signals on T2WI. In the majority of them (about 80%), hypointense capsule formation and homogeneous contrasting could be observed on T2WI and contrast-enhanced series[59]. ADC_{mean} values of myoepithelioma in different studies varied from 1.31 ± 0.9 to 1.86 ± 0.18 (range 1.18-1.91) $\times 10^{-3} \text{ mm}^2/\text{s}$ [19].

Schwannoma and neurofibroma

Intraparotid neurofibromas or schwannomas could be associated with neurofibromatosis, but they may also arise sporadically[48]. Frequency of parotid tumors which originate in the facial nerve was estimated to be between 0.2%-1.55%[65]. A fusiform tumor appearance extending into intratemporal facial nerve canal could be a distinguishing feature in diagnosis. However, this appearance also resembles perineural extension of malignant neoplasms. Peripheral nerve sheath tumors could easily be distinguished by their target and fascicular signs on MRI[48]. The target sign refers to the appearance of central T2 hypointensity and enhancement and peripheral T2 hyperintensity and non-enhancement[48, 65]. The fascicular sign corresponds to multiple ring-like T2 hypointense foci within a relatively T2 hyperintense and enhancing background[48]. On DWI, neurofibromas were reported to have ADC_{mean} values in the range of (1.41-1.91) $\times 10^{-3} \text{ mm}^2/\text{s}$ [13,17].

Lipoma or sialolipoma

Lipomas are neoplasms consisting of mature adipose tissue. For salivary gland involvement, they may be intraglandular or extraglandular[48]. Lipomas have similar signal intensities to subcutaneous adipose tissue on T1WI and T2WI[66]. Fat-suppression is useful on MRI of salivary gland lipomas. These tumors may have septations when they surround vessels[48]. Some rare variants of lipomas with a biphasic pattern where serous tissue is diffusely scattered among fat is termed sialolipoma and their appearance closely resemble normal parotid tissue[48,67]. They are encapsulated but tend to be heterogeneous in appearance due to their soft salivary gland tissue and fat tissue[48]. DWI studies showed that lipomas had ADC_{mean} values of $(0.09-0.62) \pm 0.21$ [range $(0.08-0.76) \times 10^{-3} \text{ mm}^2/\text{s}$] [19].

Hemangioma

Hemangiomas refer to vascular abnormalities involving increased proliferation and endothelial cell renewal. They are more common in childhood. About 60%-65% of hemangiomas are observed in the head and neck area, and 81%-85% of them are found in the parotid gland. Hemangiomas constitute 0.4%-0.6% of all tumors in the parotid gland and the ADC value of the hemangioma was found to be $0.8 \times 10^{-3} \text{ mm}^2/\text{s}$ [68]. On MRI, they have homogeneously hyperintense appearance on T2WI and strong enhancement, but they are devoid of prominent flow. These tumors often affect the whole gland and could have additional lesions elsewhere in the head and neck or in other regions[48,68].

SALIVARY GLAND MTS

MEC

MEC refers to the most common salivary gland malignancy and 60% of these lesions involve the parotid gland. MEC develops in epithelium tissue of salivary gland ducts. It is made of mucus secreting cells,

epidermoid cells and intermediate cells[46]. They may have low, intermediate or high-grade subtypes with different radiological appearances. Low grade tumors have smooth borders and cystic components containing mucin, and have hyperintense signals on T1WI and T2WI. High-grade tumors, on the other hand, are quite solid with undefined borders due to extension into neighboring structures. They often appear on T2WI as hypointense or isointense lesions due to their high cellularity[33]. ADC values of MECs on DWI is low in poorly differentiated lesions. ADC_{mean} values of MECs on DWI studies were reported to vary from $[(0.81 \pm 0.06)-(1.05 \pm 0.03)] \times 10^{-3} \text{ mm}^2/\text{s}$ [range $(0.65-1.14) \times 10^{-3} \text{ mm}^2/\text{s}$][13,19,20, 69]. Zheng *et al*[52] reported T_{peak} value of 120 s or lower for MECs on DCE MRI. WR of a case was reported to be less than 30% while that of another was 30% or over.

Adenoid cystic carcinoma

Adenoid cystic carcinoma (ACCa) is made of ductal epithelial and myoepithelial cells. It may be in solid, cribriform or tubular forms, cribriform being most common. It is more frequent in middle-aged or elderly patients. Perineural spreading and invasion capacity of ACCa is very high[46]. They can result in distant metastases and local invasions. ACCa is frequently observed as ill-defined masses with perineural spreading in imaging. ACCa has intermediate to low signal on T1WI and T2WI MRI. The parotid gland is the most common location for ACCa (about 25%), which often involves perineurium of cranial nerve VII during the diagnosis[46]. On DWI studies, ACCas were found to have ADC_{mean} values varying from $[(0.84 \pm 0.07)-(1.46 \pm 0.03)] \times 10^{-3} \text{ mm}^2/\text{s}$ [9,13,17,19,69]. Tsushima *et al*[23] detected PMA-like TIC pattern (Figure 3) in two ACCa cases using DCE MR (T_{peak} > 260 s and no wash-out). It was suggested that this pattern could be due to increased interstitial space of ACCa which contains extracellular mucin and low microvessel count[3,23]. Zheng *et al*[52] reported that one ACCa they studied had the TIC pattern most commonly observed in MTs (type C, T_{peak} ≤ 120 s and WR < 30%).

Acinic cell carcinoma

Acinic cell carcinoma is a low-grade malignant lesion, and about 90% of these lesions are located in the parotid gland[46]. Its characteristic feature is serous acinar differentiation and basophilic granules in cytoplasm[8]. No specific finding is observed in imaging, but most acinic cell carcinomas are homogeneously enhanced, well-bordered, slowly growing masses like other benign or low grade malignant lesions[33,46]. Most of the malignancies which were previously considered acinic cell carcinomas are now identified as MASCs[46]. Kashiwagi *et al*[70] revealed that acinic cell carcinomas tended to be solid while MASCs were predominantly cystic masses with solid papillary extensions. The authors mentioned that intermediate-high SI of acinic cell carcinomas on T1WI could help in differential diagnosis. DWI studies in the literature showed ADC_{mean} values from $[(0.79 \pm 0.33)-(1.76 \pm 0.11)] \times 10^{-3} \text{ mm}^2/\text{s}$ for acinic cell carcinomas[69,70]. Zheng *et al*[52] studied three acinic cell carcinoma cases on DCE MRI and observed a T_{peak} value of 120 s or less. WR was over 30% in two cases and equal to or larger than 30% in the other.

MASC

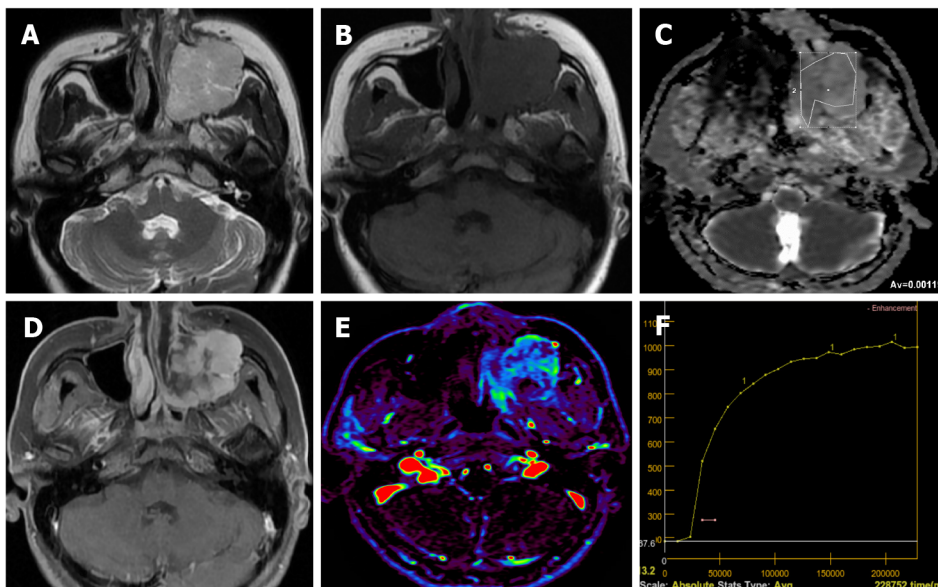
MASC was first described in 2010 as a rare salivary carcinoma mimicking acinar cell carcinoma and was released to the World Health Organization classification of head and neck tumors in 2017[71,72]. MASC has morphological and genetic similarities with secretory carcinoma of the breast. The majority of MASCs (approximately 70%-80%) are located in the parotid gland, while a smaller number are located in other minor salivary gland areas or major salivary gland glands[72,73]. MASCs are often tumors of “papillary and cystic” or “non-papillary and cystic” morphology. The cystic and solid components of these tumors have high signal on T1WIs on MRI, more often in the cystic component. On contrast-enhanced MRI series, solid components may show different forms of enhancement (homogeneous, heterogeneous, or scarce)[72]. DWI has been applied in a limited number of cases in MASCs, and ADC values in the solid components of the tumor vary between $(0.5-1.7) \times 10^{-3} \text{ mm}^2/\text{s}$ [70,72].

Carcinoma ex pleomorphic adenoma

Carcinoma ex pleomorphic adenoma arises in connection with a primary or repeating benign PMA. About 1.5% of pleomorphic adenoma cases develop carcinoma ex pleomorphic adenoma in five years, and 10% of them in 15 years. In this condition, a painless mass still for many years starts growing. They appear in MRI as masses with ill-defined borders extending into surrounding tissues, discontinuous hypointense rim and mediate to low heterogeneous SI on T2WI[74]. On DWI studies, carcinoma ex PMAs were reported to have ADC_{mean} values in the range of $[(0.82 \pm 0.01)-(1.32 \pm 0.035)] \times 10^{-3} \text{ mm}^2/\text{s}$ [9, 13,17]. Zheng *et al*[52] found that T_{peak} of carcinoma ex PMA was 120 s or less while their WR was less than 30% on DCE MRI.

Lymphoma

Primary lymphoma of salivary glands is rare and in 75%-80% of the cases parotid gland is involved. Most commonly encountered Non-Hodgkin lymphoma types of salivary glands are extranodal marginal zone B-cell lymphoma in mucosa-associated lymphoid tissue (MALT), follicular B-cell lymphoma and diffuse large B-cell lymphoma. Follicular type and MALT lymphomas are low-grade



DOI: 10.4329/wjr.v14.i8.256 Copyright ©The Author(s) 2022.

Figure 3 Forty-four years old female patient with adenoid cystic carcinoma infiltrating into the left maxillary sinus. A: T2-weighted image shows a hyperintense mass in the left maxillary sinus; B: T1-weighted image shows a hypointense mass in the left maxillary sinus; C: The apparent diffusion coefficient (ADC) value of mass was $1.19 \times 10^{-3} \text{ mm}^2/\text{s}$ on the ADC map; D: There was intense contrast enhancement on the contrast-enhanced image of the mass; E: On the color-coded perfusion magnetic resonance imaging, hyper and hypoperfused areas are seen in the mass; F: On the time intensity curve of mass, progressive enhancement is seen towards the late phases.

lesions characterized by slow growth, which sometimes regress spontaneously. In cases with autoimmune conditions such as Sjogren's syndrome MALT lymphoma risk is 44 times higher. Parotid MALT lymphomas are mostly solid-cystic lesions which may have a solitary or diffused pattern. In non-MALT lymphomas, on the other hand, multiple or solitary homogeneous internal structure is more common. A diffuse large B-cell lymphoma is the most common high-grade lymphoma involving the parotid gland. Some of them arise from an underlying low-grade lesion. They manifest themselves with an asymptomatic mass in the parotid gland which grows in a period of four to six months[75]. The ADC values of lymphomas on DWI were generally lower than other solitary tumors (Figure 4), which helps in their differential diagnosis. DWI studies found ADC_{mean} values from 0.55 to 0.98 [range $(0.4-1.21) \times 10^{-3} \text{ mm}^2/\text{s}$] for parotid gland lymphomas[15,20,21,58,76].

It has been known that malignant lymphomas have higher cellularity and less extracellular space than head and neck carcinomas[27,76]. Therefore, malignant lymphomas show rapid enhancing and wash-out TIC patterns[19,26,28]. Since TIC patterns of malignant lymphomas and WTs are similar, differentiation of WTs and malignant lymphomas cannot be done using DCE MRI alone[27]. However, T_{peak} of lymphomas are somewhat longer and their WR is lower compared to WTs. In their study dealing with head and neck lymphomas, Asaumi *et al*[77] measured average maximum duration for lymphomas to reach contrast index as $78.5 \pm 29.1 \text{ s}$. Tao *et al*[14], on the other hand, found that in all of seven lymphomas they studied T_{peak} was less than 58 s while WR was less than 22.6% in six of them (85.7%) but equal to or greater than 22.6% in one (14.3%). Wang *et al*[76] evaluated 20 MALToma cases and reported that parotid MALTomas were usually (94.1% of the patients) in early ascending type (*i.e.*, type I, with a T_{peak} of less than 79.65 s and an initial slope of increase less than 0.807). They mentioned that T_{peak} values could be used to distinguish between parotid tumor-like benign lymphoepithelial lesion (BLEL) and MALToma because T_{peak} value was at least twice higher in tumor-like BLEL cases compared to MALToma cases[76].

Salivary duct carcinoma

Salivary duct carcinoma (SDC) refers to tumors of different sizes characterized by duct structures which contain eosinophilic tumor cells. They often have a cribriform structure. SDC constitutes the most commonly encountered malignant component of carcinoma ex pleomorphic adenoma. Majority of SDCs originate from PMAs[78]. On DWI studies, ADC_{mean} values of SDCs were reported to vary from $(0.88-1.28) \pm 0.16$ [range $(0.87-1.47) \times 10^{-3} \text{ mm}^2/\text{s}$][26,27,30,31,79]. Motoori *et al*[79] reported that on DCE MRI 78% of SDCs appeared as type B ($T_{\text{peak}} < 120 \text{ s}$ and $\text{WR} < 30\%$), and 67% of had areas of type C TIC pattern ($T_{\text{peak}} > 120 \text{ s}$) due to their abundant fibrotic tissue.

Epithelial-myoepithelial carcinoma

Epithelial-myoepithelial carcinoma (EMC) is a rare subtype of malignant salivary gland tumor.

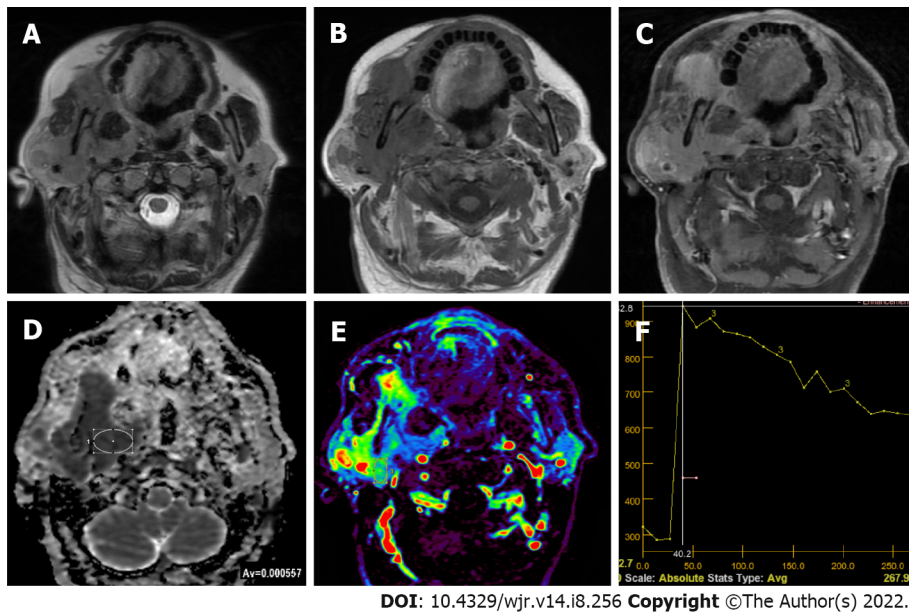


Figure 4 Sixty-one years old male patient with non-Hodgkin lymphoma infiltrating into the right parotid gland. A and B: Hypointense signal of the lesion compared to the gland on T2-weighted image and T1-weighted image; C: Contrast enhancement components of different intensities are seen on contrast-enhanced image in the lesion; D: The apparent diffusion coefficient (ADC) value of mass was $0.55 \times 10^{-3} \text{ mm}^2/\text{s}$ on the ADC map; E: The mass is hyperperfused on the color-coded perfusion image; F: The time intensity curve of mass has a wash-out ratio of 43%.

Histopathologically, it consists of a biphasic array of inner lumen ductal cells and outer myoepithelial cells. On conventional MRI, EMCs are well-contoured, may contain mostly solid or cystic components, septa or multi-nodularity can be detected, solid components are isointense or hypointense on T1WIs, hyperintense or isointense on T2WIs, contrast-enhancement with different forms (homogeneous or heterogeneous; moderate, mild or none) can be seen as masses. On DWI studies, ADCmean values of EMCs were reported to vary from $(0.96\text{-}1.05) \pm 0.03$ [range $(0.789\text{-}1.14) \times 10^{-3} \text{ mm}^2/\text{s}$][80].

Secondary malignancies of the salivary glands (metastases)

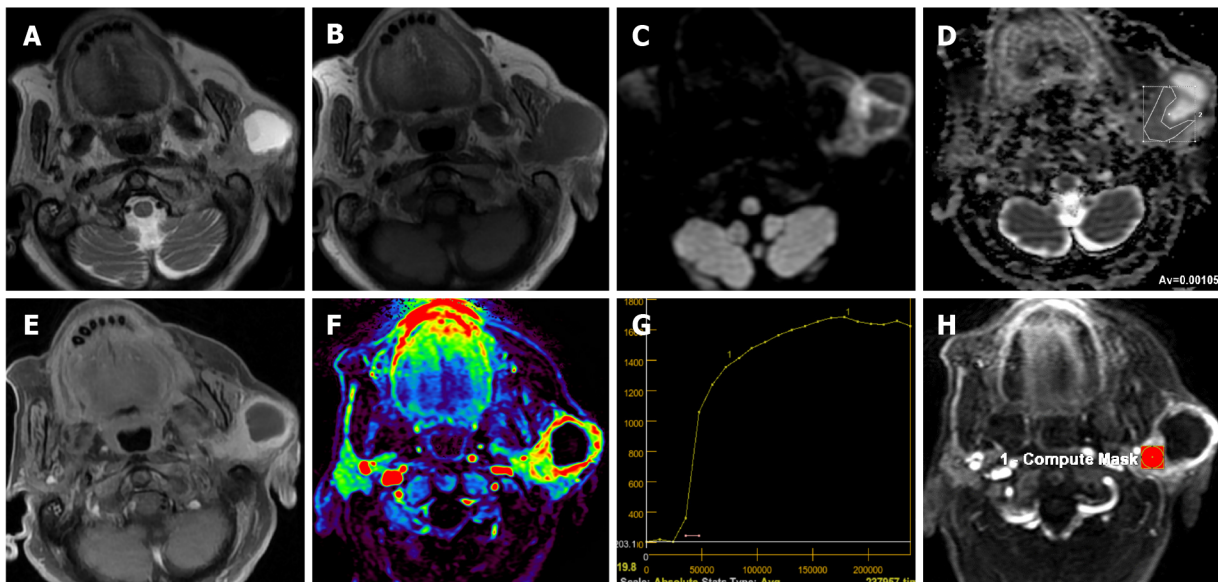
Secondary malignancies of the salivary glands may develop either by distant metastasis or by direct infiltration of tumors from adjacent tissues. Secondary malignancies of the salivary glands may involve the parenchyma of the salivary glands or the intraglandular and/or periglandular lymph nodes. Secondary malignancies most commonly involve the parotid gland, followed by the submandibular gland. Metastases in other salivary glands are less common. Metastases to the salivary glands most commonly arise from squamous cell carcinomas of the head and neck region and the upper aerodigestive tract[81,82] (Figure 5). Various hematopoietic and lymphoid malignancies, including lymphomas, but not as much as squamous cell carcinomas, constitute a significant portion of secondary malignancies of the salivary glands[81]. Metastases may originate less frequently from distant organs such as malignant melanoma, breast, lung, kidney, thyroid, pancreatobiliary, prostate, and bladder[81, 82].

Cystic lesions of parotid gland and its tumors which may have cystic component

Parotid gland could have pure cystic benign lesions such as lymphoepithelial cysts, lymphangiomas, dermoid cysts, first branchial cleft cysts and mucocele, but they could be BTs and MTs which contain cystic components of different size[50]. Kato *et al*[50] found cystic components of different size scattered over different areas which might have different T1 and T2 signal characteristics in 40% of PMAs, 60% of WTs, 67% of BCAs, 86% of SDCs, 80% of MECs, 75% of epithelial myoepithelial cell carcinomas, 50% of acinic cell carcinomas, 100% of carcinoma ex PMA, 100% of adenocarcinomas and 100% of ACCs. In order to avoid erroneous ADC measurements in tumors with cystic or necrotic components using DWI and in measurements to determine TIC pattern in DCI, region of interest should be placed in solid sections of the lesions[24,62,83].

CONCLUSION

In addition to the morphological data of conventional MRI, advanced MRI techniques allow us to obtain information about the cellularity, microstructural features or vascularity of tumors and thus to interpret the nature and subtypes of tumors. For example, while high cellular tumors such as WTs or lymphomas



DOI: 10.4329/wjr.v14.i8.256 Copyright ©The Author(s) 2022.

Figure 5 Eighty-seven years old female patient with squamous cell carcinoma infiltrating into the left parotid gland. A: T2-weighted image shows a mass with a large cystic component; B: The lesion is hypointense on T1-weighted image; C: Solid component of the mass appears to be slightly hyperintense on the diffusion-weighted image; D: The apparent diffusion coefficient (ADC) value of the solid component of mass was $1.05 \times 10^{-3} \text{ mm}^2/\text{sec}$ on the ADC; E: There was intense contrast enhancement of the solid component of mass on the contrast-enhanced image; F: On the color-coded perfusion magnetic resonance imaging, hyperperfused areas are seen in the solid component of the mass; G: On the time intensity curve of mass, progressive enhancement is seen towards the late phases. H: Ktrans was measured on quantitative dynamic contrast-enhanced magnetic resonance imaging.

show low ADC values on diffusion MRI, they cause rapid contrast enhancement and significant wash-out on dynamic contrast MRI series. Except for their cellular variants, PMAs show high ADC values and an increasing TIC pattern on dynamic MR series. High cellular MTs show diffusion restrictions and WRs not as much as WTs or lymphomas. Quantitative perfusion MRI values (such as Ktrans, Kep, Ve) can be measured in accordance with the structural features of the tumors. With the increase in data and studies on the nature and subtypes of SGTs in the literature, threshold values or acceptance intervals for quantitative measurements have begun to emerge, although there are overlaps.

FOOTNOTES

Author contributions: Gökçe E designed the study; Beyhan M supervised the study. Gökçe E and Beyhan M participated in literature research and manuscript preparation, and read and approved the final version.

Conflict-of-interest statement: All the authors report no relevant conflicts of interest for this article.

Open-Access: This article is an open-access article that was selected by an in-house editor and fully peer-reviewed by external reviewers. It is distributed in accordance with the Creative Commons Attribution NonCommercial (CC BY-NC 4.0) license, which permits others to distribute, remix, adapt, build upon this work non-commercially, and license their derivative works on different terms, provided the original work is properly cited and the use is non-commercial. See: <https://creativecommons.org/licenses/by-nc/4.0/>

Country/Territory of origin: Turkey

ORCID number: Erkan Gökçe 0000-0003-3947-2972; Murat Beyhan 0000-0002-8630-4632.

S-Editor: Wang JJ

L-Editor: A

P-Editor: Wang JJ

REFERENCES

- 1 Gao M, Hao Y, Huang MX, Ma DQ, Chen Y, Luo HY, Gao Y, Cao ZQ, Peng X, Yu GY. Salivary gland tumours in a northern Chinese population: a 50-year retrospective study of 7190 cases. *Int J Oral Maxillofac Surg* 2017; **46**: 343-349

- [PMID: 27769738 DOI: 10.1016/j.ijom.2016.09.021]
- 2 **Del Signore AG**, Megwalu UC. The rising incidence of major salivary gland cancer in the United States. *Ear Nose Throat J* 2017; **96**: E13-E16 [PMID: 28346649 DOI: 10.1177/014556131709600319]
 - 3 **Abdel Razek AAK**, Mukherji SK. State-of-the-Art Imaging of Salivary Gland Tumors. *Neuroimaging Clin N Am* 2018; **28**: 303-317 [PMID: 29622121 DOI: 10.1016/j.nic.2018.01.009]
 - 4 **Carlson ER**. Management of Parotid Tumors. *J Oral Maxillofac Surg* 2017; **75**: 247-248 [PMID: 28328430 DOI: 10.1016/j.joms.2016.12.001]
 - 5 **Kuan EC**, Mallen-St Clair J, St John MA. Evaluation of Parotid Lesions. *Otolaryngol Clin North Am* 2016; **49**: 313-325 [PMID: 26902978 DOI: 10.1016/j.otc.2015.10.004]
 - 6 **Eveson JW**, Cawson RA. Salivary gland tumours. A review of 2410 cases with particular reference to histological types, site, age and sex distribution. *J Pathol* 1985; **146**: 51-58 [PMID: 4009321 DOI: 10.1002/path.1711460106]
 - 7 **Mansour N**, Hofauer B, Knopf A. Ultrasound Elastography in Diffuse and Focal Parotid Gland Lesions. *ORL J Otorhinolaryngol Relat Spec* 2017; **79**: 54-64 [PMID: 28231589 DOI: 10.1159/000455727]
 - 8 **Munhoz L**, Abdala Júnior R, Abdala R, Arita ES. Diffusion-weighted magnetic resonance imaging of the paranasal sinuses: A systematic review. *Oral Surg Oral Med Oral Pathol Oral Radiol* 2018; **126**: 521-536 [PMID: 30143461 DOI: 10.1016/j.oooo.2018.07.004]
 - 9 **Inci E**, Hocaoglu E, Kilickesmez O, Aydin S, Cimilli T. Quantitative Diffusion-Weighted MR Imaging in the Differential Diagnosis of Parotid Gland Tumors: Is it a Useful Technique? *Turkiye Klinikleri J Med Sci* 2010; **30**: 1339-1345 [DOI: 10.5336/medsci.2009-14994]
 - 10 **Lechner Goyault J**, Riehm S, Neuville A, Gentine A, Veillon F. Interest of diffusion-weighted and gadolinium-enhanced dynamic MR sequences for the diagnosis of parotid gland tumors. *J Neuroradiol* 2011; **38**: 77-89 [PMID: 20542568 DOI: 10.1016/j.neurad.2009.10.005]
 - 11 **Celebi I**, Mahmutoglu AS, Ucgul A, Ulusay SM, Basak T, Basak M. Quantitative diffusion-weighted magnetic resonance imaging in the evaluation of parotid gland masses: a study with histopathological correlation. *Clin Imaging* 2013; **37**: 232-238 [PMID: 23465973 DOI: 10.1016/j.clinimag.2012.04.025]
 - 12 **Milad P**, Elbegiermy M, Shokry T, Mahmoud H, Kamal I, Taha MS, Keriakos N. The added value of pretreatment DW MRI in characterization of salivary glands pathologies. *Am J Otolaryngol* 2017; **38**: 13-20 [PMID: 27806890 DOI: 10.1016/j.amjoto.2016.09.002]
 - 13 **Abdel Razek AA**, Samir S, Ashmalla GA. Characterization of Parotid Tumors With Dynamic Susceptibility Contrast Perfusion-Weighted Magnetic Resonance Imaging and Diffusion-Weighted MR Imaging. *J Comput Assist Tomogr* 2017; **41**: 131-136 [PMID: 27636248 DOI: 10.1097/RCT.0000000000000486]
 - 14 **Tao X**, Yang G, Wang P, Wu Y, Zhu W, Shi H, Gong X, Gao W, Yu Q. The value of combining conventional, diffusion-weighted and dynamic contrast-enhanced MR imaging for the diagnosis of parotid gland tumours. *Dentomaxillofac Radiol* 2017; **46**: 20160434 [PMID: 28299943 DOI: 10.1259/dmfr.20160434]
 - 15 **Elmokadem AH**, Abdel Khalek AM, Abdel Wahab RM, Tharwat N, Gaballa GM, Elata MA, Amer T. Diagnostic Accuracy of Multiparametric Magnetic Resonance Imaging for Differentiation Between Parotid Neoplasms. *Can Assoc Radiol J* 2019; **70**: 264-272 [PMID: 30922790 DOI: 10.1016/j.carj.2018.10.010]
 - 16 **Zhang W**, Zuo Z, Luo N, Liu L, Jin G, Liu J, Su D. Non-enhanced MRI in combination with color Doppler flow imaging for improving diagnostic accuracy of parotid gland lesions. *Eur Arch Otorhinolaryngol* 2018; **275**: 987-995 [PMID: 29430614 DOI: 10.1007/s00405-018-4895-6]
 - 17 **Matsushima N**, Maeda M, Takamura M, Takeda K. Apparent diffusion coefficients of benign and malignant salivary gland tumors. Comparison to histopathological findings. *J Neuroradiol* 2007; **34**: 183-189 [PMID: 17568674 DOI: 10.1016/j.neurad.2007.04.002]
 - 18 **Faheem MH**, Shady S, Refaat MM. Role of magnetic resonance imaging (MRI) including diffusion weighted images (DWIs) in assessment of parotid gland masses with histopathological correlation. *Egypt J Radiol Nucl Med* 2018; **49**: 368-373 [DOI: 10.1016/j.ejrmm.2018.03.001]
 - 19 **Habermann CR**, Gossrau P, Graessner J, Arndt C, Cramer MC, Reitmeier F, Jaehne M, Adam G. Diffusion-weighted echo-planar MRI: a valuable tool for differentiating primary parotid gland tumors? *Rofa* 2005; **177**: 940-945 [PMID: 15973595 DOI: 10.1055/s-2005-858297]
 - 20 **Takumi K**, Fukukura Y, Hakamada H, Ideue J, Kumagae Y, Yoshiura T. Value of diffusion tensor imaging in differentiating malignant from benign parotid gland tumors. *Eur J Radiol* 2017; **95**: 249-256 [PMID: 28987676 DOI: 10.1016/j.ejrad.2017.08.013]
 - 21 **Matsusue E**, Fujihara Y, Matsuda E, Tokuyasu Y, Nakamoto S, Nakamura K, Ogawa T. Differentiating parotid tumors by quantitative signal intensity evaluation on MR imaging. *Clin Imaging* 2017; **46**: 37-43 [PMID: 28704680 DOI: 10.1016/j.clinimag.2017.06.009]
 - 22 **Ogawa T**, Kojima I, Ishii R, Sakamoto M, Murata T, Suzuki T, Kato K, Nakanome A, Ohkoshi A, Ishida E, Kakehata S, Shiga K, Katori Y. Clinical utility of dynamic-enhanced MRI in salivary gland tumors: retrospective study and literature review. *Eur Arch Otorhinolaryngol* 2018; **275**: 1613-1621 [PMID: 29623392 DOI: 10.1007/s00405-018-4965-9]
 - 23 **Tsushima Y**, Matsumoto M, Endo K. Parotid and parapharyngeal tumours: tissue characterization with dynamic magnetic resonance imaging. *Br J Radiol* 1994; **67**: 342-345 [PMID: 8173873 DOI: 10.1259/0007-1285-67-796-342]
 - 24 **Yabuuchi H**, Fukuya T, Tajima T, Hachitanda Y, Tomita K, Koga M. Salivary gland tumors: diagnostic value of gadolinium-enhanced dynamic MR imaging with histopathologic correlation. *Radiology* 2003; **226**: 345-354 [PMID: 12563124 DOI: 10.1148/radiol.2262011486]
 - 25 **Hisatomi M**, Asaumi J, Yanagi Y, Unetsubo T, Maki Y, Murakami J, Matsuzaki H, Honda Y, Konouchi H. Diagnostic value of dynamic contrast-enhanced MRI in the salivary gland tumors. *Oral Oncol* 2007; **43**: 940-947 [PMID: 17257881 DOI: 10.1016/j.oraloncology.2006.11.009]
 - 26 **Sumi M**, Nakamura T. Head and neck tumours: combined MRI assessment based on IVIM and TIC analyses for the differentiation of tumors of different histological types. *Eur Radiol* 2014; **24**: 223-231 [PMID: 24013848 DOI: 10.1007/s00330-013-3002-z]

- 27 **Lam PD**, Kuribayashi A, Imaizumi A, Sakamoto J, Sumi Y, Yoshino N, Kurabayashi T. Differentiating benign and malignant salivary gland tumours: diagnostic criteria and the accuracy of dynamic contrast-enhanced MRI with high temporal resolution. *Br J Radiol* 2015; **88**: 20140685 [PMID: 25791568 DOI: 10.1259/bjr.20140685]
- 28 **Eida S**, Ohki M, Sumi M, Yamada T, Nakamura T. MR factor analysis: improved technology for the assessment of 2D dynamic structures of benign and malignant salivary gland tumors. *J Magn Reson Imaging* 2008; **27**: 1256-1262 [PMID: 18504743 DOI: 10.1002/jmri.21349]
- 29 **Xu Z**, Zheng S, Pan A, Cheng X, Gao M. A multiparametric analysis based on DCE-MRI to improve the accuracy of parotid tumor discrimination. *Eur J Nucl Med Mol Imaging* 2019; **46**: 2228-2234 [PMID: 31372671 DOI: 10.1007/s00259-019-04447-9]
- 30 **Huang N**, Xiao Z, Chen Y, She D, Guo W, Yang X, Chen Q, Cao D, Chen T. Quantitative dynamic contrast-enhanced MRI and readout segmentation of long variable echo-trains diffusion-weighted imaging in differentiating parotid gland tumors. *Neuroradiology* 2021; **63**: 1709-1719 [PMID: 34241661 DOI: 10.1007/s00234-021-02758-z]
- 31 **Yabuuchi H**, Kamitani T, Sagiyama K, Yamasaki Y, Hida T, Matsuura Y, Hino T, Murayama Y, Yasumatsu R, Yamamoto H. Characterization of parotid gland tumors: added value of permeability MR imaging to DWI and DCE-MRI. *Eur Radiol* 2020; **30**: 6402-6412 [PMID: 32613285 DOI: 10.1007/s00330-020-07004-3]
- 32 **Park SY**, Kim HJ, Cha W. Comparative Study of Dynamic Susceptibility Contrast Perfusion MR Images between Warthin's Tumor and Malignant Parotid Tumors. *Kosin Med J* 2019; **34**: 38 [DOI: 10.7180/kmj.2019.34.1.38]
- 33 **Abdel Razek AAK**, Mukherji SK. Imaging of Minor Salivary Glands. *Neuroimaging Clin N Am* 2018; **28**: 295-302 [PMID: 29622120 DOI: 10.1016/j.nic.2018.01.008]
- 34 **Fujima N**, Kudo K, Tsukahara A, Yoshida D, Sakashita T, Homma A, Tha KK, Shirato H. Measurement of tumor blood flow in head and neck squamous cell carcinoma by pseudo-continuous arterial spin labeling: comparison with dynamic contrast-enhanced MRI. *J Magn Reson Imaging* 2015; **41**: 983-991 [PMID: 25787123 DOI: 10.1002/jmri.24885]
- 35 **Razek AAKA**. Multi-parametric MR imaging using pseudo-continuous arterial-spin labeling and diffusion-weighted MR imaging in differentiating subtypes of parotid tumors. *Magn Reson Imaging* 2019; **63**: 55-59 [PMID: 31422165 DOI: 10.1016/j.mri.2019.08.005]
- 36 **Rosenkrantz AB**, Padhani AR, Chenevert TL, Koh DM, De Keyzer F, Taouli B, Le Bihan D. Body diffusion kurtosis imaging: Basic principles, applications, and considerations for clinical practice. *J Magn Reson Imaging* 2015; **42**: 1190-1202 [PMID: 26119267 DOI: 10.1002/jmri.24985]
- 37 **Qian W**, Xu XQ, Zhu LN, Ma G, Su GY, Bu SS, Wu FY. Preliminary study of using diffusion kurtosis imaging for characterizing parotid gland tumors. *Acta Radiol* 2019; **60**: 887-894 [PMID: 30259752 DOI: 10.1177/0284185118803784]
- 38 **Abdel Razek AA**, Poptani H. MR spectroscopy of head and neck cancer. *Eur J Radiol* 2013; **82**: 982-989 [PMID: 23485098 DOI: 10.1016/j.ejrad.2013.01.025]
- 39 **King AD**, Yeung DK, Ahuja AT, Tse GM, Yuen HY, Wong KT, van Hasselt AC. Salivary gland tumors at *in vivo* proton MR spectroscopy. *Radiology* 2005; **237**: 563-569 [PMID: 16244265 DOI: 10.1148/radiol.2372041309]
- 40 **El-Naggar AK**, Chan JKC, Grandis JR, Takata T, Slootweg PJ. WHO classification of head and neck tumours. 4th ed. Lyon: International Agency for Research on Cancer, 2017: 159-201
- 41 **Speight PM**, Barrett AW. Salivary gland tumours: diagnostic challenges and an update on the latest WHO classification. *Diagn Histopathol* 2020; **26**: 147-158 [DOI: 10.1016/j.mpdhp.2020.01.001]
- 42 **Speight PM**, Barrett AW. Salivary gland tumours. *Oral Dis* 2002; **8**: 229-240 [PMID: 12363107 DOI: 10.1034/j.1601-0825.2002.02870.x]
- 43 **Branstetter BF**. Benign tumors. Parotid space. In: Hansberger HR. Diagnostic Imaging: Head and Neck. 2nd ed. Canada: Amirsys, 2011; 5: 5-28
- 44 **Kato H**, Kawaguchi M, Ando T, Mizuta K, Aoki M, Matsuo M. Pleomorphic adenoma of salivary glands: common and uncommon CT and MR imaging features. *Jpn J Radiol* 2018; **36**: 463-471 [PMID: 29845358 DOI: 10.1007/s11604-018-0747-y]
- 45 **Ito FA**, Jorge J, Vargas PA, Lopes MA. Histopathological findings of pleomorphic adenomas of the salivary glands. *Med Oral Patol Oral Cir Bucal* 2009; **14**: E57-E61 [PMID: 19179950]
- 46 **Kessler AT**, Bhatt AA. Review of the Major and Minor Salivary Glands, Part 2: Neoplasms and Tumor-like Lesions. *J Clin Imaging Sci* 2018; **8**: 48 [PMID: 30546932 DOI: 10.4103/jcis.JCIS_46_18]
- 47 **Tsushima Y**, Matsumoto M, Endo K, Aihara T, Nakajima T. Characteristic bright signal of parotid pleomorphic adenomas on T2-weighted MR images with pathological correlation. *Clin Radiol* 1994; **49**: 485-489 [PMID: 8088045 DOI: 10.1016/s0009-9260(05)81748-9]
- 48 **Ginat DT**. Imaging of Benign Neoplastic and Nonneoplastic Salivary Gland Tumors. *Neuroimaging Clin N Am* 2018; **28**: 159-169 [PMID: 29622111 DOI: 10.1016/j.nic.2018.01.002]
- 49 **Zaghi S**, Hendizadeh L, Hung T, Farahvar S, Abemayor E, Sepahdari AR. MRI criteria for the diagnosis of pleomorphic adenoma: a validation study. *Am J Otolaryngol* 2014; **35**: 713-718 [PMID: 25128908 DOI: 10.1016/j.amjoto.2014.07.013]
- 50 **Kato H**, Kanematsu M, Watanabe H, Mizuta K, Aoki M. Salivary gland tumors of the parotid gland: CT and MR imaging findings with emphasis on intratumoral cystic components. *Neuroradiology* 2014; **56**: 789-795 [PMID: 24948426 DOI: 10.1007/s00234-014-1386-3]
- 51 **Mukai H**, Motoori K, Horikoshi T, Takishima H, Nagai Y, Okamoto Y, Uno T. Basal cell adenoma of the parotid gland; MR features and differentiation from pleomorphic adenoma. *Dentomaxillofac Radiol* 2016; **45**: 20150322 [PMID: 26837669 DOI: 10.1259/dmfr.20150322]
- 52 **Zheng N**, Li R, Liu W, Shao S, Jiang S. The diagnostic value of combining conventional, diffusion-weighted imaging and dynamic contrast-enhanced MRI for salivary gland tumors. *Br J Radiol* 2018; **91**: 20170707 [PMID: 29902075 DOI: 10.1259/bjr.20170707]
- 53 **Khamis MEM**, Ahmed AF, Ismail EI, Bayomy MF, El-Anwar MW. The diagnostic efficacy of apparent diffusion coefficient value and Choline/Creatine ratio in differentiation between parotid gland tumors. *Egypt J Radiol Nucl Med* 2018; **49**: 358-367 [DOI: 10.1016/j.ejrnm.2018.02.004]
- 54 **Espinoza S**, Halimi P. Interpretation pearls for MR imaging of parotid gland tumor. *Eur Ann Otorhinolaryngol Head Neck*

- Dis* 2013; **130**: 30-35 [PMID: 22819222 DOI: 10.1016/j.anorl.2011.12.006]
- 55 **Hisatomi M**, Asaumi J, Yanagi Y, Konouchi H, Matsuzaki H, Honda Y, Kishi K. Assessment of pleomorphic adenomas using MRI and dynamic contrast enhanced MRI. *Oral Oncol* 2003; **39**: 574-579 [PMID: 12798400 DOI: 10.1016/s1368-8375(03)00040-x]
- 56 **Kato H**, Fujimoto K, Matsuo M, Mizuta K, Aoki M. Usefulness of diffusion-weighted MR imaging for differentiating between Warthin's tumor and oncocytoma of the parotid gland. *Jpn J Radiol* 2017; **35**: 78-85 [PMID: 28074380 DOI: 10.1007/s11604-016-0608-5]
- 57 **Ikeda M**, Motoori K, Hanazawa T, Nagai Y, Yamamoto S, Ueda T, Funatsu H, Ito H. Warthin tumor of the parotid gland: diagnostic value of MR imaging with histopathologic correlation. *AJNR Am J Neuroradiol* 2004; **25**: 1256-1262 [PMID: 15313720]
- 58 **Minami M**, Tanioka H, Oyama K, Itai Y, Eguchi M, Yoshikawa K, Murakami T, Sasaki Y. Warthin tumor of the parotid gland: MR-pathologic correlation. *AJNR Am J Neuroradiol* 1993; **14**: 209-214 [PMID: 8427092]
- 59 **Ding J**, Wang W, Peng W, Zhou X, Chen T. MRI and CT imaging characteristics of myoepithelioma of the parotid gland. *Acta Radiol* 2016; **57**: 837-843 [PMID: 26508793 DOI: 10.1177/0284185115609364]
- 60 **Sepúlveda I**, Platin E, Spencer ML, Mucientes P, Frelinghuysen M, Ortega P, Ulloa D. Oncocytoma of the parotid gland: a case report and review of the literature. *Case Rep Oncol* 2014; **7**: 109-116 [PMID: 24707257 DOI: 10.1159/000359998]
- 61 **Hisatomi M**, Asaumi J, Konouchi H, Yanagi Y, Matsuzaki H, Kishi K. Assessment of dynamic MRI of Warthin's tumors arising as multiple lesions in the parotid glands. *Oral Oncol* 2002; **38**: 369-372 [PMID: 12076701 DOI: 10.1016/s1368-8375(01)00073-2]
- 62 **Sakai E**, Yoda T, Shimamoto H, Hirano Y, Kusama M, Enomoto S. Pathologic and imaging findings of an oncocytoma in the deep lobe of the left parotid gland. *Int J Oral Maxillofac Surg* 2003; **32**: 563-565 [PMID: 14759120]
- 63 **Iida E**, Wiggins RH 3rd, Anzai Y. Bilateral parotid oncocytoma with spontaneous intratumoral hemorrhage: a rare hypervascular parotid tumor with ASL perfusion. *Clin Imaging* 2016; **40**: 357-360 [PMID: 27133667 DOI: 10.1016/j.clinimag.2016.02.003]
- 64 **Weitzel M**, Cohn JE, Spector H. Myoepithelioma of the Parotid Gland: A Case Report with Review of the Literature and Classic Histopathology. *Case Rep Otolaryngol* 2017; **2017**: 6036179 [PMID: 28900549 DOI: 10.1155/2017/6036179]
- 65 **Shimizu K**, Iwai H, Ikeda K, Sakaida N, Sawada S. Intraparotid facial nerve schwannoma: a report of five cases and an analysis of MR imaging results. *AJNR Am J Neuroradiol* 2005; **26**: 1328-1330 [PMID: 15956491]
- 66 **Chikui T**, Yonetsu K, Yoshiura K, Miwa K, Kanda S, Ozeki S, Shinohara M. Imaging findings of lipomas in the orofacial region with CT, US, and MRI. *Oral Surg Oral Med Oral Pathol Oral Radiol Endod* 1997; **84**: 88-95 [PMID: 9247958 DOI: 10.1016/s1079-2104(97)90302-4]
- 67 **Agaimy A**, Ihrler S, Märkl B, Lell M, Zenk J, Hartmann A, Michal M, Skalova A. Lipomatous salivary gland tumors: a series of 31 cases spanning their morphologic spectrum with emphasis on sialolipoma and oncocytic lipoadenoma. *Am J Surg Pathol* 2013; **37**: 128-137 [PMID: 23232852 DOI: 10.1097/PAS.0b013e31826731e0]
- 68 **Lara-Sánchez H**, Peral-Cagigal B, Madrigal-Rubiales B, Verrier-Hernández A. Cavernous hemangioma of the parotid gland in adults. *J Clin Exp Dent* 2014; **6**: e592-e594 [PMID: 25674332 DOI: 10.4317/jced.51750]
- 69 **Salama AA**, El-Barbary AH, Mlees MA, Esheba GES. Value of apparent diffusion coefficient and magnetic resonance spectroscopy in the identification of various pathological subtypes of parotid gland tumors. *Egypt J Radiol Nucl Med* 2015; **46**: 45-52 [DOI: 10.1016/j.ejmm.2014.09.005]
- 70 **Kashiwagi N**, Nakatsuka SI, Murakami T, Enoki E, Yamamoto K, Nakanishi K, Chikugo T, Kurisu Y, Kimura M, Hyodo T, Tsukabe A, Kakigi T, Tomita Y, Ishii K, Narumi Y, Yagyu Y, Tomiyama N. MR imaging features of mammary analogue secretory carcinoma and acinic cell carcinoma of the salivary gland: a preliminary report. *Dentomaxillofac Radiol* 2018; **47**: 20170218 [PMID: 29493279 DOI: 10.1259/dmfr.20170218]
- 71 **Skálová A**, Vanecek T, Sima R, Laco J, Weinreb I, Perez-Ordóñez B, Starek I, Geierova M, Simpson RH, Passador-Santos F, Ryska A, Leivo I, Kinkor Z, Michal M. Mammary analogue secretory carcinoma of salivary glands, containing the ETV6-NTRK3 fusion gene: a hitherto undescribed salivary gland tumor entity. *Am J Surg Pathol* 2010; **34**: 599-608 [PMID: 20410810 DOI: 10.1097/PAS.0b013e3181d9efcc]
- 72 **Kurokawa R**, Kurokawa M, Baba A, Ota Y, Moritani T, Srinivasan A. Radiological features of head and neck mammary analogue secretory carcinoma: 11 new cases with a systematic review of 29 cases reported in 28 publications. *Neuroradiology* 2021; **63**: 1901-1911 [PMID: 34427706 DOI: 10.1007/s00234-021-02796-7]
- 73 **Khalele BA**. Systematic review of mammary analog secretory carcinoma of salivary glands at 7 years after description. *Head Neck* 2017; **39**: 1243-1248 [PMID: 28370824 DOI: 10.1002/hed.24755]
- 74 **Kashiwagi N**, Murakami T, Chikugo T, Tomita Y, Kawano K, Nakanishi K, Mori K, Tomiyama N. Carcinoma ex pleomorphic adenoma of the parotid gland. *Acta Radiol* 2012; **53**: 303-306 [PMID: 22287150 DOI: 10.1258/ar.2011.110389]
- 75 **Shum JW**, Emmerling M, Lubek JE, Ord RA. Parotid lymphoma: a review of clinical presentation and management. *Oral Surg Oral Med Oral Pathol Oral Radiol* 2014; **118**: e1-e5 [PMID: 24405648 DOI: 10.1016/j.oooo.2013.10.013]
- 76 **Wang J**, Takashima S, Takayama F, Kawakami S, Saito A, Matsushita T, Momose M, Ishiyama T. Head and neck lesions: characterization with diffusion-weighted echo-planar MR imaging. *Radiology* 2001; **220**: 621-630 [PMID: 11526259 DOI: 10.1148/radiol.2202010063]
- 77 **Asaumi J**, Yanagi Y, Hisatomi M, Matsuzaki H, Konouchi H, Kishi K. The value of dynamic contrast-enhanced MRI in diagnosis of malignant lymphoma of the head and neck. *Eur J Radiol* 2003; **48**: 183-187 [PMID: 14680911 DOI: 10.1016/S0720-048x(02)00347-9]
- 78 **Andreasen S**, Kiss K, Mikkelsen LH, Channir HI, Plaschke CC, Melchior LC, Eriksen JG, Wessel I. An update on head and neck cancer: new entities and their histopathology, molecular background, treatment, and outcome. *APMIS* 2019; **127**: 240-264 [PMID: 30811708 DOI: 10.1111/apm.12901]
- 79 **Motoori K**, Iida Y, Nagai Y, Yamamoto S, Ueda T, Funatsu H, Ito H, Yoshitaka O. MR imaging of salivary duct carcinoma. *AJNR Am J Neuroradiol* 2005; **26**: 1201-1206 [PMID: 15891184]
- 80 **Suto T**, Kato H, Kawaguchi M, Kobayashi K, Miyazaki T, Ando T, Noda Y, Hyodo F, Matsuo M, Ishihara H, Ogawa T.

- MRI findings of epithelial-myoepithelial carcinoma of the parotid gland with radiologic-pathologic correlation. *Jpn J Radiol* 2022; **40**: 578-585 [PMID: 34982376 DOI: 10.1007/s11604-021-01243-0]
- 81 **Wang H**, Hoda RS, Faquin W, Rossi ED, Hotchandani N, Sun T, Pusztaszeri M, Bizzarro T, Bongiovanni M, Patel V, Jhala N, Fadda G, Gong Y. FNA biopsy of secondary nonlymphomatous malignancies in salivary glands: A multi-institutional study of 184 cases. *Cancer Cytopathol* 2017; **125**: 91-103 [PMID: 28001329 DOI: 10.1002/ency.21798]
- 82 **Horáková M**, Porre S, Tommola S, Baněčková M, Skálová A, Kholová I. FNA diagnostics of secondary malignancies in the salivary gland: Bi-institutional experience of 36 cases. *Diagn Cytopathol* 2021; **49**: 241-251 [PMID: 33017519 DOI: 10.1002/dc.24629]
- 83 **Mikaszewski B**, Markiet K, Smugała A, Stodulski D, Szurowska E, Stankiewicz C. Diffusion- and Perfusion-Weighted Magnetic Resonance Imaging-An Alternative to Fine Needle Biopsy or Only an Adjunct Test in Preoperative Differential Diagnostics of Malignant and Benign Parotid Tumors? *J Oral Maxillofac Surg* 2017; **75**: 2248-2253 [PMID: 28412261 DOI: 10.1016/j.joms.2017.03.018]

Amebic liver abscess: Clinico-radiological findings and interventional management

Rajeev Nayan Priyadarshi, Ramesh Kumar, Utpal Anand

Specialty type: Radiology, nuclear medicine and medical imaging

Provenance and peer review: Invited article; Externally peer reviewed.

Peer-review model: Single blind

Peer-review report's scientific quality classification

Grade A (Excellent): A
Grade B (Very good): 0
Grade C (Good): C
Grade D (Fair): D, D
Grade E (Poor): 0

P-Reviewer: Cerwenka H, Austria; Parzen-Johnson S, United States; Shelat VG, Singapore

Received: February 28, 2022

Peer-review started: February 28, 2022

First decision: May 9, 2022

Revised: May 30, 2022

Accepted: June 20, 2022

Article in press: June 20, 2022

Published online: August 28, 2022



Rajeev Nayan Priyadarshi, Department of Radiodiagnosis, All India Institute of Medical Sciences, Patna, Patna 801507, Bihar, India

Ramesh Kumar, Department of Gastroenterology, All India Institute of Medical Sciences, Patna, Patna 801507, Bihar, India

Utpal Anand, Department of Surgical Gastroenterology, All India Institute of Medical Sciences, Patna, Patna 801507, Bihar, India

Corresponding author: Ramesh Kumar, MD, Associate Professor, Department of Gastroenterology, All India Institute of Medical Sciences, Patna, Phulwari Sharif, Patna 801507, Bihar, India. docrameshkr@gmail.com

Abstract

In its classic form, amebic liver abscess (ALA) is a mild disease, which responds dramatically to antibiotics and rarely requires drainage. However, the two other forms of the disease, *i.e.*, acute aggressive and chronic indolent usually require drainage. These forms of ALA are frequently reported in endemic areas. The acute aggressive disease is particularly associated with serious complications, such as ruptures, secondary infections, and biliary communications. Laboratory parameters are deranged, with signs of organ failure often present. This form of disease is also associated with a high mortality rate, and early drainage is often required to control the disease severity. In the chronic form, the disease is characterized by low-grade symptoms, mainly pain in the right upper quadrant. Ultrasound and computed tomography (CT) play an important role not only in the diagnosis but also in the assessment of disease severity and identification of the associated complications. Recently, it has been shown that CT imaging morphology can be classified into three patterns, which seem to correlate with the clinical subtypes. Each pattern depicts its own set of distinctive imaging features. In this review, we briefly outline the clinical and imaging features of the three distinct forms of ALA, and discuss the role of percutaneous drainage in the management of ALA.

Key Words: Amebic liver abscess; Complicated liver abscess; Refractory liver abscess; Ruptured amebic liver abscess; Pleuropulmonary complication; Biliary communication; Needle aspiration; Catheter drainage

©The Author(s) 2022. Published by Baishideng Publishing Group Inc. All rights reserved.

Core Tip: The clinical presentation and imaging findings of amebic liver abscess (ALA) can be classified into three forms: subacute mild, acute aggressive and chronic indolent. The latter two forms are particularly associated with most complications of ALA. Despite this, prior literature primarily focused on the mild form of the disease, which responds well to antibiotics. To the best of our knowledge, there is no research on the types of ALA. In this review, the distinct clinical and imaging characteristics of each type are discussed in detail. With this understanding, the therapeutic strategy, medical or interventional, can be employed more efficiently for patients with ALA.

Citation: Priyadarshi RN, Kumar R, Anand U. Amebic liver abscess: Clinico-radiological findings and interventional management. *World J Radiol* 2022; 14(8): 272-285

URL: <https://www.wjgnet.com/1949-8470/full/v14/i8/272.htm>

DOI: <https://dx.doi.org/10.4329/wjr.v14.i8.272>

INTRODUCTION

Amebic liver abscess (ALA) is an infection caused by the protozoan *Entamoeba histolytica* (EH), an intestinal parasite. The infection is acquired by ingestion of water or food contaminated by EH cysts (the infective stage of the parasite). The cysts resist gastric juice and reach the distal ileum, where they undergo excystation producing trophozoites (the feeding stage of the parasite). In > 90% patients, the trophozoites feed on intestinal tissue and bacteria without producing symptoms. In less than 1% of cases, however, the trophozoites penetrate the mucosa and, through the portal route, reach the liver causing liver abscess[1]. ALA is the most common and has the highest mortality of amebiasis manifestations. It continues to remain the most common cause of liver abscess in developing and under-developed countries[2-6].

ALA was known as a progressive and deadly disease a century ago; however, since the introduction of modern antibiotics, the mortality has drastically reduced to between 1% and 3% [7]. Metronidazole is the most effective agent, with cure rates of approximately 90%. Most patients become asymptomatic within 72 to 96 h of treatment, and drainage adds no benefit to uncomplicated cases[7,8]. This fact seems to be more relevant for a typical case where the patient presents the classic and the most common form of the disease, *i.e.*, subacute mild disease. Reports from endemic areas have shown that a greater percentage of cases require drainage through either a needle or catheter. The reported prevalence of such cases varies from 44% to 80% [3-5,7,9-14]. A thorough literature search shows that two distinct clinical settings usually require drainage. In the first, the patients present acutely with severe and fulminant disease, and drainage is performed to control disease progression and prevent organ failure. Such abscesses, by different authors, have been denoted by different terms that indicate the aggressive nature of the disease, such as “acute aggressive ALA”, “severe ALA” or “fulminant ALA” [10,15-17]. In the second clinical setting of the disease, the patients present late with mild symptoms, usually tenderness; they usually have a large persistent abscess despite medical therapy. Various terms are used to describe such abscesses, such as “drug-resistant ALA”, “refractory ALA” or “chronic indolent ALA” [18-22]. Regardless of the presentations, most cases are usually associated with a few complications, such as rupture, secondary infection or biliary communication. Considering this fact, a few authors prefer referring to it as “complicated ALA” [13,14]. Therefore, ALA can be classified into three clinical subtypes: subacute mild, acute aggressive and chronic indolent. Not only do the ALAs have varied clinical presentations, but they are also associated with distinct imaging patterns[10].

This review describes the three major types of clinical presentations as well as three types of imaging patterns (correlating with clinical subtypes). Special emphasis has been placed on the two clinical types – acute aggressive and chronic indolent. This paper also discusses the complications of ALA and their percutaneous management.

OVERVIEW OF EPIDEMIOLOGY, RISK FACTORS AND PATHOGENESIS OF COMPLICATED ALA

Epidemiology

Although ALA occurs globally, most reports emerge from endemic countries, such as India, Sri Lanka, Bangladesh, Mexico, East and South Africa or parts of Central and South America[23]. A high endemicity in these countries is related to poor hygiene and sanitation since the parasite is transmitted *via* the fecal-oral route. Even in endemic countries, ALA occurs primarily in rural areas where defecation in the open air is a common practice[11,24-26]. The lack of adequate sewage disposal results in contamination of drinking water with EH cysts. Using polymerase chain reaction (PCR), a

population-based study from India detected the prevalence of EH in 14% of stool samples[27]. In developed countries, ALA occurs mostly in travelers or immigrants from endemic areas[28]. Apart from endemicity, several other epidemiological factors also increase the risk of developing complicated disease.

Risk factors

The disease is found almost exclusively in men (male: female > 10:1)[11]. The reason for this is unknown but several investigators have speculated that it might be related to alcohol, particularly those prepared locally from the sap of palm trees (toddy)[11,24,25,29]. Not only is the toddy a risk factor for ALA, but in many studies it has been linked to severe disease[13,30]. The exact mechanism by which it contributes to the pathogenesis of ALA is unclear. It has been proposed that alcohol may alter the gut mucosa or convert the pathogen to a more virulent strain or render the liver more susceptible to the infection[23,24,29]. Most cases occur in middle age ranging from 20 to 50 years[30]. In older patients, the disease tends to be more severe possibly due to their poor immunity, whereas it is rare in children[31]. Another factor contributing to the pathogenesis of ALA is malnutrition[11,13,23]. For centuries, the disease has been a symbol of poverty. A typical patient with ALA, as we have observed, is a thin emaciated villager of low socioeconomic status. Their poor nutritional status is evidenced by low albumin, BMI and hemoglobin [11]. ALA has also been shown to be severe in diabetic patients[16,32].

Pathogenesis

The term “amebic liver abscess” is a misnomer as the cavity formation or liquefaction is not due to suppuration; rather, it is the result of a unique type of necrosis[33,34]. The necrotic area appears as if it has been dissolved by chemical or toxin. Considering this morphological pattern, it was believed that the parasite possesses a toxin that lyses the hepatocytes, and therefore the parasite was named “histolytica” [35]. It is now known that several proteolytic enzymes released by the inflammatory cells are responsible for tissue destruction[7,36,37].

Understanding the gross morphology is important because it is characteristic and, to a large extent, can be extrapolated to imaging findings[35,38,39]. The gross appearance varies depending on the severity and the duration of the disease. In the early stage, it is that of a necrotic area where the center has liquefied necrotic tissue (chocolate-colored sterile “pus”); however, the periphery has more solid tissue[10,35,38-40]. The peripheral solid and partially liquified tissue is responsible for the shaggy or ragged appearance on the abscess wall[10,40]. A mature wall is absent and the tissue surrounding the abscess is congested, compressed and edematous[41]. There may be pressure over the surrounding liver parenchyma or the hepatic capsule. Venous thrombosis and ischemic infarction are commonly observed in fatal cases[42]. As the abscess heals, a fibrous wall forms and the cavity becomes more sharply defined[38,43]. The edema and congestion regress and the abscess wall is surrounded only by a thin rim of edema. The peripheral solid tissue becomes more liquefied, the content is gradually resorbed, and the lesion heals completely without scar. However, a complicated or a very large abscess can persist in the form of a residual abscess with a thick fibrous wall. A mature wall, as opposed to the ragged wall, indicates chronicity or secondary infection[42].

ALA is usually solitary, located in the right lobe of the liver. The size varies from a few centimeters to 20 cm[35]. However, the risk of complications increases with the number and size. In autopsy series, unlike successfully treated series, 60% of cases show multiple abscesses varying in size from 10 to 15 cm [35]. Literature shows a higher incidence of large (> 5 to 10 cm) and multiple abscesses (occurring in about 50% of cases) among the Southeast Asian population compared to other studied populations[8-11, 43-47].

CLINICAL PRESENTATION

The clinical presentation varies from mild to severe. Based on the duration and the severity, ALA can be classified into three main types: subacute mild, acute aggressive, and chronic indolent[10,15,23,28,48].

Subacute mild ALA

Most patients (approximately 80%) have a subacute course characterized by mild symptoms that develop in less than 2 to 4 wk[23,28,30,49-51]. The disease typically begins with fever and chills, right upper quadrant pain and tender hepatomegaly. Other symptoms include anorexia, weakness, nausea and diarrhea. There may be right shoulder pain when an abscess located in the posterosuperior segments irritates the diaphragm. The typical finding on physical examination is point tenderness in the intercostal spaces[31]. The disease is associated with no or minimal organ dysfunction; the laboratory parameters are near normal except mild to moderate leukocytosis. Dramatic improvement is observed after medical therapy and no further complications occur. This pattern of presentation has also been referred to as “acute benign ALA” by a few authors; however, the term “subacute mild” may be preferable as it correctly defines the clinical course of the disease[15,48]. Additionally, the term also differentiates it from the two other forms of the disease, *i.e.*, acute aggressive ALA and chronic indolent

ALA.

Acute aggressive ALA

Acute aggressive ALA is characterized by a more severe and rapidly progressive course. Considering the acuteness and severity of this form, Katzenstein *et al*[15] named it “acute aggressive ALA”. The prevalence of this type of ALA may be high in endemic areas[10]. In a study of 317 patients with ALA, Balasegaram reported acute fulminating infection in 13% of cases[17]. The patients often present more acutely (< 10 d) with signs of severe disease including systemic toxicity, high fevers and chills, and an exquisitely tender hepatomegaly[15]. Signs related to rupture and other complications may be present. In fact, rupture is a common presenting manifestation of aggressive ALA, occurring in up to 57% of patients[10]. The patients with free intraperitoneal rupture often have features of generalized peritonitis. Sepsis-like features can occur in more severely affected patients. Up to 90% of patients require hospitalization and about 13% require intensive care unit management[10]. Signs of organ dysfunction, such as jaundice, may also be observed in most patients[9,12,32]. Renal dysfunction can occur in 5% to 12% of cases[6,10]. Hepatic failure and encephalopathy may also occur. Approximately, one-third to one-half of the patients will have gross fluid derangements including ascites, pleural effusion and edema[5,9,10,13,52]. Patients with aggressive ALA are often misdiagnosed as having acute cholecystitis, appendicitis or bowel perforation[30,53-55].

Most patients with aggressive ALA will have markedly deranged laboratory parameters, such as severe leukocytosis, hyperbilirubinemia, hypoalbuminemia, elevated liver enzymes, and elevated alkaline phosphatase[10]. A high mortality has been recorded in this group of patients. Most deaths are usually related to intraperitoneal rupture, which is followed by sepsis and multiorgan failure. Many findings of aggressive disease have been identified as poor prognostic markers in different studies, such as multiple abscesses, large (> 500 cc) volume abscesses, presence of encephalopathy, hypoalbuminemia, and hyperbilirubinemia (> 3.5 mg/dL)[3,9,13,32]. Medical therapy alone is often suboptimal to control the disease and the laboratory tests do not return to near normal following treatment. Therefore, drainage with either a needle or catheter is usually required[10,15].

Chronic indolent ALA

Chronic presentation can occur in approximately 10 to 20% of cases[10,15,23,49,56,57]. This presentation has been designated in most studies as “chronic indolent ALA”. In this form, patients present late with mild symptoms for more than four weeks. Most patients complain of pain over the right lower chest or upper abdomen. Fever is usually absent or of low grade. However, a history of fever with chills at the onset of the disease may be obtained in most cases. Additionally, many patients will have a history of prior medical treatment or sometimes prior needle aspirations. On examination, right upper quadrant tenderness is usually present. Other low-grade symptoms include weight loss, anorexia, or malaise[10,15]. Laboratory tests are usually normal except elevated alkaline phosphatase level and low serum albumin. Leukocytosis in chronic abscesses suggests the presence of secondary infection, which is the most common complication in this form of the disease. In contrast to acute aggressive ALA, chronic ALA is rarely associated with intraperitoneal rupture.

LABORATORY EVALUATION

The diagnosis of ALA is based on recognition of the typical clinical features, imaging studies and serological tests. Serological tests are considered confirmatory (sensitivity > 94%; specificity > 95%)[7]. However, their usefulness in the diagnosis of acute ALA is limited in endemic areas because the tests remain positive for several months to years after resolution of infection. Moreover, the serological tests may be negative in the first seven to ten days of the infection, limiting their diagnostic use for acute ALA[7].

Routine laboratory tests in ALA are nonspecific and do not differ from those in pyogenic abscess[58,59]. However, these tests are useful in assessing the severity and monitoring the treatment response. In most patients with acute benign ALA, mild to moderate leukocytosis is found with an average WBC count of 16000/ μ L. However, a high WBC count above 20000/ μ L should suggest either aggressive, or secondarily infected abscesses[9,56,60]. In our series, a mean of 24000/ μ L was found in patients with aggressive abscesses. Serum bilirubin and liver enzyme (AST/ALT) levels are normal or minimally elevated in mild cases. When elevated, the AST/ALT levels return to normal following medical therapy. However, the alkaline phosphatase level is elevated in 70 to 80% of cases, regardless of the severity of the disease and the duration of presentation[56,60]. A very high value of bilirubin (> 3.5 mg/dL) and liver enzymes indicates complications or aggressive disease. A low serum albumin (< 2 g/dL) is found in almost all patients; however, an exceedingly low value is a poor prognostic marker[34]. Inflammatory biomarkers, such as C-reactive protein and procalcitonin have been found to be nonspecifically raised in most patients with ALA[34,59,61].

IMAGING EVALUATION: IMAGING CLASSIFICATION AND CLINICORADIOLOGICAL CORRELATION

Chest radiographs, ultrasound, computed tomography (CT), and magnetic resonance imaging (MRI) are the most employed modalities for diagnosis of ALA. Radiographs are insensitive, non-specific and are abnormal in only half of cases[23]. They can reveal elevated diaphragm, pleural effusion and basal consolidation or atelectasis. MRI seems to offer no advantage over CT[33,62]. Of all radiological tests, ultrasound and CT are the most employed tools; in fact, they are complementary to one another in many ways. For example, ultrasound can detect the degrees of liquefaction, differentiating solid necrotic tissue from more liquefied tissue; this information is not provided by CT. Ultrasound, however, can fail to detect an early abscess when the lesion is not liquid enough to be visible[63]. CT is more sensitive in this regard. Another concern with ultrasound may be that early aggressive abscesses might be mistaken for necrotic malignant masses because they often contain solid (non-liquefied) necrotic material[8,38,39,47]. Due to its ability to differentiate viable tissue from necrotic tissue, contrast-enhanced CT can distinguish between necrotic mass and aggressive abscesses. Additionally, CT is useful in the identification of various complications associated with ALA. Although both ultrasound and CT are highly sensitive (ultrasound, 85%-95%; CT, 100%)[64], their specificity is low for differentiating ALA from other infective abscesses or necrotic masses[45].

The imaging features of ALA on CT have been described as round oval hypodense lesions with a rim enhancing wall and on sonography as hypoechoic or anechoic lesions with internal echoes. This classic description of ALA, however, does not take into account the entire spectrum of the imaging findings, which are known to vary considerably. The varied morphology has largely been shown to reflect the underlying pathological changes, which occur as ALA evolves through the different phases of maturation. Acute abscesses consist mainly of solid necrotic tissue and their edges are irregular or ragged. As the abscesses heal, there is formation of a distinct wall, edges become smooth, and the contents become more liquefied[10,38,43]. This morphologic variation has prompted several investigators to classify the imaging features of ALA into distinct types[46,65,66]. Most investigators have classified ALA into three types based on sonographic appearance. In 1987, Léonetti *et al*[65] divided the sonographic morphology into three stages: pre-suppurative stage (phase I), suppurative stage (phase II), and scarring stage (phase III). Subsequently, N'Gbesso *et al*[66] proposed a similar sonographic classification: non-collected ALA (type I), collected ALA (type II), and healed ALA (type III).

On MRI, a variable degree of wall formation and edema surrounding ALA have been reported according to the status of abscess healing. Elizondo *et al*[43], who examined 29 ALAs with MRI, reported that untreated ALAs are associated with an incomplete ring (corresponding to incomplete wall) and diffuse or wedge-shaped perilesional edema. Following successful treatment, the ring formation is complete and the edema regresses to form concentric rings around the abscess. Matching with the MRI findings, a double-target sign has been described on contrast-enhanced CT; the inner ring corresponds to the enhancing wall and the outer ring to the perilesional edema[10,67].

Our recent experience suggests that the latest generation CT can effectively evaluate several imaging characteristics, such as wall formation, degree of liquefaction, enhancement patterns, septa, or perilesional hypodensity[10]. These characteristics can provide considerable information on the patient's clinical status. It appears that imaging findings of ALA can be classified into three distinct but overlapping patterns (type I, II and III) that correlate well with the clinical subtypes (Table 1)[10]. This classification may be useful for identifying those abscesses that would require more aggressive treatment.

Type I: ALA with ragged edges

Type I pattern is observed in patients with acute aggressive ALA. It is characterized by incomplete or absent walls and ragged edges (Figure 1A). This pattern is observed in patients with acute aggressive ALA. Type I pattern indicates an early and progressive abscess, with no sign of healing. Surrounding the abscess, there is a diffuse or wedge-shaped hypodensity, which is usually due to the combined effect of hypoperfusion and edema[10,68]. Most cases show irregular and interrupted enhancement at the edges. Multiple irregular septa may be observed at the periphery, indicating the viable parenchyma that is yet to be necrotic[10]. On sonography, they appear heterogeneous due to the presence of both solid and liquefied necrotic tissue[38,47]. The heterogeneity accounts for the frequent misdiagnosis of aggressive ALA as malignant lesions[10,38,47,67]. Other imaging features often associated with type I morphology are large size, multiplicity, and irregular shape (due to coalescence of multiple lesions)[10].

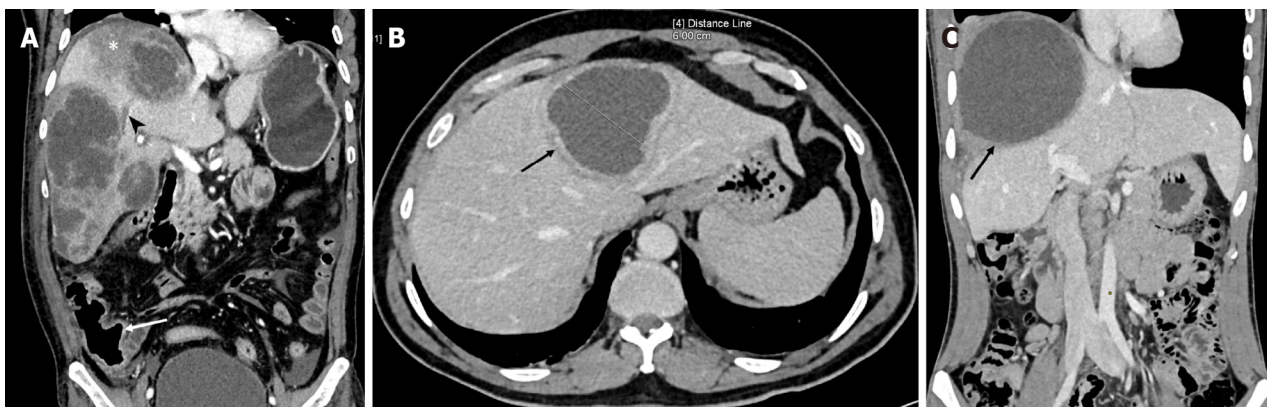
Type II: ALA with a complete rim enhancing wall

Type II pattern indicates subacute mild ALA. It is characterized by a well-defined enhancing wall (Figure 1B). The rim enhancement of the wall indicates active granulation tissue, a pathological sign of inflammation and beginning of healing[43]. A thin rim of edema surrounding the wall (in contrast to the more widespread edema of type I pattern) may be observed to form a perilesional "halo" on contrast CT. In many cases, a double-target sign (the inner ring of wall enhancement and outer ring of hypodense edema) is identified. The content is more liquefied and homogeneous compared to those

Table 1 Distinguishing clinical findings, imaging features and treatment strategy of the three forms of amebic liver abscesses

	Acute aggressive	Subacute mild	Chronic indolent
Presentation	Acute (< 10 d)	Subacute (< 2-4 wk)	Chronic (> 4 wk)
Symptoms	Severe symptoms (RUQ pain, fever, toxicity, abdominal distention, leg edema, shock-like syndrome resembling sepsis, jaundice, signs of intraperitoneal or intrathoracic rupture)	Moderate symptoms (usually intermittent fever and RUQ tenderness)	Mild (usually RUQ tenderness, fever if secondary infection)
Laboratory tests	Marked leukocytosis (> 20000/ μ L), abnormal LFT, features of organ failure (hyperbilirubinemia, renal dysfunction)	Transient leukocytosis and transient elevation of LFT (returns to normal after treatment)	Usually normal
Imaging features	Incomplete or absent wall, ragged edge, interrupted or no enhancement, septations, heterogeneous content, widespread or wedge-shaped perilesional hypodensity	Relatively smooth outline, rim-enhancing wall with perilesional hypodense "halo" (double-target sign)	Smooth outline, thick non-enhancing wall, faint or no perilesional "halo"
Size and number	> 5-10 cm, multiple in over 50% of cases	< 5-10 cm, usually single	> 5-10 cm, usually single
Treatment	Antibiotics; Early drainage is often required to control severity	Antibiotic alone suffices in most cases; rapid recovery, drainage when symptoms persist	Mostly pre-treated with antibiotics, drainage not required unless pressure symptoms or secondary infection present

RUQ: Right upper quadrant; LFT: Liver function test.



DOI: 10.4329/wjr.v14.i8.272 Copyright ©The Author(s) 2022.

Figure 1 Computed tomography images. A: Computed tomography (CT) (coronal image) demonstrating the characteristic imaging findings of an acute aggressive abscess (type I pattern) in a 60-year-old man who presented with sepsis-like features and markedly deranged laboratory parameters. There are multiple abscesses in the right lobe with irregular ragged edges, multiple septa and heterogeneous densities indicating partially liquefied tissue. Also, note the presence of a hypodense area in the surrounding parenchyma (asterisk) and right hepatic vein thrombosis (arrowhead). The thickened cecal wall (arrow) and mild ascites are also evident; B: CT of a typical case of subacute mild disease. The laboratory profile was near normal. The axial image shows an abscess in the left lobe with a well-defined wall showing rim enhancement (type II pattern). This patient presented with mild abdominal pain after 20 d of symptoms; C: CT image of a chronic indolent abscess (type III pattern). Coronal image of a 24-year-old man showing a large abscess with a thick non-enhancing wall in the right lobe. He had persistent pain in the right upper quadrant for two months despite complete resolution of fever and normalization of laboratory tests after metronidazole therapy.

presenting acutely. This pattern is nonspecific and resembles pyogenic abscesses[43,69,70].

Type III: ALA with a nonenhancing wall

Type III pattern represents chronic indolent ALA. It is characterized by a thick fibrotic wall that is much smoother and does not enhance with contrast (Figure 1C). The absence of contrast enhancement excludes active inflammation. This pattern, in fact, represents persistence of amebic pus (usually more than four weeks), in which the liver fails to clear the necrotic tissue. The abscesses in this form are usually asymptomatic; however, when they are large enough to cause capsular stretching, they can cause right upper quadrant pain. Clinicians should be aware that healed ALAs in this pattern often resemble cysts and can persist for months or years following successful treatment[46,66,71,72].

COMPLICATIONS: CLINICO-RADIOLOGICAL FINDINGS

Rupture

The most feared complication of ALA is rupture. The overall incidence ranges from 6 to 40% [10,44,52,73]. ALA generally ruptures into the thoracic cavity or intraperitoneal space. Occasionally, the abscess can rupture into hollow viscera, such as the stomach, duodenum, or colon [20,60,74,75]. Of all ruptures, the gravest, but fortunately rare, is rupture into the pericardium [49]. In our experience, the risk of free intraperitoneal ruptures is high when the abscesses present acutely (type I pattern). However, intrathoracic ruptures, particularly the intrapulmonary ones, are noted more frequently in chronic cases (type II or III pattern). This may be due to development of adhesion between the diaphragm and pleura in older abscesses [10].

Intrathoracic rupture: Pleural empyema, lung abscess, hepatobronchial fistula

Pleuropulmonary rupture occurs in 7% to 20% of patients [7,56,57]. The abscesses located inferior to the diaphragm can perforate it to enter the pleural space causing amebic empyema, which is the most common intrathoracic complication. It is important that pleural empyema be differentiated from sterile pleural effusion, which occurs more frequently than empyema. The sterile effusion is reactionary and resolves spontaneously, and therefore, it requires no drainage [57]. The presence of loculations and septations on ultrasound indicate amebic empyema [11]. The next intrathoracic complication is the development of lung consolidation or lung abscess, which occurs when an abscess directly ruptures into lung parenchyma invading through both the diaphragm and pleura. The lung abscess may, in turn, communicate with the bronchi to cause hepatobronchial fistula or with pleura to cause bronchopleural fistula. Bronchial communication has been reported to occur in over one-third of thoracic complications [76]. The presence of air in the lung abscess or liver abscess or in the pleural collections indicates these fistulous complications (Figure 2) [11]. Clinically, the patients complain of productive cough, often expectoration of amebic pus-like material. The pleuropulmonary rupture is considered less severe than the intraperitoneal rupture because of spontaneous drainage of the abscesses following the hepatobronchial fistula.

Intraperitoneal rupture: Contained rupture versus free rupture

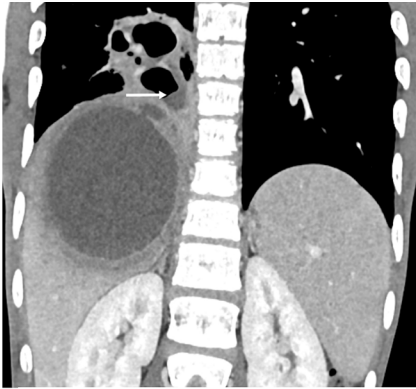
Intraperitoneal rupture has been said to occur in only 7% of cases [7,56,57]. However, we found an incidence of intraperitoneal rupture of 33% in our series [10]. In fact, several series from endemic countries have reported similar findings [6,13,17]. Based on imaging findings, intraperitoneal ruptures can be divided into two types: contained rupture and free rupture [11,60]. The contained rupture is characterized by accumulation of the localized fluid collection around the liver, usually in the subphrenic or subhepatic space (Figure 3A) [11]. The localized fluid from the contained rupture may occasionally be palpable on abdominal examination. This type of rupture carries a good prognosis and fortunately, is more common than its counterpart – the free rupture. The free rupture is characterized by fluid collection that diffusely involves the entire peritoneal cavity; it can cause generalized peritonitis and carry a poor prognosis (Figure 3B). The differentiation between these two types is significant as more aggressive treatment for longer duration is required for free ruptures [11,21].

Biliary complication: Communication versus compression

A common cause of drug failure is the presence of biliary complications, which has been reported to occur in up to 27% of refractory cases [12,22,77]. This occurs either from ductal communication with the abscess or from external compression by a large abscess [12,41]. When the liver parenchyma is destroyed by an aggressive abscess, the bile ducts are also damaged, producing ductal communications [12]. Usually, the communication is subtle, and therefore, ductal dilatation may not be evident on imaging. In several cases, the diagnosis is made only during percutaneous drainage when the initial aspirated fluid is bilious or when bile (usually persistent) appears thereafter [11,22,77]. Uncommonly, an abscess, particularly when large and aggressive, can rupture into the central bile ducts, causing duct dilation (Figure 4). In such cases, the diagnosis may be confirmed when endoscopic retrograde cholangiopancreatography (ERCP) or cavitogram demonstrates contrast extravasation into the abscess cavity [22,55]. Usually, the bile ducts are compressed by a large abscess, resulting in biliary duct dilation; these cases are evident on ultrasound or CT. The size and location of an abscess on imaging can provide anatomic clues to the presence of a biliary complication. The large (> 5 to 10 cm) and centrally located abscesses (near porta hepatis) are more likely to have biliary complications than those smaller and with subcapsular locations [12]. Clinically, the presence of high jaundice may indicate biliary complications. Agarwal *et al* [22] compared the abscesses with and without biliary communications and found that total bilirubin levels > 2 mg/dL were present only in the patients with biliary complications.

Secondary bacterial infection

ALA is typically sterile. However, in 10% to 20% of cases, it can be complicated by secondary bacterial infections [58,78,79]. The incidence may be higher than generally recognized. Recently, in a PCR based study from liver aspirates, Singh *et al* [2] found bacterial infection in 37% of cases, mostly anaerobes of



DOI: 10.4329/wjrr.v14.i8.272 Copyright ©The Author(s) 2022.

Figure 2 Computed tomography image (coronal view) of a patient who presented with productive cough and mild upper abdominal pain for more than four weeks. Note the rupture of a subdiaphragmatic abscess into the lung resulting in the formation of a lung abscess. The air-fluid level in the lung abscess (arrow) indicates fistulous communication between the lung abscess and the bronchus.



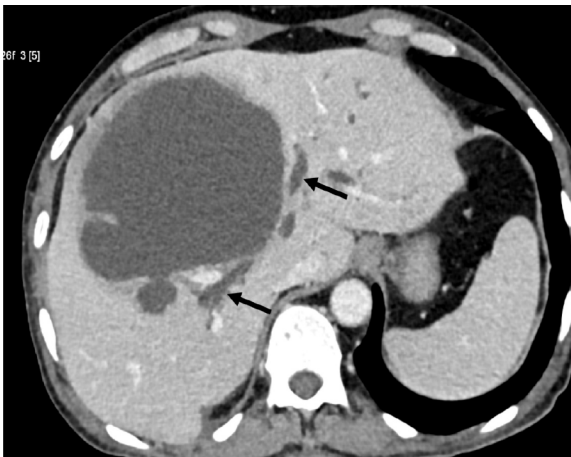
DOI: 10.4329/wjrr.v14.i8.272 Copyright ©The Author(s) 2022.

Figure 3 Computed tomography image. A: Computed tomography image (coronal view) demonstrating a contained rupture. A fluid collection that is localized in the subphrenic space (asterisk). Note the wide rent in the abscess (arrow). Additional imaging features of an aggressive disease in this image are the presence of ascites and thrombus in a segment of the hepatic vein (arrowhead); B: Free intraperitoneal rupture in a 40-year-old man who presented with features of generalized peritonitis. Coronal computed tomography image showing a large amebic abscess with an irregular edge in the right lobe and diffuse intraperitoneal fluid collection (arrows).

intestinal microbiota. The authors suggested that intestinal bacteria reach the liver along with the trophozoites through the portal route, that is, concurrent or coinfection with bacteria. When secondary bacterial infection occurs as coinfection, the disease may take an aggressive course. This complication should be suspected in refractory cases, particularly those associated with persistent high fever and marked leukocytosis ($> 20000/\mu\text{L}$) [56]. Another mechanism of secondary infection is bacterial superinfection, which usually occurs in the stagnant fluid following unsuccessful needle aspiration or inadequate catheter drainage [18]. Since most of the abscesses are walled off at this point, symptoms are of chronic indolent disease. In contrast to sterile amebic aspirate, cultures of pus from secondarily infected ALA usually yield positive results. Blood cultures, however, may be negative because most patients are generally pretreated with antibiotics [80].

Vascular complication: Venous thrombosis, venous compression and arterial aneurysm

Venous thrombosis is a common phenomenon in this disease. Autopsy studies have shown that venous thrombosis occurs in up to 30% of cases; however, we have identified venous thrombus in 70% of cases with the use of the latest multidetector CT [42,68]. Venous thrombosis may involve the portal or hepatic vein, but usually both are involved. Thrombus typically occurs in the smaller segmental or subsegmental branches. The hepatic vein thrombosis can extend into the inferior vena cava (IVC) or even into the right atrium [68]. Rarely, it can cause a Budd-Chiari like syndrome [81]. Detection of thrombus in large veins may be indicative of severe ALA [68,82]. The diagnosis of thrombosis on CT can be suggested by the presence of a wedge-shaped hypoattenuating area surrounding the abscess, which might be due to thrombosis led hypoperfusion [68]. Another vascular complication is compression of the intrahepatic veins and the IVC. Venous compression may be a clue to the presence of a high intracavitary pressure in



DOI: 10.4329/wjr.v14.i8.272 Copyright ©The Author(s) 2022.

Figure 4 Axial computed tomography of a 60-year-old man showing a large abscess in segment IV of the liver near the porta hepatis. Note the duct dilation (arrows) that resulted from rupture of the abscess into the central bile ducts. He was managed with catheter drainage. Bilious fluid draining through the catheter was observed for several weeks in this patient.

the abscess, which in turn indicates aggressive abscesses. IVC compression occurs when a large abscess located in the caudate lobe compresses the IVC, causing leg edema[48]. Additionally, portal vein compression near the porta hepatis has been reported to cause splenomegaly and portal hypertension [41]. Hepatic artery pseudoaneurysm is a rare, but serious complication of ALA that results from erosion of the arterial wall by an aggressive abscess[83].

Concurrent colitis and perforations

Although diarrhea is found in only 15% to 30% of patients with ALA, concurrent colonic ulcers are detected in approximately 50% of patients with ALA on colonoscopy[17,57,84,85]. The colonic lesions on colonoscopy appear as small discrete ulcers in the cecum or ascending colon. Approximately 70% of the ulcers are localized to cecum and contiguous involvement of the appendix (amebic typhlo-appendicitis) is common[10]. As the ulcers are usually small and localized, symptoms related to colitis are mild. In severe cases, however, other segments may also be involved or there may be cecal perforations. Furthermore, the severity of colitis seems to parallel the severity of abscesses. Recently, Premkumar *et al* [85], in a study of 52 patients with ALA, reported bleeding and large ileocecal ulcers in the majority of their patients; most synchronous ALAs in this series had aggressive clinical and imaging features. In an autopsy study of 76 patients with fatal ALA, Aikat *et al*[42] found that the incidence of colonic ulcers was 62%. With multidetector CT, we have observed concurrent colitis in 28% of patients, more frequently and possibly more severe in the patients with aggressive ALA than those with mild ALA. On CT, colitis generally manifests as nonspecific bowel wall thickening (Figure 1A)[10].

MANAGEMENT: ROLE OF IMAGE-GUIDED PERCUTANEOUS DRAINAGE

ALA, in most patients, is mild and responds promptly to medical therapy. The drug of choice for the treatment of ALA is metronidazole, a nitroimidazole, which is given at a dose of 750 mg orally or intravenously three times daily for seven to ten days[31]. This regime results in resolution of fever, toxemia, and pain in 80% to 90% of patients with uncomplicated ALA within 72 to 96 h of treatment[7]. The disease resolves without complications or without the need for any invasive procedures. This treatment is followed by a luminal agent (paromomycin or diloxanide furoate) to clear the luminal parasites.

The decision to perform drainage is based largely on the clinical grounds. Any symptomatic patient with persistent symptoms after four days of treatment requires drainage, regardless of the imaging findings. In the most common scenario of percutaneous drainage, the patients continue to have symptoms, primarily pain or tenderness in the right upper quadrant, despite completed medical therapy. In another clinical setting, early drainage is performed for acute aggressive abscesses to control the disease severity[10]. The third clinical setting may be the patients in whom there is diagnostic uncertainty between ALA and pyogenic abscess. In such cases, most physicians prefer to drain the amebic abscesses considering them as a pyogenic abscess.

In addition to clinical criteria, imaging-based criteria for the use of drainage was formulated by de la Rey Nel *et al*[86]. They recommended that abscesses with the following risk factors should be drained: abscesses > 10 cm (because of their long healing time), abscesses located in the left lobe (because of the

risk of rupture into the pericardium), and large superficial abscesses with a thin rim (because of the risk of rupture). In this context, it must be emphasized that lack of a mature wall is also an important risk factor that must be considered while assessing rupture risk. Most intraperitoneal ruptures in our series occurred when the abscesses lacked a mature wall[10].

Needle aspiration vs catheter drainage

Percutaneous drainage can be performed either by needle aspiration or catheter drainage under image guidance. Usually, sonographic guidance suffices for the placement of the catheter or needle into the abscess cavity[11]. CT guidance may be required in some cases, particularly in thoracic complications. Success of the procedure is dependent on its effectiveness in evacuation of the amebic pus. Needle aspiration is a simple, less invasive technique and requires less expertise. However, it is not as effective as catheter drainage, and presents several disadvantages. It fails to evacuate the solid necrotic tissue, which usually blocks the needle lumen during aspiration. Since tissue necrosis and its liquefaction is a dynamic process, not all tissue is completely liquid at the time of aspiration, and therefore, multiple sessions are generally needed to achieve complete drainage. This practice is perhaps related to the most serious drawback of needle aspiration, *i.e.*, bacterial superinfections. The reported rate of superinfections following needle aspirations is 15% [18]. Nevertheless, needle aspirations may be useful in the appropriate settings, such as when the abscesses are small (< 5 cm) and the content is completely liquefied. Another common scenario includes multiple abscesses, where smaller and more liquefied abscesses are aspirated using an 18G spinal needle, whereas the larger and partially necrotic abscesses are drained using catheters[11]. Several randomized controlled studies have demonstrated that catheter drainage offers a higher success rate (up to 100%) compared to needle aspiration, particularly when abscesses are larger than 5 cm [78,87-89]. Due to its obvious advantage of having a large bore, it evacuates the necrotic tissue efficiently. It has an additional advantage of being indwelling, which makes it more effective in clearing those abscesses that liquefy over a period of time.

Percutaneous drainage in the management of complications

Although aspirations have been useful in the management of refractory abscesses for several decades, free rupture with peritonitis was typically considered an indication for surgery. The reported mortality rate in surgically treated patients was as high as 50% [90,91]. In the last three decades, a paradigm shift has been seen from surgical drainage to catheter drainage. All complications related to ALA are currently managed with percutaneous catheter drainage [11,19-21,92-94]. By using catheter drainage, we have achieved a success rate of 97%, without significant mortality [11]. Only the placement of multiple catheters, usually in multiple sessions, is required to drain intraperitoneal fluid collections. As the collections are sterile, the peritonitis is not as severe as that seen in cases of bowel perforation. Not only is catheter drainage curative for the intraperitoneal rupture, it also effectively treats pleuropulmonary ruptures [11]. The drainage of pleural fluid collections may require CT guidance as ultrasound has low sensitivity for pleuropulmonary pathology. Lung abscesses usually do not require drainage due to the presence of bronchial fistula, which provides natural drainage in most patients. Catheter drainage has also been proved to be excellent in the management of biliary communications. Agarwal *et al* [22] evaluated 33 patients with refractory abscesses, nine of the patients were found to have an abscess with intrabiliary communication, and all patients were successfully treated with prolonged catheter drainage (12 to 50 d). None of the patients required endoscopic placement of stents. Endoscopic stenting or sphincterotomy, however, may be required to control bile leak prior to catheter removal when fistulous communication persists despite prolonged catheter drainage. Catheter drainage has also been shown to facilitate spontaneous healing of small arterial aneurysms resulting from ALA [83].

Surgical management

The role of surgical drainage in the management of ALA has been reassessed due to the widespread use of radiologically guided drainage [95]. However, open drainage may be warranted in some cases where percutaneous drainage may fail to evacuate abscess content. Surgery may also be indicated in selected cases of intraperitoneal rupture with generalized peritonitis [96]. As an alternative to open surgical drainage, laparoscopic drainage can result in less morbidity and mortality [97].

CONCLUSION

Clinical and imaging features of ALA are variable and parallel to each other. Although the mild form of the disease is cured easily with antibiotics alone, the other two forms of the disease—acute aggressive and chronic indolent—often require percutaneous drainage. Most complications and mortality in ALA occur when it presents in its acute aggressive form. Imaging studies play a key role in identifying the different forms of the disease and assessing the complications. All complications, including free intraperitoneal ruptures, can be managed with percutaneous catheter drainage.

FOOTNOTES

Author contributions: Priyadarshi RN contributed to the concept and design of the manuscript, data collection and manuscript writing; Kumar R and Anand U contributed to the literature search, critical inputs and manuscript revision.

Conflict-of-interest statement: All the authors declare that they have no conflict of interest related to this article.

Open-Access: This article is an open-access article that was selected by an in-house editor and fully peer-reviewed by external reviewers. It is distributed in accordance with the Creative Commons Attribution NonCommercial (CC BY-NC 4.0) license, which permits others to distribute, remix, adapt, build upon this work non-commercially, and license their derivative works on different terms, provided the original work is properly cited and the use is non-commercial. See: <https://creativecommons.org/licenses/by-nc/4.0/>

Country/Territory of origin: India

ORCID number: Rajeev Nayan Priyadarshi 0000-0003-2890-8910; Ramesh Kumar 0000-0001-5136-4865; Utpal Anand 0000-0003-0653-4129.

S-Editor: Liu JH

L-Editor: Webster JR

P-Editor: Liu JH

REFERENCES

- Walsh JA. Problems in recognition and diagnosis of amebiasis: estimation of the global magnitude of morbidity and mortality. *Rev Infect Dis* 1986; **8**: 228-238 [PMID: 2871619 DOI: 10.1093/clinids/8.2.228]
- Singh A, Banerjee T, Kumar R, Shukla SK. Prevalence of cases of amebic liver abscess in a tertiary care centre in India: A study on risk factors, associated microflora and strain variation of *Entamoeba histolytica*. *PLoS One* 2019; **14**: e0214880 [PMID: 30943253 DOI: 10.1371/journal.pone.0214880]
- Khan R, Hamid S, Abid S, Jafri W, Abbas Z, Islam M, Shah H, Beg S. Predictive factors for early aspiration in liver abscess. *World J Gastroenterol* 2008; **14**: 2089-2093 [PMID: 18395912 DOI: 10.3748/wjg.14.2089]
- Ghosh S, Sharma S, Gadpayle AK, Gupta HK, Mahajan RK, Sahoo R, Kumar N. Clinical, laboratory, and management profile in patients of liver abscess from northern India. *J Trop Med* 2014; **2014**: 142382 [PMID: 25002869 DOI: 10.1155/2014/142382]
- Khanna S, Chaudhary D, Kumar A, Vij JC. Experience with aspiration in cases of amebic liver abscess in an endemic area. *Eur J Clin Microbiol Infect Dis* 2005; **24**: 428-430 [PMID: 15928909 DOI: 10.1007/s10096-005-1338-2]
- Jindal A, Pandey A, Sharma MK, Mukund A, Vijayaraghavan R, Arora V, Shasthry SM, Choudhary A, Sarin SK. Management Practices and Predictors of Outcome of Liver Abscess in Adults: A Series of 1630 Patients from a Liver Unit. *J Clin Exp Hepatol* 2021; **11**: 312-320 [PMID: 33994714 DOI: 10.1016/j.jceh.2020.10.002]
- Stanley SL Jr. Amoebiasis. *Lancet* 2003; **361**: 1025-1034 [PMID: 12660071 DOI: 10.1016/S0140-6736(03)12830-9]
- Ralls PW, Barnes PF, Johnson MB, De Cock KM, Radin DR, Halls J. Medical treatment of hepatic amebic abscess: rare need for percutaneous drainage. *Radiology* 1987; **165**: 805-807 [PMID: 3317505 DOI: 10.1148/radiology.165.3.3317505]
- Nigam P, Gupta AK, Kapoor KK, Sharan GR, Goyal BM, Joshi LD. Cholestasis in amoebic liver abscess. *Gut* 1985; **26**: 140-145 [PMID: 3967831 DOI: 10.1136/gut.26.2.140]
- Priyadarshi RN, Sherin L, Kumar R, Anand U, Kumar P. CT of amebic liver abscess: different morphological types with different clinical features. *Abdom Radiol (NY)* 2021; **46**: 4148-4158 [PMID: 33893854 DOI: 10.1007/s00261-021-03093-w]
- Priyadarshi RN, Prakash V, Anand U, Kumar P, Jha AK, Kumar R. Ultrasound-guided percutaneous catheter drainage of various types of ruptured amebic liver abscess: a report of 117 cases from a highly endemic zone of India. *Abdom Radiol (NY)* 2019; **44**: 877-885 [PMID: 30361869 DOI: 10.1007/s00261-018-1810-y]
- Datta DV, Saha S, Singh SA, Aikat BK, Chhuttani PN. The clinical pattern and prognosis of patients with amebic liver abscess and jaundice. *Am J Dig Dis* 1973; **18**: 887-898 [PMID: 4355077 DOI: 10.1007/BF01073340]
- Jha AK, Jha P, Chaudhary M, Purkayastha S, Jha SK, Ranjan R, Priyadarshi RN, Kumar R. Evaluation of factors associated with complications in amoebic liver abscess in a predominantly toddy-drinking population: A retrospective study of 198 cases. *JGH Open* 2019; **3**: 474-479 [PMID: 31832547 DOI: 10.1002/jgh3.12183]
- Sharma N, Sharma A, Varma S, Lal A, Singh V. Amoebic liver abscess in the medical emergency of a North Indian hospital. *BMC Res Notes* 2010; **3**: 21 [PMID: 20181006 DOI: 10.1186/1756-0500-3-21]
- Katzenstein D, Rickerson V, Braude A. New concepts of amebic liver abscess derived from hepatic imaging, serodiagnosis, and hepatic enzymes in 67 consecutive cases in San Diego. *Medicine (Baltimore)* 1982; **61**: 237-246 [PMID: 6806561 DOI: 10.1097/00005792-198207000-00003]
- Chuah SK, Chang-Chien CS, Sheen IS, Lin HH, Chiou SS, Chiu CT, Kuo CH, Chen JJ, Chiu KW. The prognostic factors of severe amebic liver abscess: a retrospective study of 125 cases. *Am J Trop Med Hyg* 1992; **46**: 398-402 [PMID: 1575285 DOI: 10.4269/ajtmh.1992.46.398]
- Balasegaram M. Management of hepatic abscess. *Curr Probl Surg* 1981; **18**: 282-340 [PMID: 6263552]
- Singh JP, Kashyap A. A comparative evaluation of percutaneous catheter drainage for resistant amebic liver abscesses. *Am*

- J Surg* 1989; **158**: 58-62 [PMID: 2662790 DOI: 10.1016/0002-9610(89)90316-4]
- 19 **Hanna RM**, Dahniya MH, Badr SS, El-Betagy A. Percutaneous catheter drainage in drug-resistant amoebic liver abscess. *Trop Med Int Health* 2000; **5**: 578-581 [PMID: 10995100 DOI: 10.1046/j.1365-3156.2000.00586.x]
 - 20 **Ken JG**, vanSonnenberg E, Casola G, Christensen R, Polansky AM. Perforated amoebic liver abscesses: successful percutaneous treatment. *Radiology* 1989; **170**: 195-197 [PMID: 2909097 DOI: 10.1148/radiology.170.1.2909097]
 - 21 **Baijal SS**, Agarwal DK, Roy S, Choudhuri G. Complex ruptured amoebic liver abscesses: the role of percutaneous catheter drainage. *Eur J Radiol* 1995; **20**: 65-67 [PMID: 7556258 DOI: 10.1016/0720-048x(95)00613-u]
 - 22 **Agarwal DK**, Baijal SS, Roy S, Mittal BR, Gupta R, Choudhuri G. Percutaneous catheter drainage of amoebic liver abscesses with and without intrahepatic biliary communication: a comparative study. *Eur J Radiol* 1995; **20**: 61-64 [PMID: 7556257 DOI: 10.1016/0720-048x(95)00603-n]
 - 23 **Hughes MA**, Petri WA Jr. Amebic liver abscess. *Infect Dis Clin North Am* 2000; **14**: 565-582, viii [PMID: 10987110 DOI: 10.1016/s0891-5520(05)70121-5]
 - 24 **Kumanan T**, Sujaniha V, Sreeharan N. Amoebic liver abscess: a neglected tropical disease. *Lancet Infect Dis* 2020; **20**: 160-162 [PMID: 32006496 DOI: 10.1016/S1473-3099(19)30696-6]
 - 25 **Kannathasan S**, Murugananthan A, Kumanan T, de Silva NR, Rajeshkannan N, Haque R, Iddawela D. Epidemiology and factors associated with amoebic liver abscess in northern Sri Lanka. *BMC Public Health* 2018; **18**: 118 [PMID: 29316900 DOI: 10.1186/s12889-018-5036-2]
 - 26 Ray G. Sociodemographic and Clinical Profile of Amoebic Liver Abscess observed at a Tertiary Referral Hospital over 10 Years. *Trop Gastroenterol* 2021; **42**: 126-33
 - 27 **Nath J**, Ghosh SK, Singha B, Paul J. Molecular Epidemiology of Amoebiasis: A Cross-Sectional Study among North East Indian Population. *PLoS Negl Trop Dis* 2015; **9**: e0004225 [PMID: 26633890 DOI: 10.1371/journal.pntd.0004225]
 - 28 **Wuerz T**, Kane JB, Boggild AK, Krajden S, Keystone JS, Fuksa M, Kain KC, Warren R, Kempston J, Anderson J. A review of amoebic liver abscess for clinicians in a nonendemic setting. *Can J Gastroenterol* 2012; **26**: 729-733 [PMID: 23061067 DOI: 10.1155/2012/852835]
 - 29 **Kumar R**, Priyadarshi RN, Anand U. Toddy consumption and amoebic liver abscess in India: An unexplored link. *Indian J Public Health* 2019; **63**: 89-90 [PMID: 30880745 DOI: 10.4103/ijph.IJPH_192_18]
 - 30 **Mukhopadhyay M**, Saha AK, Sarkar A, Mukherjee S. Amoebic liver abscess: presentation and complications. *Indian J Surg* 2010; **72**: 37-41 [PMID: 23133202 DOI: 10.1007/s12262-010-0007-6]
 - 31 **Haque R**, Huston CD, Hughes M, Houpt E, Petri WA Jr. Amebiasis. *N Engl J Med* 2003; **348**: 1565-1573 [PMID: 12700377 DOI: 10.1056/NEJMra022710]
 - 32 **Sharma MP**, Dasarathy S, Verma N, Saksena S, Shukla DK. Prognostic markers in amoebic liver abscess: a prospective study. *Am J Gastroenterol* 1996; **91**: 2584-2588 [PMID: 8946991]
 - 33 **Singh R**, Adhikari DR, Patil BP, Talathi NR, Hanamshetti SR, Joshi RM. Amoebic liver abscess: an appraisal. *Int Surg* 2011; **96**: 305-309 [PMID: 22808611 DOI: 10.9738/cc9.1]
 - 34 **Khim G**, Em S, Mo S, Townell N. Liver abscess: diagnostic and management issues found in the low resource setting. *Br Med Bull* 2019; **132**: 45-52 [PMID: 31836890 DOI: 10.1093/bmb/ldz032]
 - 35 **Brandt H**, Tamayo RP. Pathology of human amoebiasis. *Hum Pathol* 1970; **1**: 351-385 [PMID: 4330002 DOI: 10.1016/s0046-8177(70)80072-7]
 - 36 **Martínez-Palomo A**. The pathogenesis of amoebiasis. *Parasitol Today* 1987; **3**: 111-118 [PMID: 15462926 DOI: 10.1016/0169-4758(87)90048-2]
 - 37 **Tsutsumi V**, Mena-Lopez R, Anaya-Velazquez F, Martínez-Palomo A. Cellular bases of experimental amoebic liver abscess formation. *Am J Pathol* 1984; **117**: 81-91 [PMID: 6385728]
 - 38 **Simjee AE**, Patel A, Gathiram V, Engelbrecht HE, Singh K, Rooknoodeen F. Serial ultrasound in amoebic liver abscess. *Clin Radiol* 1985; **36**: 61-68 [PMID: 3905191 DOI: 10.1016/s0009-9260(85)80027-1]
 - 39 **Missalek W**. Ultrasonography in the diagnosis of amoebic liver abscess and its complications. *Trop Doct* 1992; **22**: 59-64 [PMID: 1318595 DOI: 10.1177/004947559202200205]
 - 40 **Jimenez F**. Pathology of amoebiasis. *Bull N Y Acad Med* 1981; **57**: 217-223 [PMID: 6938282]
 - 41 **Knight R**. Hepatic amoebiasis. *Semin Liver Dis* 1984; **4**: 277-292 [PMID: 6098014 DOI: 10.1055/s-2008-1040657]
 - 42 **Aikat BK**, Bhusnurmath SR, Pal AK, Chhuttani PN, Datta DV. The pathology and pathogenesis of fatal hepatic amoebiasis--A study based on 79 autopsy cases. *Trans R Soc Trop Med Hyg* 1979; **73**: 188-192 [PMID: 473308 DOI: 10.1016/0035-9203(79)90209-8]
 - 43 **Elizondo G**, Weissleder R, Stark DD, Todd LE, Compton C, Wittenberg J, Ferrucci JT Jr. Amebic liver abscess: diagnosis and treatment evaluation with MR imaging. *Radiology* 1987; **165**: 795-800 [PMID: 2891154 DOI: 10.1148/radiology.165.3.2891154]
 - 44 **Basile JA**, Klein SR, Worthen NJ, Wilson SE, Hiatt JR. Amebic liver abscess. The surgeon's role in management. *Am J Surg* 1983; **146**: 67-71 [PMID: 6869681 DOI: 10.1016/0002-9610(83)90261-1]
 - 45 **Radín DR**, Ralls PW, Colletti PM, Halls JM. CT of amoebic liver abscess. *AJR Am J Roentgenol* 1988; **150**: 1297-1301 [PMID: 3259367 DOI: 10.2214/ajr.150.6.1297]
 - 46 **Nari GA**, Ceballos Espinosa R, Carrera Ladrón de Guevara S, Preciado Vargas J, Cruz Valenciano JL, Briones Rivas JL, Moreno Hernández F, Góngora Ortega J. [Amebic liver abscess. Three years experience]. *Rev Esp Enferm Dig* 2008; **100**: 268-272 [PMID: 18662078 DOI: 10.4321/s1130-01082008000500004]
 - 47 **Boultee JE**, Simjee AE, Rooknoodeen F, Engelbrecht HE. Experiences with grey scale ultrasonography in hepatic amoebiasis. *Clin Radiol* 1979; **30**: 683-689 [PMID: 509870 DOI: 10.1016/s0009-9260(79)80020-3]
 - 48 **Sharma MP**, Ahuja V. Amoebic liver abscess. *J Indian Acad Clin Med* 2003; **4**: 107-11
 - 49 **Adams EB**, MacLeod IN. Invasive amoebiasis. II. Amebic liver abscess and its complications. *Medicine (Baltimore)* 1977; **56**: 325-334 [PMID: 875719 DOI: 10.1097/00005792-197707000-00004]
 - 50 **Wells CD**, Arguedas M. Amebic liver abscess. *South Med J* 2004; **97**: 673-682 [PMID: 15301125 DOI: 10.1097/00007611-200407000-00013]

- 51 **Anesi JA**, Gluckman S. Amebic liver abscess. *Clin Liver Dis (Hoboken)* 2015; **6**: 41-43 [PMID: 31040985 DOI: 10.1002/cld.488]
- 52 **Alam F**, Salam MA, Hassan P, Mahmood I, Kabir M, Haque R. Amebic liver abscess in northern region of Bangladesh: sociodemographic determinants and clinical outcomes. *BMC Res Notes* 2014; **7**: 625 [PMID: 25204395 DOI: 10.1186/1756-0500-7-625]
- 53 **Wallace RJ Jr**, Greenberg SB, Lau JM, Kalchoff WP, Mangold DE, Martin R. Amebic peritonitis following rupture of an amebic liver abscess. Successful treatment of two patients. *Arch Surg* 1978; **113**: 322-325 [PMID: 205190 DOI: 10.1001/archsurg.1978.01370150094024]
- 54 **Ajao OG**, Adebo OA. Unruptured amoebic liver abscess presenting as acute abdomen. *Trop Doct* 1983; **13**: 109-111 [PMID: 6879689 DOI: 10.1177/004947558301300305]
- 55 **Ibrarullah M**, Agarwal DK, Bajjal SS, Mittal BR, Kapoor VK. Amebic liver abscess with intra-biliary rupture. *HPB Surg* 1994; **7**: 305-10; discussion 310 [PMID: 8204550 DOI: 10.1155/1994/36160]
- 56 **Peters RS**, Gitlin N, Libke RD. Amebic liver abscess. *Annu Rev Med* 1981; **32**: 161-174 [PMID: 7013659 DOI: 10.1146/annurev.me.32.020181.001113]
- 57 **Reed SL**. Amebiasis: an update. *Clin Infect Dis* 1992; **14**: 385-393 [PMID: 1554822 DOI: 10.1093/clinids/14.2.385]
- 58 **Barnes PF**, De Cock KM, Reynolds TN, Ralls PW. A comparison of amebic and pyogenic abscess of the liver. *Medicine (Baltimore)* 1987; **66**: 472-483 [PMID: 3316923 DOI: 10.1097/00005792-198711000-00005]
- 59 **Neill L**, Edwards F, Collin SM, Harrington D, Wakerley D, Rao GG, McGregor AC. Clinical characteristics and treatment outcomes in a cohort of patients with pyogenic and amoebic liver abscess. *BMC Infect Dis* 2019; **19**: 490 [PMID: 31159769 DOI: 10.1186/s12879-019-4127-8]
- 60 **Greaney GC**, Reynolds TB, Donovan AJ. Ruptured amebic liver abscess. *Arch Surg* 1985; **120**: 555-561 [PMID: 3885916 DOI: 10.1001/archsurg.1985.01390290037006]
- 61 **Recipon G**, Piver É, Caille A, Le Pape P, Pihet M, Pagès JC, Chandener J, Desoubeaux G. Is procalcitonin increased in cases of invasive amoebiasis? *Diagn Microbiol Infect Dis* 2015; **83**: 395-399 [PMID: 26388549 DOI: 10.1016/j.diagmicrobio.2015.08.014]
- 62 **Ralls PW**, Henley DS, Colletti PM, Benson R, Raval JK, Radin DR, Boswell WD Jr, Halls JM. Amebic liver abscess: MR imaging. *Radiology* 1987; **165**: 801-804 [PMID: 3317504 DOI: 10.1148/radiology.165.3.3317504]
- 63 **Elzi L**, Laifer G, Sendi P, Ledermann HP, Fluckiger U, Bassetti S. Low sensitivity of ultrasonography for the early diagnosis of amebic liver abscess. *Am J Med* 2004; **117**: 519-522 [PMID: 15464710 DOI: 10.1016/j.amjmed.2004.01.031]
- 64 **Seeto RK**, Rockey DC. Amebic liver abscess: epidemiology, clinical features, and outcome. *West J Med* 1999; **170**: 104-109 [PMID: 10063397]
- 65 **Léonetti P**, Moncany G, Soubeyrand J. [Amebic abscess of the liver. Contribution of ultrasonics to developmental diagnosis apropos of 983 cases]. *J Radiol* 1987; **68**: 259-264 [PMID: 3295224]
- 66 **N'Gbesso RD**, Kéita AK. [Ultrasonography of amebic liver abscesses. Proposal of a new classification]. *J Radiol* 1997; **78**: 569-576 [PMID: 9537173]
- 67 **Terrier F**, Becker CD, Triller JK. Morphologic aspects of hepatic abscesses at computed tomography and ultrasound. *Acta Radiol Diagn (Stockh)* 1983; **24**: 129-137 [PMID: 6624514]
- 68 **Priyadarshi RN**, Kumar P, Kumar R, Anand U, Shyama. Venous thrombosis and segmental hypoperfusion in amebic liver abscess: MDCT demonstration and its implications. *Abdom Radiol (NY)* 2020; **45**: 652-660 [PMID: 31955219 DOI: 10.1007/s00261-020-02409-6]
- 69 **Qian LJ**, Zhu J, Zhuang ZG, Xia Q, Liu Q, Xu JR. Spectrum of multilocular cystic hepatic lesions: CT and MR imaging findings with pathologic correlation. *Radiographics* 2013; **33**: 1419-1433 [PMID: 24025933 DOI: 10.1148/rg.335125063]
- 70 **Mathieu D**, Vasile N, Fagniez PL, Segui S, Grably D, Lardé D. Dynamic CT features of hepatic abscesses. *Radiology* 1985; **154**: 749-752 [PMID: 3969480 DOI: 10.1148/radiology.154.3.3969480]
- 71 **Ralls PW**, Quinn MF, Boswell WD Jr, Colletti PM, Radin DR, Halls J. Patterns of resolution in successfully treated hepatic amebic abscess: sonographic evaluation. *Radiology* 1983; **149**: 541-543 [PMID: 6622702 DOI: 10.1148/radiology.149.2.6622702]
- 72 **Berry M**, Bazaz R, Bhargava S. Amebic liver abscess: sonographic diagnosis and management. *J Clin Ultrasound* 1986; **14**: 239-242 [PMID: 3084579 DOI: 10.1002/jcu.1870140402]
- 73 **Sarda AK**, Bal S, Sharma AK, Kapur MM. Intra-peritoneal rupture of amoebic liver abscess. *Br J Surg* 1989; **76**: 202-203 [PMID: 2702459 DOI: 10.1002/bjs.1800760231]
- 74 **Pawar SV**, Zanwar VG, Gambhire PA, Mohite AR, Choksey AS, Rathi PM, Asgaonkar DS. Unusual complication of amebic liver abscess: Hepatogastric fistula. *World J Gastrointest Endosc* 2015; **7**: 916-919 [PMID: 26240693 DOI: 10.4253/wjge.v7.i9.916]
- 75 **Mowji PJ**, Cohen AJ, Potkin B, Viltuznik J. Amebic liver abscess with hepatoduodenal fistula. *Am J Gastroenterol* 1987; **82**: 558-559 [PMID: 3578237]
- 76 **Ibarra-Pérez C**. Thoracic complications of amebic abscess of the liver: report of 501 cases. *Chest* 1981; **79**: 672-677 [PMID: 7226956 DOI: 10.1378/chest.79.6.672]
- 77 **Sandeep SM**, Banait VS, Thakur SK, Bapat MR, Rathi PM, Abraham P. Endoscopic biliary drainage in patients with amebic liver abscess and biliary communication. *Indian J Gastroenterol* 2006; **25**: 125-127 [PMID: 16877823]
- 78 **Singh S**, Chaudhary P, Saxena N, Khandelwal S, Poddar DD, Biswal UC. Treatment of liver abscess: prospective randomized comparison of catheter drainage and needle aspiration. *Ann Gastroenterol* 2013; **26**: 332-339 [PMID: 24714320]
- 79 **Ochsner A**, DeBakey M. Liver abscess part I. *Am J Surg* 1935; **29**: 173-194 [DOI: 10.1016/s0002-9610(35)91120-5]
- 80 **Chemaly RF**, Hall GS, Keys TF, Procop GW. Microbiology of liver abscesses and the predictive value of abscess gram stain and associated blood cultures. *Diagn Microbiol Infect Dis* 2003; **46**: 245-248 [PMID: 12944014 DOI: 10.1016/s0732-8893(03)00088-9]
- 81 **Méchai F**, Aoun O, Ficko C, Barruet R, Imbert P, Rapp C. Budd-Chiari syndrome as a vascular complication of amebic liver abscess. *Am J Trop Med Hyg* 2009; **81**: 768-769 [PMID: 19861608 DOI: 10.4269/ajtmh.2009.09-0230]

- 82 **Yadav T**, Patel RK, Bansal A, Chatterjee N, Patidar Y, Mukund A. Caudate lobe amebic abscesses: percutaneous image-guided aspiration or drainage. *Abdom Radiol (NY)* 2022; **47**: 1157-1166 [PMID: 34964910 DOI: 10.1007/s00261-021-03395-z]
- 83 **Priyadarshi RN**, Kumar R, Anand U. Case Report: Spontaneous Resolution of Intracavitary Hepatic Artery Pseudoaneurysm Caused by Amebic Liver Abscess following Percutaneous Drainage. *Am J Trop Med Hyg* 2019; **101**: 157-159 [PMID: 31162010 DOI: 10.4269/ajtmh.19-0103]
- 84 **Sachdev GK**, Dhol P. Colonic involvement in patients with amebic liver abscess: endoscopic findings. *Gastrointest Endosc* 1997; **46**: 37-39 [PMID: 9260703 DOI: 10.1016/s0016-5107(97)70207-4]
- 85 **Premkumar M**, Devurgowda D, Dudha S, Kulkarni A, Joshi YK. Clinical and Endoscopic Management of Synchronous Amoebic Liver Abscess and Bleeding Colonic Ulcers. *J Assoc Physicians India* 2019; **67**: 14-18 [PMID: 31304698]
- 86 **de la Rey Nel J**, Simjee AE, Patel A. Indications for aspiration of amoebic liver abscess. *S Afr Med J* 1989; **75**: 373-376 [PMID: 2711266]
- 87 **Rajak CL**, Gupta S, Jain S, Chawla Y, Gulati M, Suri S. Percutaneous treatment of liver abscesses: needle aspiration versus catheter drainage. *AJR Am J Roentgenol* 1998; **170**: 1035-1039 [PMID: 9530055 DOI: 10.2214/ajr.170.4.9530055]
- 88 **Cai YL**, Xiong XZ, Lu J, Cheng Y, Yang C, Lin YX, Zhang J, Cheng NS. Percutaneous needle aspiration versus catheter drainage in the management of liver abscess: a systematic review and meta-analysis. *HPB (Oxford)* 2015; **17**: 195-201 [PMID: 25209740 DOI: 10.1111/hpb.12332]
- 89 **Ramani A**, Ramani R, Kumar MS, Lakhkar BN, Kundaje GN. Ultrasound-guided needle aspiration of amoebic liver abscess. *Postgrad Med J* 1993; **69**: 381-383 [PMID: 8346134 DOI: 10.1136/pgmj.69.811.381]
- 90 **Kumar R**, Anand U, Priyadarshi RN, Mohan S, Parasar K. Management of amoebic peritonitis due to ruptured amoebic liver abscess: It's time for a paradigm shift. *JGH Open* 2019; **3**: 268-269 [PMID: 31276048 DOI: 10.1002/jgh3.12144]
- 91 **Eggleston FC**, Handa AK, Verghese M. Amebic peritonitis secondary to amebic liver abscess. *Surgery* 1982; **91**: 46-48 [PMID: 7054906]
- 92 **Saraswat VA**, Agarwal DK, Baijal SS, Roy S, Choudhuri G, Dhiman RK, Bhandari L, Naik SR. Percutaneous catheter drainage of amoebic liver abscess. *Clin Radiol* 1992; **45**: 187-189 [PMID: 1555372 DOI: 10.1016/s0009-9260(05)80639-7]
- 93 **vanSonnenberg E**, Ferrucci JT Jr, Mueller PR, Wittenberg J, Simeone JF. Percutaneous drainage of abscesses and fluid collections: technique, results, and applications. *Radiology* 1982; **142**: 1-10 [PMID: 7053517 DOI: 10.1148/radiology.142.1.7053517]
- 94 **vanSonnenberg E**, Mueller PR, Schiffman HR, Ferrucci JT Jr, Casola G, Simeone JF, Cabrera OA, Gosink BB. Intrahepatic amebic abscesses: indications for and results of percutaneous catheter drainage. *Radiology* 1985; **156**: 631-635 [PMID: 4023220 DOI: 10.1148/radiology.156.3.4023220]
- 95 **Gibney EJ**. Amoebic liver abscess. *Br J Surg* 1990; **77**: 843-844 [PMID: 2203504 DOI: 10.1002/bjs.1800770803]
- 96 **Akgun Y**, Tacyildiz IH, Celik Y. Amebic liver abscess: changing trends over 20 years. *World J Surg* 1999; **23**: 102-106 [PMID: 9841772 DOI: 10.1007/s002689900573]
- 97 **Tay KH**, Ravinathan T, Hoe MN, See AC, Chng HC. Laparoscopic drainage of liver abscesses. *Br J Surg* 1998; **85**: 330-332 [PMID: 9529485 DOI: 10.1046/j.1365-2168.1998.00617.x]

Progress in interventional radiology treatment of pulmonary embolism: A brief review

Alessandro Posa, Pierluigi Barbieri, Giulia Mazza, Alessandro Tanzilli, Roberto Iezzi, Riccardo Manfredi, Cesare Colosimo

Specialty type: Radiology, nuclear medicine and medical imaging

Provenance and peer review: Invited article; Externally peer reviewed.

Peer-review model: Single blind

Peer-review report's scientific quality classification

Grade A (Excellent): A
Grade B (Very good): 0
Grade C (Good): C
Grade D (Fair): 0
Grade E (Poor): 0

P-Reviewer: Lv XL, China;
Schoenhagen P, United States

Received: March 20, 2022

Peer-review started: March 20, 2022

First decision: May 31, 2022

Revised: June 14, 2022

Accepted: August 6, 2022

Article in press: August 6, 2022

Published online: August 28, 2022



Alessandro Posa, Pierluigi Barbieri, Giulia Mazza, Alessandro Tanzilli, Roberto Iezzi, Riccardo Manfredi, Cesare Colosimo, Department of Diagnostic Imaging, Oncologic Radiotherapy and Hematology, Fondazione Policlinico Universitario A. Gemelli IRCCS, Rome 00168, Italy

Corresponding author: Alessandro Posa, MD, Doctor, Department of Diagnostic Imaging, Oncologic Radiotherapy and Hematology, Fondazione Policlinico Universitario A. Gemelli IRCCS, L.go A. Gemelli 8, Rome 00168, Italy. alessandro.posa@gmail.com

Abstract

Pulmonary embolism represents a common life-threatening condition. Prompt identification and treatment of this pathological condition are mandatory. In cases of massive pulmonary embolism and hemodynamic instability or right heart failure, interventional radiology treatment for pulmonary embolism is emerging as an alternative to medical treatment (systemic thrombolysis) and surgical treatment. Interventional radiology techniques include percutaneous endovascular catheter directed therapies as selective thrombolysis and thrombus aspiration, which can prove useful in cases of failure or infeasibility of medical and surgical approaches.

Key Words: Pulmonary embolism; Interventional radiology; Thrombolysis; Thrombectomy; Catheter directed therapy; Endovascular

©The Author(s) 2022. Published by Baishideng Publishing Group Inc. All rights reserved.

Core Tip: Endovascular treatment of massive pulmonary embolism can be a life-saving intervention in hemodynamically unstable patients.

Citation: Posa A, Barbieri P, Mazza G, Tanzilli A, Iezzi R, Manfredi R, Colosimo C. Progress in interventional radiology treatment of pulmonary embolism: A brief review. *World J Radiol* 2022; 14(8): 286-292

URL: <https://www.wjgnet.com/1949-8470/full/v14/i8/286.htm>

DOI: <https://dx.doi.org/10.4329/wjr.v14.i8.286>

INTRODUCTION

Venous thromboembolism, clinically presenting as deep vein thrombosis or pulmonary embolism (PE), is the third most frequent acute cardiovascular syndrome globally, after myocardial infarction and stroke[1]. Approximately one-third of all patients with a new diagnosis of venous thromboembolism have PE, with or without deep vein thrombosis[2]. PE can be defined as the occlusion of the pulmonary arteries or its branches with embolic material (thrombus, air, fat or amniotic fluid) that originates elsewhere in the body. Most commonly, the cause is a thrombus arising from the deep veins of the lower extremities, which travels to the pulmonary circulation.

Diagnosis of PE can be subtle, as there are no specific symptoms, and clinical presentation varies widely, ranging from asymptomatic to sudden cardiac death, which is seen in 25%-30% of patients[3]. There have been many advances in the field of PE in the recent decades. The development of new diagnostic and therapeutic strategies, including medical and surgical treatment as well as endovascular therapy, has led to an increasing complexity of patient treatment and, consequently, to the need of optimizing the management of this serious condition.

PHYSIOPATHOLOGY

PE, by definition, is characterized by the presence of emboli in the pulmonary arterial circulation. Most emboli originate as thrombi in the deep veins of the lower extremities; the most common site of thrombosis is represented by the calf veins, followed by femoro-popliteal veins and iliac veins. Less frequently, emboli arise from upper extremity veins and are typically associated with central venous catheters, intracardiac devices, malignancy or venous trauma. A smaller percentage of PE is caused by pelvic deep vein thrombosis, but they are generally associated with a predisposing factor such as pelvic infection, pelvic surgery or pregnancy[4]. When 25%-30% of the pulmonary vasculature is obliterated by a thrombo-embolus, pulmonary artery pressure begins to increase. However, the mechanical obstruction is not the only element leading to pulmonary hypertension: the disruption of the alveolar-capillary membrane by the thrombi results in a decrease of oxygen diffusion, with subsequent hypoxia and release of vasoconstrictors that contribute to the acute development of pulmonary hypertension[5]. The increase of pressure in the pulmonary artery determines heterogeneity of pulmonary perfusion, leading to the simultaneous presence of hypo- and hyperperfused areas; there will be an imbalance between ventilation and perfusion, generating hypoxemia[6].

Moreover, PE can have significant cardiac and hemodynamic consequences, related to the size of emboli and the presence or absence of underlying cardiopulmonary disease. In healthy patients, the mean pulmonary artery pressure can be up to 40 mmHg acutely; right ventricle (RV) failure ensues when 50%-75% of pulmonary arteries are obstructed[7]. When the degree of pulmonary artery obstruction exceeds 50%-75%, the right heart dilates and the combination of the increased wall stress and cardiac ischemia impair RV function and left ventricular (LV) output, leading to hypotension[8]. The presence of pre-existing cardiopulmonary disease results in diminished pulmonary vascular reserve and hemodynamic compromise at a lower level of pulmonary arterial obstruction.

PULMONARY EMBOLISM RISK STRATIFICATION

The American Heart Association (AHA) and the European Society of Cardiology (ESC) classified PE according to its severity, identifying three main categories[1,9].

Patients with massive (AHA) or high risk (ESC) PE present with hypotension, defined as a systolic blood pressure lower than 90 mmHg, or a drop of > 40 mmHg for at least 15 min or need for vasopressor support.

Submassive (AHA) or intermediate risk (ESC) classifications slightly differ as, according to AHA, patients with submassive PE present with an RV strain with no hypotension. RV strain is defined as: RV dysfunction on echocardiography or computed tomography pulmonary angiography, and RV injury identified by an increase in cardiac biomarkers as troponins or brain natriuretic hormone. On the other side, the ESC criteria for intermediate-risk PE include patients with a simplified Pulmonary Embolism Severity Index score ≥ 1 , regardless of RV strain. The Pulmonary Embolism Severity Index score is based on the patient's age, comorbidities, heart rate, blood pressure and oxygen saturation. Moreover, the ESC subclassifies intermediate-risk patients in two groups based on RV dysfunction and RV injury (intermediate risk-high) or only one or neither of these findings (intermediate risk-low).

Low risk patients, according to both AHA and ESC, do not meet criteria for the abovementioned risk categories.

MEDICAL AND SURGICAL TREATMENT

Severe PE leads to hypoxaemia due to the ventilation-perfusion mismatch. Therefore, it is advised to use oxygen in patients with oxygen saturation < 90%. High-flow oxygen and mechanical ventilation should be taken in consideration when extreme hemodynamic instability is present (*i.e.* cardiac arrest), even though obtaining a good hypoxemia correction is not completely possible without PE reperfusion techniques[10,11]. Intubation should be considered in patients who are not manageable with noninvasive ventilation[1].

Acute RV failure is a cause of death in high-risk PE patients due to the reduction of cardiac output. When low central venous pressure is present, modest fluid challenge (< 500 mL) could be an option, increasing cardiac index in these patients[12]. On the other hand, fluid challenge could also over-distend the RV, leading to a reduction of cardiac output. Therefore, it is recommended to use it wisely[13]. If signs of elevated central venous pressure are present, no volume loading is advised. Vasopressors are often necessary in association with reperfusion treatment (medical, surgical or interventional). Norepinephrine leads to an improvement in coronary perfusion and ventricular systolic interaction, without changing pulmonary vascular resistance[14]; the use of norepinephrine should be limited in patients with cardiogenic shock.

Temporary extracorporeal membrane oxygenation could be used in patients with a high-risk PE, cardiac arrest and circulatory collapse, but its use needs to be further tested with clinical trials[15,16].

Acute PE may lead to cardiac arrest, in which case the current advanced life support guidelines have to be followed[17].

Moreover, in patients with intermediate to high risk of PE, it is advised to start subcutaneous anticoagulation while waiting for diagnostic tests, usually with low-molecular weight heparin, fondaparinux or unfractionated heparin[18]. Clinical trials with non-vitamin K antagonist oral anticoagulants are ongoing.

Vitamin K antagonists are vastly used for oral anticoagulation in recent years; when vitamin K antagonists are used, low-molecular weight heparin or unfractionated heparin should be continued along with oral anticoagulants for more than 5 d until the International Normalized Ratio value reaches 2-3 for 2 d[19].

Regarding reperfusion treatment, systemic thrombolysis leads to fast improvement of the pulmonary obstruction and cardiovascular parameters in patients with PE compared to medical treatment alone[20, 21]. The best results are obtained when reperfusion treatment starts 48 h after symptoms onset; however thrombolysis could be useful even after 6-14 d[22]. Intravenous administration of recombinant tissue-type plasminogen activator is preferred to first generation thrombolytic agents (*i.e.* urokinase)[23].

Surgical embolectomy in patients with acute PE is performed through cardiopulmonary bypass, with incision of the pulmonary arteries and clots removal. This approach is advised in high-risk PE and in selected intermediate-risk patients[1,24].

ENDOVASCULAR TREATMENTS: CURRENT EVIDENCE AND FUTURE PERSPECTIVES

Catheter directed thrombolysis

Catheter directed thrombolysis (CDT) gives the advantage of locally delivering a high concentration of fibrinolytic agent to a great clot surface. This way, fibrinolytic dose can be greatly reduced compared to the systemic one, and side effects are therefore lower. A routine use diagnostic angiography catheter with multiple holes can be used to deliver the fibrinolytic agent and increase its local blood concentration. This could enhance the efficiency of fibrinolysis, reducing the risk of bleeding. Each pulmonary artery is catheterized with a multihole catheter, and a fibrinolytic agent such as tissue plasminogen activator is injected through the clot at a rate of 1 mg/h for 24 h in case of a unilateral PE (single device) and 1 mg/h for 12 h if bilateral PE (double device) (SEATTLE II Trial)[25]. A more recent trial, the OPTALYSE PE trial, analyzed the possibility to further lower the dose of tissue plasminogen activator with shorter infusions. The total dose was significantly lower, ranging from 4 to 12 mg per lung, and shorter infusion times (2 to 6 h)[26].

Efficient systemic administration of heparin is continued throughout the endovascular fibrinolysis procedure. Despite the lack of randomized trial studies comparing endovascular and systemic thrombolytic therapy, several comparative studies have been carried out. In a meta-analysis of Bloomer *et al*[27], the rate of intracranial hemorrhage with CDT was 0.35%, which is significantly lower than that reported with systemic thrombolytics in other randomized trials (1.46%). Bloomer *et al*[27] also found that the rate of major bleeding or vascular complication was 4.65%, and the observed mortality rate was 3.4% (12.9% in the massive PE group, 0.74% in the submassive PE group).

In addition, results of an American national registry enrolling 3107 patients who underwent systemic fibrinolytic treatment and 1319 patients undergoing CDT showed that the systemic thrombolysis group had increased rates of bleeding-related mortality (18.1% *vs* 8.4%), general mortality (14.9% *vs* 6.12%) and rehospitalization (10.6% *vs* 7.6%)[28]. According to these data, the risk of fatal bleeding is lower during CDT than in cases of systemic thrombolysis. This can be due to the higher (approximately four-fold)

Table 1 Main mechanical thrombectomy devices

Rheolytic	Rotational	Aspiration +/- retriever	Fragmentation	Ultrasound
Angiojet (Boston Scientific)	Aspirex (Straub Medical)	Indigo CAT8 (Penumbra Inc.); Flowtriever (Inari)	Fogarty arterial balloon embolectomy catheter (Edwards); Pig-Tail Catheters	Ekos endovascular system (Boston Scientific)

dose of fibrinolytic agent used in systemic thrombolysis. However, as these data are extracted from a national registry and not from randomized studies, they should cautiously be taken in consideration. The ongoing PE-TRACT and HI-PEITHO studies are designed to overcome this issue.

Mechanical thrombectomy

In cases of massive PE, the first aim should be to quickly declot the affected pulmonary artery to decrease pulmonary hypertension and the risk of RV failure. Initial fragmentation or thrombectomy by different devices (Table 1) can help reduce the thrombotic load and improve reperfusion. In addition, fragmentation of the clot exposes a greater surface of the thrombus, increasing the efficacy of local or systemic therapies[29].

Current catheters for mechanical thrombectomy or endovascular aspiration are classified based on the mechanism of action.

Rheolytic: AngioJet (Boston Scientific, Massachusetts, United States) working mechanism is determined by aspiration of the thrombus using the Venturi-Bernoulli effect. It creates a suction effect with high-pressure jets in the catheter's distal holes. Various complications (e.g., bradycardia and heart attack, severe hemoptysis, kidney failure as well as intra- and periprocedural deaths) were reported during the use of this device[30]; hence, the use of AngioJet as a first-approach treatment should be avoided. Currently the main indication of this product remains treatment of peripheral venous districts.

Rotational: A relatively new device for treatment of PE is Aspirex (Straub, Wangs, Switzerland). Launched in mid-2010, the Aspirex catheter acts as an Archimedean screw that rotates inside the catheter lumen; this spiral mechanism provides an aspiration supplied by an active motor. Clinical results are promising; however, only recent studies with small cohorts of patients demonstrated its safety and efficacy, and there is a lack of randomized studies supporting this evidence[31]. Two European case series have been reported, with complete thrombus clearance observed in 83% to 88% of patients with intermediate- and high-risk PE[31,32].

Aspiration: The Indigo mechanical aspiration system (Penumbra, Alameda, United States) is an aspiration thrombectomy catheter system. A large caliber (8 French) catheter with a directional soft tip, allows easy aspiration of the clots in the pulmonary arteries due to the great suction power of a suction pump. Several studies are being performed to evaluate safety and efficacy of this device. The recent Indigo Aspiration System for Treatment of Pulmonary Embolism Trial (EXTRACT-PE), a prospective multicenter study on 119 patients demonstrated a significant reduction in the RV/LV ratio and a low major adverse event rate in submassive PE patients treated with the Indigo CAT8 aspiration system, with a reduction of administered intraprocedural thrombolytic drugs, which were avoided in 98.3% of patients[33]. The Indigo CAT8 received Food and Drug Administration approval for PE treatment in December 2019. The system is being monitored to assess its safety even in real-world clinical practice, showing a low incidence of reports linked to the product[34].

FlowTrieve® System (Inari Medical) is another aspiration device. Its mechanism features three self-expanding nitinol mesh disks designed to engage, disrupt and deliver the clot to the Trierer Aspiration Catheter for extraction. It has been evaluated in a recent single-arm multicenter trial involving 106 patients (FLARE Study) and appears safe and effective in patients with acute intermediate-risk PE, with significant improvement in RV/LV ratio and minimal major bleeding[35]. In 2021 Inari Medical, Inc. announced enrollment of the PEERLESS randomized controlled trial comparing the clinical outcomes of patients with intermediate-high risk PE treated with the company's FlowTrieve system vs CDT (NCT05111613). PEERLESS is a prospective, multicenter trial that will include up to 700 patients and 60 centers in the United States and Europe. It will be the first ever randomized controlled trial to compare mechanical thrombectomy to catheter-directed thrombolysis for the treatment of PE and aims to provide definitive data on interventional treatment options for these patients.

Fragmentation: The EKOSonic system (Boston Scientific, Massachusetts, United States) is an ultrasound-assisted catheter-directed thrombolysis system, which was specifically indicated for treatment of PE. The ultrasound waves that depart from the interior of the 5.4 French catheter can reach and treat the whole thrombus; in addition, fibrinolytic agent infusion can be performed from the catheter, combining the two treatment modalities. The functioning tip of the catheter can be of different lengths, with a range from 6 to 50 cm. Although it has been associated with a relatively safe and effective profile, the clinical benefits of this treatment when compared to classical CDT has yet to be proven[25]. Ultrasound-assisted thrombolysis was shown in a randomized trial named ULTIMA to determine faster decreases of the

RV/LV ratio in patients with acute onset of intermediate-risk PE when compared to medical treatment, with no occurrence of major bleeding. However, the authors did not observe variations in 90-d patient mortality[36].

CONCLUSION

Actual ESC guidelines indicate that in high-risk or intermediate/high-risk patients (with RV dysfunction at transthoracic ultrasonography or at computed tomography pulmonary angiography or Pulmonary Embolism Severity Index greater than 1 and positive troponin test), reperfusion treatments should be performed, in association with prompt hemodynamic support[1]. However, systemic thrombolysis is actually considered as the first indication, and as literature evidence states surgical pulmonary embolectomy is recommended in patients with high-risk PE in whom systemic thrombolysis is contraindicated or has failed (level of evidence I). Percutaneous catheter-directed treatment has level of evidence IIa and therefore should be conditionally considered after failure or infeasibility of the abovementioned medical and surgical therapies[2].

Set up of a multidisciplinary team and of management protocols for high-risk and intermediate/high-risk patients with PE should be considered, to promptly and correctly address every PE case.

New perspectives

The 2021 announcement of the multicentric prospective PEERLESS randomized controlled trial comparing aspiration thrombectomy *vs* catheter-directed thrombolysis in up to 700 patients will provide real-life data on interventional radiology treatments for patients with intermediate/high-risk PE. At the same time, ultrasonography-assisted thrombolysis is proving valuable in intermediate/high-risk PE patients with good results and low complication rates[36]. However, more prospective studies are needed to shed light on the best interventional radiology treatment for this critical condition as well as to give the right place in the guidelines to these endovascular and mini-invasive techniques, on par to medical and surgical treatments.

FOOTNOTES

Author contributions: Posa A designed the research study; Posa A, Barbieri P, Tanzilli A and Mazza G performed the research and wrote the manuscript; Posa A, Iezzi R, Manfredi R and Colosimo C revised the manuscript; All authors have read and approved the final manuscript.

Conflict-of-interest statement: All the Authors have no conflict of interest to disclose.

Open-Access: This article is an open-access article that was selected by an in-house editor and fully peer-reviewed by external reviewers. It is distributed in accordance with the Creative Commons Attribution NonCommercial (CC BY-NC 4.0) license, which permits others to distribute, remix, adapt, build upon this work non-commercially, and license their derivative works on different terms, provided the original work is properly cited and the use is non-commercial. See: <https://creativecommons.org/licenses/by-nc/4.0/>

Country/Territory of origin: Italy

ORCID number: Alessandro Posa 0000-0001-9617-3413; Roberto Iezzi 0000-0002-2791-481X; Riccardo Manfredi 0000-0002-4972-9500.

S-Editor: Liu JH

L-Editor: Filipodia

P-Editor: Liu JH

REFERENCES

- 1 **Konstantinides SV**, Meyer G, Becattini C, Bueno H, Geersing GJ, Harjola VP, Huisman MV, Humbert M, Jennings CS, Jiménez D, Kucher N, Lang IM, Lankeit M, Lorusso R, Mazzolai L, Meneveau N, Ni Áinle F, Prandoni P, Pruszczyk P, Righini M, Torbicki A, Van Belle E, Zamorano JL; ESC Scientific Document Group. 2019 ESC Guidelines for the diagnosis and management of acute pulmonary embolism developed in collaboration with the European Respiratory Society (ERS). *Eur Heart J* 2020; **41**: 543-603 [PMID: 31504429 DOI: 10.1093/eurheartj/ehz405]
- 2 **Ortel TL**, Neumann I, Ageno W, Beyth R, Clark NP, Cuker A, Hutten BA, Jaff MR, Manja V, Schulman S, Thurston C, Vedantham S, Verhamme P, Witt DM, D Florez I, Izcovich A, Nieuwlaat R, Ross S, J Schünemann H, Wiercioch W, Zhang Y. American Society of Hematology 2020 guidelines for management of venous thromboembolism: treatment of

- deep vein thrombosis and pulmonary embolism. *Blood Adv* 2020; **4**: 4693-4738 [PMID: 33007077 DOI: 10.1182/bloodadvances.2020001830]
- 3 **Morrone D**, Morrone V. Acute Pulmonary Embolism: Focus on the Clinical Picture. *Korean Circ J* 2018; **48**: 365-381 [PMID: 29737640 DOI: 10.4070/kcj.2017.0314]
 - 4 **Turetz M**, Sideris AT, Friedman OA, Tripathi N, Horowitz JM. Epidemiology, Pathophysiology, and Natural History of Pulmonary Embolism. *Semin Intervent Radiol* 2018; **35**: 92-98 [PMID: 29872243 DOI: 10.1055/s-0038-1642036]
 - 5 **Stratmann G**, Gregory GA. Neurogenic and humoral vasoconstriction in acute pulmonary thromboembolism. *Anesth Analg* 2003; **97**: 341-354 [PMID: 12873915 DOI: 10.1213/01.ANE.0000068983.18131.F0]
 - 6 **Fernandes CJ**, Luppino Assad AP, Alves-Jr JL, Jardim C, de Souza R. Pulmonary Embolism and Gas Exchange. *Respiration* 2019; **98**: 253-262 [PMID: 31390642 DOI: 10.1159/000501342]
 - 7 **Matthews JC**, McLaughlin V. Acute right ventricular failure in the setting of acute pulmonary embolism or chronic pulmonary hypertension: a detailed review of the pathophysiology, diagnosis, and management. *Curr Cardiol Rev* 2008; **4**: 49-59 [PMID: 19924277 DOI: 10.2174/157340308783565384]
 - 8 **Wood KE**. Major pulmonary embolism: review of a pathophysiologic approach to the golden hour of hemodynamically significant pulmonary embolism. *Chest* 2002; **121**: 877-905 [PMID: 11888976 DOI: 10.1378/chest.121.3.877]
 - 9 **Giri J**, Sista AK, Weinberg I, Kearon C, Kumbhani DJ, Desai ND, Piazza G, Gladwin MT, Chatterjee S, Kobayashi T, Kabrhel C, Barnes GD. Interventional Therapies for Acute Pulmonary Embolism: Current Status and Principles for the Development of Novel Evidence: A Scientific Statement From the American Heart Association. *Circulation* 2019; **140**: e774-e801 [PMID: 31585051 DOI: 10.1161/CIR.0000000000000707]
 - 10 **Messika J**, Goutorbe P, Hajage D, Ricard JD. Severe pulmonary embolism managed with high-flow nasal cannula oxygen therapy. *Eur J Emerg Med* 2017; **24**: 230-232 [PMID: 28452810 DOI: 10.1097/MEJ.0000000000000420]
 - 11 **Lacroix G**, Pons F, D'Aranda E, Legodec J, Romanat PE, Goutorbe P. High-flow oxygen, a therapeutic bridge while awaiting thrombolysis in pulmonary embolism? *Am J Emerg Med* 2013; **31**: 463.e1-463.e2 [PMID: 23159426 DOI: 10.1016/j.ajem.2012.08.030]
 - 12 **Mercat A**, Diehl JL, Meyer G, Teboul JL, Sors H. Hemodynamic effects of fluid loading in acute massive pulmonary embolism. *Crit Care Med* 1999; **27**: 540-544 [PMID: 10199533 DOI: 10.1097/00003246-199903000-00032]
 - 13 **Green EM**, Givertz MM. Management of acute right ventricular failure in the intensive care unit. *Curr Heart Fail Rep* 2012; **9**: 228-235 [PMID: 22805893 DOI: 10.1007/s11897-012-0104-x]
 - 14 **Ghignone M**, Girling L, Prewitt RM. Volume expansion vs norepinephrine in treatment of a low cardiac output complicating an acute increase in right ventricular afterload in dogs. *Anesthesiology* 1984; **60**: 132-135 [PMID: 6198941 DOI: 10.1097/00000542-198402000-00009]
 - 15 **Corsi F**, Lebreton G, Bréchet N, Hekimian G, Nieszkowska A, Trouillet JL, Luyt CE, Leprince P, Chastre J, Combes A, Schmidt M. Life-threatening massive pulmonary embolism rescued by venoarterial-extracorporeal membrane oxygenation. *Crit Care* 2017; **21**: 76 [PMID: 28347320 DOI: 10.1186/s13054-017-1655-8]
 - 16 **Meneveau N**, Guillon B, Planquette B, Piton G, Kimmoun A, Gaide-Chevronnay L, Aissaoui N, Neuschwander A, Zogheib E, Dupont H, Pili-Floury S, Ecartot F, Schiele F, Deye N, de Prost N, Favory R, Girard P, Cristinar M, Ferré A, Meyer G, Capellier G, Sanchez O. Outcomes after extracorporeal membrane oxygenation for the treatment of high-risk pulmonary embolism: a multicentre series of 52 cases. *Eur Heart J* 2018; **39**: 4196-4204 [PMID: 30137303 DOI: 10.1093/eurheartj/ehy464]
 - 17 **Perkins GD**, Olasveengen TM, Maconochie I, Soar J, Wyllie J, Greif R, Lockey A, Semeraro F, Van de Voorde P, Lott C, Monsieurs KG, Nolan JP, European Resuscitation Council. European Resuscitation Council Guidelines for Resuscitation: 2017 update. *Resuscitation* 2018; **123**: 43-50 [PMID: 29233740 DOI: 10.1016/j.resuscitation.2017.12.007]
 - 18 **Soar J**, Nolan JP, Böttiger BW, Perkins GD, Lott C, Carli P, Pellis T, Sandroni C, Skrifvars MB, Smith GB, Sunde K, Deakin CD; Adult advanced life support section Collaborators. European Resuscitation Council Guidelines for Resuscitation 2015: Section 3. Adult advanced life support. *Resuscitation* 2015; **95**: 100-147 [PMID: 26477701 DOI: 10.1016/j.resuscitation.2015.07.016]
 - 19 **Witt DM**, Clark NP, Kaatz S, Schnurr T, Ansell JE. Guidance for the practical management of warfarin therapy in the treatment of venous thromboembolism. *J Thromb Thrombolysis* 2016; **41**: 187-205 [PMID: 26780746 DOI: 10.1007/s11239-015-1319-y]
 - 20 **Goldhaber SZ**, Haire WD, Feldstein ML, Miller M, Toltzis R, Smith JL, Taveira da Silva AM, Come PC, Lee RT, Parker JA. Alteplase vs heparin in acute pulmonary embolism: randomised trial assessing right-ventricular function and pulmonary perfusion. *Lancet* 1993; **341**: 507-511 [PMID: 8094768 DOI: 10.1016/0140-6736(93)90274-k]
 - 21 **Kline JA**, Nordenholz KE, Courtney DM, Kabrhel C, Jones AE, Rondina MT, Diercks DB, Klinger JR, Hernandez J. Treatment of submassive pulmonary embolism with tenecteplase or placebo: cardiopulmonary outcomes at 3 mo: multicenter double-blind, placebo-controlled randomized trial. *J Thromb Haemost* 2014; **12**: 459-468 [PMID: 24484241 DOI: 10.1111/jth.12521]
 - 22 **Daniels LB**, Parker JA, Patel SR, Grodstein F, Goldhaber SZ. Relation of duration of symptoms with response to thrombolytic therapy in pulmonary embolism. *Am J Cardiol* 1997; **80**: 184-188 [PMID: 9230156 DOI: 10.1016/s0002-9149(97)00315-9]
 - 23 **Sharifi M**, Bay C, Skrocki L, Rahimi F, Mehdipour M; "MOPETT" Investigators. Moderate pulmonary embolism treated with thrombolysis (from the "MOPETT" Trial). *Am J Cardiol* 2013; **111**: 273-277 [PMID: 23102885 DOI: 10.1016/j.amjcard.2012.09.027]
 - 24 **Lee T**, Itagaki S, Chiang YP, Egorova NN, Adams DH, Chikwe J. Survival and recurrence after acute pulmonary embolism treated with pulmonary embolectomy or thrombolysis in New York State, 1999 to 2013. *J Thorac Cardiovasc Surg* 2018; **155**: 1084-1090.e12 [PMID: 28942971 DOI: 10.1016/j.jtcvs.2017.07.074]
 - 25 **Piazza G**, Hohlfelder B, Jaff MR, Ouriel K, Engelhardt TC, Sterling KM, Jones NJ, Gurley JC, Bhatheja R, Kennedy RJ, Goswami N, Natarajan K, Rundback J, Sadiq IR, Liu SK, Bhalla N, Raja ML, Weinstock BS, Cynamon J, Elmasri FF, Garcia MJ, Kumar M, Ayerdi J, Soukas P, Kuo W, Liu PY, Goldhaber SZ; SEATTLE II Investigators. A Prospective, Single-Arm, Multicenter Trial of Ultrasound-Facilitated, Catheter-Directed, Low-Dose Fibrinolysis for Acute Massive and

- Submassive Pulmonary Embolism: The SEATTLE II Study. *JACC Cardiovasc Interv* 2015; **8**: 1382-1392 [PMID: 26315743 DOI: 10.1016/j.jcin.2015.04.020]
- 26 **Tapson VF**, Sterling K, Jones N, Elder M, Tripathy U, Brower J, Maholic RL, Ross CB, Natarajan K, Fong P, Greenspon L, Tamaddon H, Piracha AR, Engelhardt T, Katopodis J, Marques V, Sharp ASP, Piazza G, Goldhaber SZ. A Randomized Trial of the Optimum Duration of Acoustic Pulse Thrombolysis Procedure in Acute Intermediate-Risk Pulmonary Embolism: The OPTALYSE PE Trial. *JACC Cardiovasc Interv* 2018; **11**: 1401-1410 [PMID: 30025734 DOI: 10.1016/j.jcin.2018.04.008]
 - 27 **Bloomer TL**, El-Hayek GE, McDaniel MC, Sandvall BC, Liberman HA, Devireddy CM, Kumar G, Fong PP, Jaber WA. Safety of catheter-directed thrombolysis for massive and submassive pulmonary embolism: Results of a multicenter registry and meta-analysis. *Catheter Cardiovasc Interv* 2017; **89**: 754-760 [PMID: 28145042 DOI: 10.1002/ccd.26900]
 - 28 **Arora S**, Panaich SS, Ainani N, Kumar V, Patel NJ, Tripathi B, Shah P, Patel N, Lahewala S, Deshmukh A, Badheka A, Grines C. Comparison of In-Hospital Outcomes and Readmission Rates in Acute Pulmonary Embolism Between Systemic and Catheter-Directed Thrombolysis (from the National Readmission Database). *Am J Cardiol* 2017; **120**: 1653-1661 [PMID: 28882336 DOI: 10.1016/j.amjcard.2017.07.066]
 - 29 **Patel N**, Patel NJ, Agnihotri K, Panaich SS, Thakkar B, Patel A, Savani C, Patel N, Arora S, Deshmukh A, Bhatt P, Alfonso C, Cohen M, Tafur A, Elder M, Mohamed T, Attaran R, Schreiber T, Grines C, Badheka AO. Utilization of catheter-directed thrombolysis in pulmonary embolism and outcome difference between systemic thrombolysis and catheter-directed thrombolysis. *Catheter Cardiovasc Interv* 2015; **86**: 1219-1227 [PMID: 26308961 DOI: 10.1002/ccd.26108]
 - 30 **Kuo WT**, Gould MK, Louie JD, Rosenberg JK, Sze DY, Hofmann LV. Catheter-directed therapy for the treatment of massive pulmonary embolism: systematic review and meta-analysis of modern techniques. *J Vasc Interv Radiol* 2009; **20**: 1431-1440 [PMID: 19875060 DOI: 10.1016/j.jvir.2009.08.002]
 - 31 **Dumantepe M**, Teymen B, Akturk U, Seren M. Efficacy of rotational thrombectomy on the mortality of patients with massive and submassive pulmonary embolism. *J Card Surg* 2015; **30**: 324-332 [PMID: 25683156 DOI: 10.1111/jocs.12521]
 - 32 **Bayiz H**, Dumantepe M, Teymen B, Uyar I. Percutaneous aspiration thrombectomy in treatment of massive pulmonary embolism. *Heart Lung Circ* 2015; **24**: 46-54 [PMID: 25060976 DOI: 10.1016/j.hlc.2014.06.014]
 - 33 **Sista AK**, Horowitz JM, Tapson VF, Rosenberg M, Elder MD, Schiro BJ, Dohad S, Amoroso NE, Dexter DJ, Loh CT, Leung DA, Bieneman BK, Perkowski PE, Chuang ML, Benenati JF; EXTRACT-PE Investigators. Indigo Aspiration System for Treatment of Pulmonary Embolism: Results of the EXTRACT-PE Trial. *JACC Cardiovasc Interv* 2021; **14**: 319-329 [PMID: 33454291 DOI: 10.1016/j.jcin.2020.09.053]
 - 34 **Sedhom R**, Abdelmaseeh P, Haroun M, Megaly M, Narayanan MA, Syed M, Ambrosia AM, Kalra S, George JC, Jaber WA. Complications of Penumbra Indigo Aspiration Device in Pulmonary Embolism: Insights From MAUDE Database. *Cardiovasc Revasc Med* 2022; **39**: 97-100 [PMID: 34706845 DOI: 10.1016/j.carrev.2021.10.009]
 - 35 **Tu T**, Toma C, Tapson VF, Adams C, Jaber WA, Silver M, Khandhar S, Amin R, Weinberg M, Engelhardt T, Hunter M, Holmes D, Hoots G, Hamdalla H, Maholic RL, Lilly SM, Ouriel K, Rosenfield K; FLARE Investigators. A Prospective, Single-Arm, Multicenter Trial of Catheter-Directed Mechanical Thrombectomy for Intermediate-Risk Acute Pulmonary Embolism: The FLARE Study. *JACC Cardiovasc Interv* 2019; **12**: 859-869 [PMID: 31072507 DOI: 10.1016/j.jcin.2018.12.022]
 - 36 **Kucher N**, Boekstegers P, Müller OJ, Kupatt C, Beyer-Westendorf J, Heitzer T, Tebbe U, Horstkotte J, Müller R, Blessing E, Greif M, Lange P, Hoffmann RT, Werth S, Barmeyer A, Härtel D, Grünwald H, Empen K, Baumgartner I. Randomized, controlled trial of ultrasound-assisted catheter-directed thrombolysis for acute intermediate-risk pulmonary embolism. *Circulation* 2014; **129**: 479-486 [PMID: 24226805 DOI: 10.1161/CIRCULATIONAHA.113.005544]

Retrospective Study

Imaging volumes during COVID-19: A Victorian health service experience

Jo-Anne Pinson, My Linh Diep, Vinay Krishnan, Caroline Aird, Cassie Cooper, Christopher Leong, Jeff Chen, Nicholas Ardley, Eldho Paul, Mohamed Khaldoun Badawy

Specialty type: Radiology, nuclear medicine and medical imaging

Provenance and peer review:

Unsolicited article; Externally peer reviewed.

Peer-review model: Single blind

Peer-review report's scientific quality classification

Grade A (Excellent): A
Grade B (Very good): 0
Grade C (Good): C
Grade D (Fair): 0
Grade E (Poor): 0

P-Reviewer: Chen Q, China; Verde F, Italy

Received: March 16, 2022

Peer-review started: March 16, 2022

First decision: June 16, 2022

Revised: July 7, 2022

Accepted: July 20, 2022

Article in press: July 20, 2022

Published online: August 28, 2022



Jo-Anne Pinson, My Linh Diep, Vinay Krishnan, Caroline Aird, Cassie Cooper, Christopher Leong, Jeff Chen, Nicholas Ardley, Mohamed Khaldoun Badawy, Monash Health Imaging, Monash Health, Clayton, Victoria 3168, Australia

Jo-Anne Pinson, Department of Medical Imaging, Peninsula Health, Melbourne, Victoria 3099, Australia

Jo-Anne Pinson, Mohamed Khaldoun Badawy, Department of Medical Imaging and Radiation Sciences, School of Allied Health Care, Faculty of Medicine, Nursing and Health Sciences, Monash University, Clayton, Victoria 3800, Australia

Eldho Paul, Department of Epidemiology and Preventive Medicine, School of Public Health and Preventive Medicine, Monash University, Melbourne, Victoria 3800, Australia

Corresponding author: Mohamed Khaldoun Badawy, BSc, MSc, PhD, Senior Lecturer, Senior Scientist, Monash Health Imaging, Monash Health, 246 Clayton Road, Clayton, Victoria 3168, Australia. mohamed.badawy@monashhealth.org

Abstract**BACKGROUND**

The World Health Organisation declared the coronavirus disease 2019 (COVID-19) a pandemic on March 11, 2020. While globally, the relative caseload has been high, Australia's has been relatively low. During the pandemic, radiology services have seen significant changes in workflow across modalities and a reduction in imaging volumes.

AIM

To investigate differences in modality imaging volumes during the COVID-19 pandemic across a large Victorian public health network.

METHODS

A retrospective analysis from January 2019 to December 2020 compared imaging volumes across two periods corresponding to the pandemic's first and second waves. Weekly volumes across patient class, modality and mobile imaging were summed for periods: wave 1 (weeks 11 to 16 for 2019; weeks 63 to 68 for 2020) and wave 2 (weeks 28 to 43 for 2019; weeks 80 to 95 for 2020). Microsoft Power Business Intelligence linked to the radiology information system was used to mine

all completed examinations.

RESULTS

Summed weekly data during the pandemic's first wave showed the greatest decrease of 29.8% in adult outpatient imaging volumes and 46.3% in paediatric emergency department imaging volumes. Adult nuclear medicine demonstrated the greatest decrease of 37.1% for the same period. Paediatric nuclear medicine showed the greatest decrease of 47.8%, with angiography increasing by 50%. The pandemic's second wave demonstrated the greatest decrease of 23.5% in adult outpatient imaging volumes, with an increase of 18.2% in inpatient imaging volumes. The greatest decrease was 28.5% in paediatric emergency department imaging volumes. Nuclear medicine showed the greatest decrease of 37.1% for the same period. Paediatric nuclear medicine showed the greatest decrease of 36.7%. Mobile imaging utilisation increased between 57.8% and 135.1% during the first and second waves. A strong correlation was observed between mobile and non-mobile imaging in the emergency setting (Spearman's correlation coefficient = -0.743, $P = 0.000$). No correlation was observed in the inpatient setting (Spearman's correlation coefficient = -0.059, $P = 0.554$).

CONCLUSION

Nuclear medicine was most impacted, while computed tomography and angiography were the least affected by the pandemic. The impact was less during the pandemic's second wave. Mobile imaging shows continuous growth during both waves.

Key Words: COVID-19; Pandemic; Radiology; Imaging volume; Modality; Mobile imaging

©The Author(s) 2022. Published by Baishideng Publishing Group Inc. All rights reserved.

Core Tip: Analysis of weekly imaging modality volumes provides an overview of changes in service demand over time. We describe the changes in imaging modality and mobile imaging volumes during Victoria's first and second waves of the coronavirus disease 2019 pandemic.

Citation: Pinson JA, Diep ML, Krishnan V, Aird C, Cooper C, Leong C, Chen J, Ardley N, Paul E, Badawy MK. Imaging volumes during COVID-19: A Victorian health service experience. *World J Radiol* 2022; 14(8): 293-310

URL: <https://www.wjgnet.com/1949-8470/full/v14/i8/293.htm>

DOI: <https://dx.doi.org/10.4329/wjr.v14.i8.293>

INTRODUCTION

The World Health Organisation declared the coronavirus disease 2019 (COVID-19) a pandemic on March 11, 2020[1]. Healthcare facilities implemented strict infection control, social distancing protocols, and other measures in the interest of public health and safety[2]. In preparation for the surge in hospitalisations across the globe, overall elective surgical services decreased by approximately 72%[3]. In comparison, in Australia, this fell by about 69%. Others utilised computational modelling to help predict the health services saturation point for ICU beds and ventilators[4]. While globally, the relative caseload has been high, Australia's has been relatively low. In this context, during 2020, Victoria has experienced most of Australia's cases, with the new daily caseloads shown in [Figure 1](#).

Due to the overwhelming prevalence of COVID-19 in various countries, for example, Italy, some radiology departments were dedicated to imaging COVID-19 patients only[5]. Radiology services have also seen significant changes in workflow across modalities and a reduction in imaging volumes[6-8]. For example, departments were re-configured to separate COVID-19 patients from non-infected patients, segregation of staff to reduce infection transmission, increased demand for PPE, radiologists reporting from home, and expansion of video conferencing use[5,9]. For patients presenting to the emergency department, general radiography was primarily used due to its accessibility, availability and low radiation levels. The chest X-ray was an ideal first choice for patients with typical symptoms of COVID-19, such as shortness of breath on exertion, persistent cough and chest pain [8]. To minimise the transmission risk of suspected COVID-19 (sCOVID) patients in hospital, mobile imaging became particularly important to manage workflow[10,11]. Imaging in the ward wearing PPE could reduce staff exposure, with effective cleaning of mobile units possible between imaging patients, without compromising patient care.

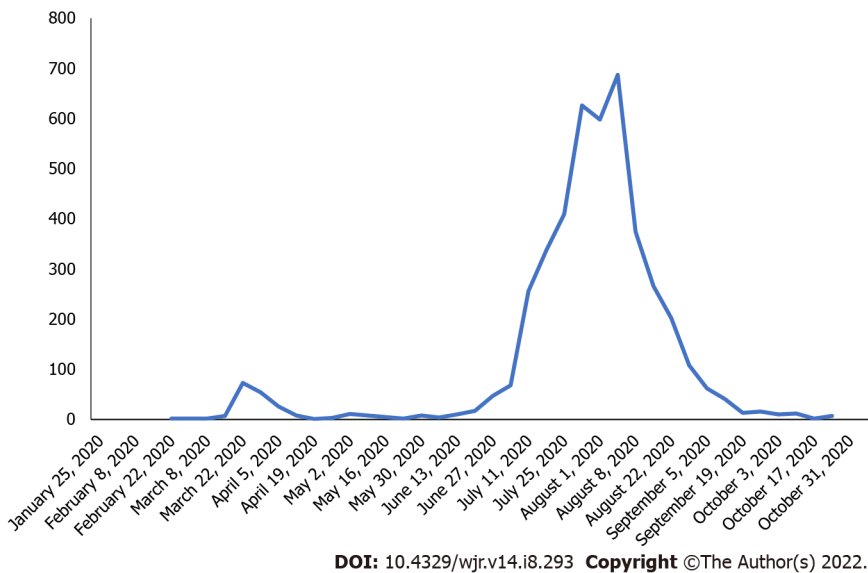


Figure 1 Victorian new the coronavirus disease 2019 case numbers by date from January 2020–November 2020.

While it has been reported, there was a decrease in patients presenting with stroke to our institution during the pandemic[7]. To our knowledge, little is known about the severity of impact on radiology volumes in Australia. While overall Australian imaging volumes were analysed through Medicare, no institutional experience has been presented[12].

Objectives

This study investigates the imaging volume changes during the pandemic across the network at a large Victorian public health service provider. A secondary aim was to study changes in mobile imaging utilisation and whether that impacted the use of fixed (non-mobile) X-ray imaging systems. This data will help inform radiology practices for service adaptation with subsequent pandemic phases or other “once in a lifetime” events.

MATERIALS AND METHODS

This health network has 98 imaging systems across eight imaging modalities analysed according to Table 1.

Study setting

Our network provided over three million episodes of care from 2019 to 2020. Three of our five hospitals provide accident and emergency services, and one is a geriatric centre, and the other is an oncology centre that did not service COVID-19-positive patients (‘clean site’). Data from the geriatric and oncology centre were excluded due to heterogeneity in these sites. Significant federal, state and local health policy and guideline changes were implemented and updated during the pandemic that impacted the imaging pathway, including: patients with typical respiratory symptoms (fever, chest tightness, dyspnoea, cough) were classified as sCOVID-19 (suspected COVID-19); recommendation for all eligible sCOVID-19 patients to have computed tomography (CT) pulmonary angiography (CTPA) instead of V/Q scans[13]; rescheduling of non-urgent cases as discussed with referring clinicians; use of mobile X-ray to reduce infection transmission; social distancing guidelines restricting patient waiting room numbers and minimum area of 4 m² per person in shared spaces.

Data collection

Microsoft Power Business Intelligence, linked to the radiology information system, was used to mine all completed examinations between January 1, 2019 and December 31, 2020 across three sites. Imaging modality was defined as the device or technology used in medical imaging (general X-ray, mammography, nuclear medicine, CT, magnetic resonance imaging (MRI), fluoroscopy, angiography, ultrasound, with mobile X-ray being a subset of X-ray). Fixed or non-mobile imaging was an X-ray system permanently secured in an X-ray room. Mobile imaging was defined as using a portable X-ray imaging system capable of moving to different locations. Patient classes were defined by location (inpatient (IP), outpatient (OP) or emergency department (ED)). Adult patients were ≥ 16 years, while paediatric patients were aged < 16 years. Examinations were filtered by modality and patient class.

Table 1 List of equipment number across all modalities

Modality	MRI	NM	BMD	CT	X-ray	Fluoro	US	Angio
Equip No.	5	6	2	7	26	4	45	3

MRI: Magnetic resonance imaging; NM: Nanometer; BMD: Bone mineral densitometry; CT: Computed tomography; Fluoro: Fluoroscopy; US: Ultrasound; Angio: Angiography.

March 2020 and April 2020 [week 63 (March 11 to March 17) to week 68 (April 15 to April 21)] corresponded to Victoria's first wave of the pandemic; July 2020 to October 2020 [week 80 (July 9 to July 14) to week 95 (October 21 to October 26)] corresponded to the second wave of the pandemic. **Figure 2** provides the timeline of the first and second waves for considering the impact on departmental caseloads. The outcome measure was total weekly completed imaging case numbers from Wednesday to Tuesday commencing Wednesday January 2 to Tuesday January 8, 2019 (week 1) for direct day matched weekly comparisons between 2019 and 2020, allowing for any periodic variability observed. Weekly modality data were summed to reflect the first and second waves of the pandemic.

Statistical analysis

Weekly volumes across patient class, modality and mobile imaging were summed for defined periods: wave 1 (weeks 11 to 16 for 2019; weeks 63 to 68 for 2020) and wave 2 (weeks 28 to 43 for 2019; weeks 80 to 95 for 2020). This was to evaluate the impact of COVID-19 on patient class, modality and mobile imaging case volumes during each COVID-19 wave. For analysis of mean weekly case numbers, pre-COVID data were defined as weeks 1 to 60 (*i.e.*, January 2, 2019 to February 29, 2020), while COVID-19 data were defined as the mean of weeks 61 to 104 (*i.e.*, March 1, 2020 to December 31, 2020). Independent sample *t*-tests were performed comparing the mean weekly imaging case volumes in the years 2020 and 2019 for each imaging modality type stratified by patient service locations for the pre-COVID-19 and post-COVID-19 periods with results presented as means and 95% confidence intervals (95%CI). The relationship between mobile and non-mobile imaging volumes was assessed using Spearman rank correlation. Statistical significance was considered for *p* values < 0.05. All analyses were performed using SAS version 9.4 (SAS Institute, Cary, NC, United States). Dr Eldho Paul reviewed the statistical methods of this study from Monash University.

This study was approved by the Monash Health Human Research Ethics Committee.

RESULTS

Adults

Total volume (all modalities): During the pandemic's first wave in Victoria, total adult imaging volume across all modalities declined by 20.7% between March 11 and April 21, 2020 (weeks 63 to 68) compared to the same time in 2019 (March 13 and April 23, 2019, weeks 11 to 16). During the pandemic's second wave, adult imaging volume across all modalities declined by 6.6% between July 8, and October 27, 2020 (weeks 80 to 95) compared to the same time in 2019 (July 10, and October 29, 2019, weeks 28 to 43).

Volume by patient class

Table 2 shows the summed weekly imaging volumes for the defined periods and the percentage of adult image volume change across all included modalities by patient class for weeks 11 to 16 (March 13 and April 23) and 28 to 43 (July 10 and October 29) in 2019 and weeks 63 to 68 (March 11 and April 21) and 80 to 95 (July 8 and 2October 27) in 2020.

Volume by modality: During the pandemic's first wave between March 11 and April 21, 2020 (weeks 63 to 68), adult angiography, bone mineral densitometry, computed tomography, fluoroscopy, general radiography, magnetic resonance imaging, mammography, nuclear medicine and ultrasound imaging volumes declined between 10.3% and 37.1% when compared to the same time in 2019 (March 13 and April 23, 2019, weeks 11 to 16) shown in **Table 3**.

During the pandemic's second wave between July 8 and October 27, 2020 (weeks 80 to 95), adult angiography, bone mineral densitometry, fluoroscopy, general radiography, magnetic resonance imaging, mammography, nuclear medicine and ultrasound services declined between 1.6% and 31.6%, while computed tomography increased by 1.7% when compared to the same time in 2019 (July 10 and October 29, 2019, weeks 28 to 43) shown in **Table 4**.

Figure 3 highlights the weekly adult modality imaging volumes.

Comparison of the adult mean weekly 2019 (pre-COVID-19, January 1, 2019 to February 29, 2020, weeks 1 to 61) with 2020 (March 1 to December 31, 2020 weeks 61 to 104) imaging volumes by modality, categorised by inpatient, outpatient and emergency services (**Table 5**) shows statistically significant

Table 2 Summed imaging volumes and percentage change in adult imaging volume across patient class in waves 1 and 2

Wave 1	2020 (weeks 63-68)	2019 (weeks 11-16)	% change	Wave 2	2020 (weeks 80-95)	2019 (weeks 28-43)	% change
ED	9521	12783	-25.5	ED	29454	32262	-8.7
IP	9210	9395	-2.0	IP	31424	26576	18.2
OP	8874	12636	-29.8	OP	26967	35236	-23.5
Overall	27605	34814	-20.7	Overall	87845	94074	-6.6

ED: Emergency department; IP: Inpatient; OP: Outpatient.

Table 3 Summed imaging volumes and percentage change in adult imaging volumes across modalities in wave 1

Wave 1	2020 (weeks 63-68)	2019 (weeks 11-16)	%
Angiography	269	300	-10.3
Bone Mineral Densitometry	185	239	-22.6
Computed Tomography	5883	6688	-12.0
Fluoroscopy	766	968	-20.9
General Radiography	11668	15311	-23.8
Magnetic Resonance Imaging	2013	2709	-25.7
Mammography	82	123	-33.3
Nuclear Medicine	394	626	-37.1
Ultrasound	6345	7850	-19.2
Total	27605	34814	-20.7

Table 4 Summed imaging volumes and percentage change in adult imaging volume across modalities in wave 2

Wave 2	2020 (weeks 80-95)	2019 (weeks 28-43)	%
Angiography	822	835	-1.6
Bone mineral densitometry	690	892	-22.6
Computed tomography	19316	18997	1.7
Fluoroscopy	2313	2550	-9.3
General radiography	36845	40592	-9.2
Magnetic resonance imaging	6685	7539	-11.3
Mammography	303	334	-9.3
Nuclear medicine	1149	1679	-31.6
Ultrasound	19722	20656	-4.5
Total	87845	94074	-6.6

declines in six imaging modalities ($P = 0.042$ to $P < 0.0001$). There were statistically significant declines in one inpatient imaging modality ($P = 0.002$) and nine outpatient imaging modalities ($P = 0.027$ to $P < 0.0001$). Statistically significant increases were observed in five inpatient modalities ($P = 0.0003$ to $P < 0.0001$). All patient classes observed overall declines across seven imaging modalities ($P = 0.027$ to $P < 0.0001$).

Mobile and non-mobile X-ray imaging: During the pandemic's first wave in Victoria, total adult mobile imaging volume increased by 57.8% between March 11 and April 21, 2020 (weeks 63 to 68) compared to the same time in 2019 (March 13 and April 23, 2019, weeks 11 to 16). During the pandemic's second wave, adult mobile imaging volume increased by 135.1% between July 8 and October 27, 2020 (weeks 80 to 95) compared to the same time in 2019 (July 10 and October 29, 2019, weeks 28 to 43). **Table 6** highlights the mobile imaging changes across inpatient and emergency patient classes during the first

Table 5 Comparison of mean adult weekly imaging volumes for 2019 and 2020 including 95% CIs, by imaging modality categorised by patient setting

Adult Setting	Modality	2020			2019			P value
		Mean	Min-max	95%CI	Mean	Min-max	95%CI	
Emergency	Angiography	4.05	1-10	3.38-4.71	5.03	2-12	4.51-5.56	0.02
	Computed tomography	541.2	384-663	520-562.4	548.68	473-606	541.7-555.7	0.453
	Fluoroscopy	5.18	1-12	4.31-6.05	4.15	0-11	3.58-4.72	0.042
	Radiography	1162.64	925-1309	1133.02-1192.25	1299.03	1156-1446	1281.05-1317.02	< 0.0001
	Magnetic resonance imaging	12.11	3-27	10.35-13.87	18.55	9-30	17.09-20.01	< 0.0001
	Nuclear Medicine	3.27	0-8	2.66-3.88	7.55	0-21	6.43-8.67	< 0.0001
	Ultrasound	122.98	85-157	117.52-128.43	172.13	116-255	163.72-180.55	< 0.0001
	Mammography	0	0-0	0-0	0.02	-0.02-0.05	0-0.1	0.394
Inpatient	Angiography	38.8	23-53	36.25-41.34	29.48	17-43	27.94-31.02	< 0.0001
	Computed tomography	408.05	277-498	392.38-423.71	298.87	210-416	285.57-312.16	< 0.0001
	Fluoroscopy	125.98	82-162	120.33-131.63	129.25	80-155	125.39-133.11	0.325
	Radiography	855.64	557-1015	824.02-887.25	794.77	685-968	779.87-809.67	0.0003
	Magnetic resonance imaging	123.09	74-158	117.84-128.34	100.65	67-132	97.32-103.98	< 0.0001
	Nuclear Medicine	21.64	8-37	19.76-23.52	20.92	12-35	19.68-22.15	0.507
	Ultrasound	325.82	215-395	314.29-337.35	264.22	192-323	256.97-271.46	< 0.0001
	Mammography	0.7	0-7	0.3-1.1	1.87	0-10	1.3-2.43	0.002
	Bone mineral densitometry	1.41	0-5	0.97-1.85	1.6	0-5	1.27-1.93	0.479
Outpatient	Angiography	9.0	2-26	7.47-10.53	17.08	5-30	15.86-18.31	< 0.0001
	Computed tomography	249.86	107-333	234.48-265.25	313.7	139-367	302.61-324.79	< 0.0001
	Fluoroscopy	17.61	6-37	15.2-20.03	24.78	5-43	22.97-26.59	< 0.0001
	Radiography	268.02	120-473	246.82-289.23	427.12	147-507	410.57-443.66	< 0.0001
	Magnetic resonance imaging	268.09	98-414	249.76-286.43	347.6	108-401	335.36-359.84	< 0.0001
	Nuclear medicine	50.84	19-88	46.88-54.8	71.72	31-112	68.14-75.3	< 0.0001
	Ultrasound	768.48	492-943	741.33-795.62	855.27	554-931	836.21-874.32	< 0.0001
	Mammography	15.82	2-24	14.2-17.44	17.75	8-23	16.87-18.63	0.027
	Bone mineral densitometry	36.77	4-72	301.13-42.42	50.9	0-72	47.57-54.23	< 0.0001
All classes	Angiography	51.84	30-70	48.58-55.11	51.6	30-63	49.76-53.44	0.892
	Computed tomography	1199.11	768-1458	1154.65-1243.58	1161.25	962-1339	1141.96-1180.54	0.090
	Fluoroscopy	148.77	96-205	141.2-145.35	158.18	92-184	153.59-162.78	0.027
	Radiography	2286.3	1602-2603	2214.97-2357.62	2520.92	2310-2718	2498.03-2543.80	< 0.0001
	Magnetic resonance imaging	403.30	175-556	380.71-425.88	466.8	200-526	452.6-481.0	< 0.0001
	Nuclear medicine	75.75	29-128	70.65-80.85	100.18	46-134	96.21-104.15	< 0.0001
	Ultrasound	1217.27	808-1491	1178.47-1256.08	1291.62	918-1429	1268.35-1314.88	.001
	Mammography	16.52	2-24	14.87-18.17	19.63	10-30	18.61-20.66	0.001
	Bone mineral densitometry	38.18	5-74	32.33-44.03	52.5	0-72	49.13-55.87	< 0.0001
Total	5437.05	3520-6441	5250.9-5623.8	5822.68	4645-6175	5750.97-5894.4	< 0.0001	

and second waves.

Comparison of the adult mean weekly 2019 (pre-COVID-19, January 2, 2019 to February 29, 2020, weeks 1 to 61) with 2020 (March 1 to December 31, 2020, weeks 61 to 104) mobile and non-mobile X-ray

Table 6 Summed imaging volumes and percentage change in adult mobile imaging volume across patient class in waves 1 and 2

Wave 1	2020 (weeks 63-68)	2019 (weeks 11-16)	% change	Wave 2	2020 (weeks 80-95)	2019 (weeks 28-43)	% change
ED	1952	372	424.7	ED	7526	1037	625.7
IP	2008	2138	-6.1	IP	8654	5845	48.1
Overall	3960	2510	57.8	Overall	16180	6882	135.1

ED: Emergency department; IP: Inpatient.

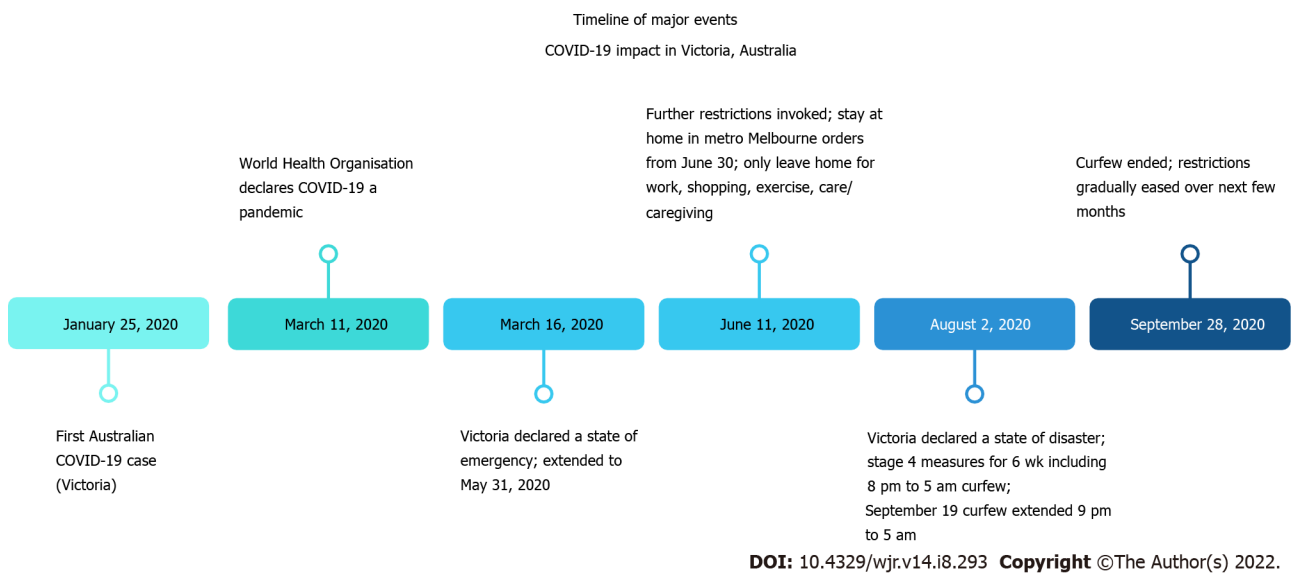


Figure 2 Timeline of significant events in Victoria, Australia during the first and second waves of the coronavirus disease 2019 pandemic. COVID-19: The coronavirus disease 2019.

imaging volumes, categorised by inpatient and emergency services (Table 7) shows statistically significant changes across all mobile and non-mobile imaging ($P = 0.001$ to < 0.0001). A strong correlation was observed between mobile and non-mobile imaging in the emergency setting (Spearman's correlation coefficient = -0.743 , $P = 0.000$). No correlation was observed in the inpatient setting (Spearman's correlation coefficient = -0.059 , $P = 0.554$). Figure 4 shows the weekly adult X-ray mobile and non-mobile imaging volumes.

Paediatrics

Total volume (all modalities): Total paediatric imaging volume across all modalities declined by 28.6% between March 11 and April 21, 2020 (weeks 63 to 68) compared to the same time in 2019 (March 13 and April 23, 2019, weeks 11 to 16). During the pandemic's second wave, paediatric imaging volume across all modalities declined by 6.6% between July 8 and October 27, 2020 (weeks 80 to 95) compared to the same time in 2019 (July 10 and October 29, 2019, weeks 28 to 43).

Volume by patient class: Table 8 shows the percentage of paediatric image volume change across all included modalities by patient class for weeks 11 to 16 and 28 to 43 in 2019 and weeks 63 to 68 and 80 to 95 in 2020.

During the pandemic's first wave between March 11 and April 21, 2020 (weeks 63-68), paediatric IP, OP and ED services declined by between 3.7% and 46.3% when compared to the same time in 2019 (March 13 and April 23 2019, weeks 11 to 16).

During the pandemic's second wave between July 8 and October 27, 2020 (weeks 80 to 95), paediatric IP, OP and ED services declined by between 16.1% and 28.5% when compared to the same time in 2019 (July 10 and October 29, 2019, weeks 28 to 43).

Volume by modality: During the pandemic's first wave between March 11 and April 21, 2020 (weeks 63 to 68), paediatric imaging modality services declined by between 18.6% and 47.8% and 18.6%, while angiography increased by 50% when compared to the same time in 2019 (March 13 and 23rd April 2019, weeks 11 to 16 shown in Table 9).

Table 7 Comparison of mean adult weekly imaging volumes for 2019 and 2020 including 95% CIs, by mobile and non-mobile imaging categorised by patient setting

Adult Setting	Modality	2020			2019			P value
		Mean	Min-max	95%CI	Mean	Min-max	95%CI	
Emergency	Mobile	366.64	63-550	330.11-403.17	63.23	45-85	60.86-65.61	< 0.0001
	Non-mobile	783.59	574-1190	739.11-828.08	1234.33	1095-1385	1216.54-1252.13	< 0.0001
Inpatient	Mobile	451.25	240-614	420.38-482.12	355.65	298-417	348.44-362.86	< 0.0001
	Non-mobile	404.00	310-514	386.64-421.36	438.93	339-564	428.10-449.77	0.001

Table 8 Summed imaging volumes and percentage change in paediatric imaging volume across patient class in waves 1 and 2

Wave 1	2020 (weeks 63-68)	2019 (weeks 11-16)	% change	Wave 2	2020 (weeks 80-95)	2019 (weeks 28-43)	% change
ED	804	1498	-46.3	ED	2780	3887	-28.5
IP	1799	2571	-30.0	IP	5818	6938	-16.1
OP	1162	1207	-3.7	OP	3041	3776	-19.5
Overall	3765	5276	-28.6	Overall	11639	14601	-20.3

ED: Emergency department; IP: Inpatient; OP: Outpatient.

Table 9 Summed imaging volumes and percentage change in paediatric imaging volume across modalities in wave 1

Wave 1	2020 (weeks 63-68)	2019 (weeks 11-16)	%
Angiography	9	6	50
Bone mineral densitometry	16	22	-27.3
Computed tomography	71	96	-26.0
Fluoroscopy	120	148	-18.9
General radiography	1896	2936	-35.4
Magnetic resonance imaging	253	340	-25.6
Nuclear medicine	12	23	-47.8
Ultrasound	1388	1705	-18.6

During the pandemic’s second wave between July 8 and October 27, 2020 (weeks 80 to 95), paediatric imaging modality services declined by between 5.2% and 36.7% when compared to the same time in 2019 (July 10 and October 29, 2019, weeks 28 to 43), shown in **Table 10**. **Figure 5** highlights the weekly paediatric modality imaging volumes.

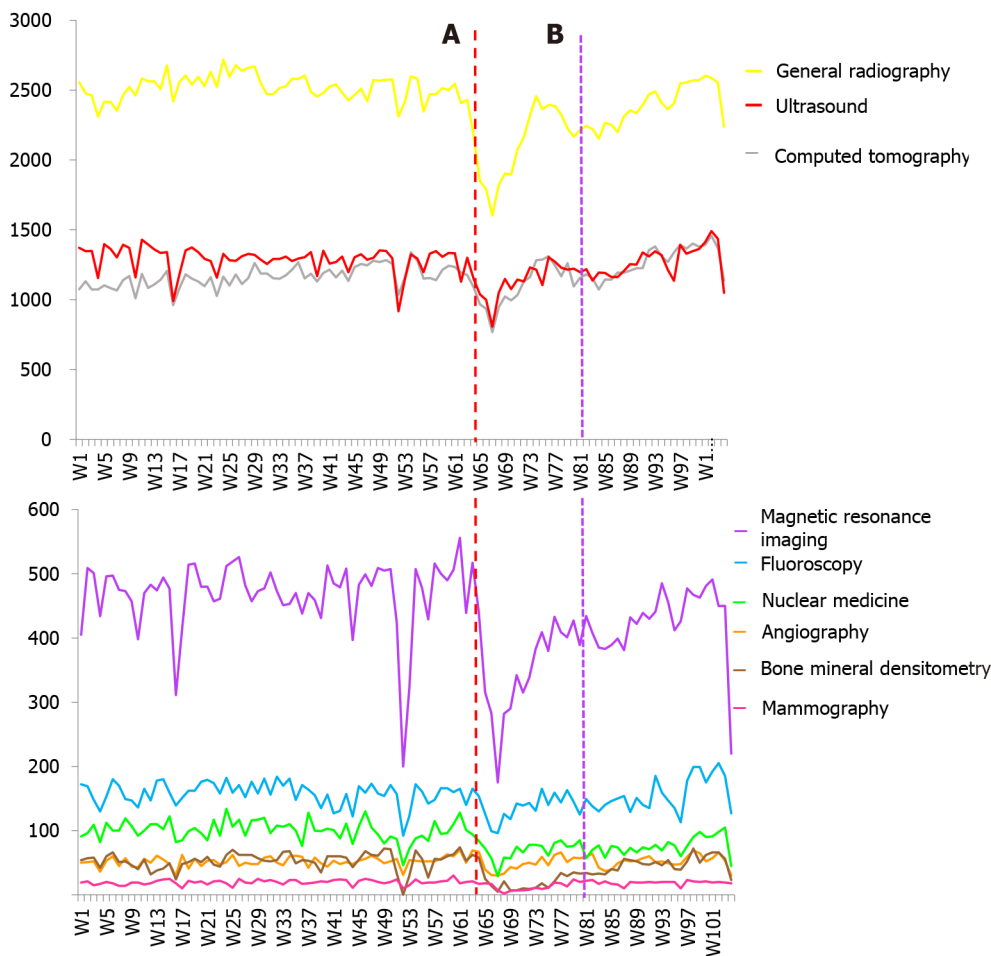
Comparison of the paediatric mean weekly 2019 (pre-COVID-19, Jan 2nd 2019 to 29th Feb 2020, weeks 1 to 61) with 2020 (March 1st to Dec 31st 2020 weeks 61 to 104) imaging volumes by modality, categorised by inpatient, outpatient and emergency services (**Table 11**) shows statistically significant changes in two emergency imaging modalities ($P = 0.0001$ to $P < 0.0001$), two inpatient imaging modalities ($P = 0.0003$ to $P < 0.0001$), and four outpatient imaging modalities ($P = 0.019$ to $P < 0.0001$). Overall changes across all patient classes were observed in five imaging modalities ($P = 0.037$ to $P < 0.0001$).

Mobile and non-mobile X-ray imaging: During the pandemic’s first wave in Victoria, total paediatric mobile imaging volume decreased by 0.7% between March 11 and April 21, 2020 (weeks 63 to 68) compared to the same time in 2019 (March 13 and April 23 2019, weeks 11 to 16). During the pandemic’s second wave, paediatric mobile imaging volume decreased by 6.7% between July 8 and October 27, 2020 (weeks 80 to 95) compared to the same time in 2019 (July 10 and October 29, 2019, weeks 28 to 43). **Table 12** highlights the mobile imaging changes across inpatient and emergency patient classes during the first and second waves.

Comparison of the paediatric mean weekly 2019 (pre-COVID-19, Jan 2nd 2019 to 29th Feb 2020, weeks 1 to 61) with 2020 (March 1st to Dec 31st 2020 weeks 61 to 104) mobile and non-mobile X-ray imaging volumes, categorised by inpatient and emergency services (**Table 13**) shows statistically significant

Table 10 Summed imaging volumes and percentage change in paediatric imaging volume across modalities in wave 2

Wave 2	2020 (weeks 80-95)	2019 (weeks 28-43)	%
Angiography	19	23	-17.4
Bone mineral densitometry	56	68	-17.6
Computed tomography	226	241	-6.2
Fluoroscopy	314	397	-20.9
General radiography	5472	7938	-31.1
Magnetic resonance imaging	874	922	-5.2
Nuclear medicine	38	60	-36.7
Ultrasound	4640	4952	-6.3



DOI: 10.4329/wjr.v14.i8.293 Copyright ©The Author(s) 2022.

Figure 3 Weekly adult imaging volumes by modality from January 2019 to December 2020 (Weeks 1 to 104). A: Week 63-commencement of first wave; B: Week 80-commencement of second wave.

changes across all mobile and non-mobile imaging ($P = 0.025$ to < 0.0001). The correlation between mobile and non-mobile imaging was -0.29 ($P = 0.003$) in the emergency setting, while no correlation was observed in the inpatient setting (Spearman correlation coefficient 0.044 , $P = 0.656$). **Figure 6** highlights the weekly paediatric X-ray mobile and non-mobile imaging volumes.

DISCUSSION

We found a reduction in the imaging volume between 2% and 30% across all adult patient classes and

Table 11 Comparison of mean paediatric weekly imaging volumes for 2019 and 2020 including 95%CIs, by imaging modality categorised by patient setting

Paediatric Setting	Modality	2020			2019			P value
		Mean	Min-max	95%CI	Mean	Min-max	95%CI	
Emergency	Angiography	0.02	0-1	-0.02-0.07	0.02	0-1	-0.02-0.05	-0.83
	Computed tomography	4.3	0-11	3.54-5.05	5.0	0-12	4.33-5.67	0.17
	Fluoroscopy	2.27	0-6	1.68-2.86	2.53	0-7	2.08-2.99	0.48
	Radiography	160.77	75-281	144.44 -177.11	206.58	123-268	198.64-214.52	< 0.0001
	Magnetic resonance imaging	1.7	0-5	1.33-2.08	1.87	0-5	1.49-2.24	0.55
	Nuclear Medicine	0.07	0-1	-0.01-0.15	0.05	0-1	-0.01-0.11	0.70
	Ultrasound	14.41	6-25	13.16-15.65	17.67	8-26	16.59-18.74	0.0001
Inpatient	Angiography	1.18	0-4	0.83-1.53	1.17	0-6	0.85-1.48	0.95
	Computed tomography	5.66	1-14	4.92-6.4	5.66	0-11	5.0-6.27	0.96
	Fluoroscopy	17.8	7-38	15.86-19.73	19.98	7-30	18.61-21.36	0.061
	Radiography	85.84	56-120	81.74-89.94	97.97	70-143	93.99- 101.95	< 0.0001
	Magnetic resonance imaging	25.73	11-41	23.6-27.86	25.05	8-41	23.41-26.69	0.61
	Nuclear Medicine	0.55	0-3	0.28-0.81	0.98	0-5	0.72-1.25	0.025
	Ultrasound	58.36	33-76	55.51-61.21	65.33	40-84	62.9-67.77	0.0003
	Bone mineral densitometry	0.82	0-4	0.47-1.17	1.27	0-4	1.01-1.53	0.038
Outpatient	Angiography	0.05	0-1	-0.02-0.11	0.38	0-3	0.20-0.57	0.003
	Computed tomography	4.43	1-9	3.82-5.04	4.28	0-10	3.75-4.82	0.72
	Fluoroscopy	2.25	0-7	1.7-2.8	2.72	0-9	2.22-3.22	0.22
	Radiography	121.2	66-197	110.62-131.79	167.88	87-215	161.21-174.55	< 0.0001
	Magnetic resonance imaging	25.48	10-37	23.49-27.46	28.82	11-47	26.92-30.72	0.019
	Nuclear medicine	2	0-6	1.54-2.46	2.47	0-6	2.08-2.86	0.13
	Ultrasound	198.77	92-266	186.88-210.66	208.77	117-260	201.54-215.99	0.13
	Bone mineral densitometry	1.86	0-8	1.37-2.35	2.8	0-7	2.35-3.25	0.007
All classes	Angiography	1.25	0-4	0.89-1.61	1.57	0-6	1.22-1.91	0.22
	Computed tomography	14.39	8-23	13.10-15.67	14.92	5-21	14.01-15.83	0.49
	Fluoroscopy	22.32	11-44	20.04-24.60	25.23	8-40	3.59-4.54	0.037
	Radiography	367.82	239-538	340.73-394.90	472.43	331-581	458.91-485.96	< 0.0001
	Magnetic resonance imaging	52.91	23-78	49.27-56.55	55.73	22-84	52.78-58.68	0.23
	Nuclear Medicine	2.61	0-8	2.01-3.21	3.5	0-7	3.05-3.95	0.017
	Ultrasound	271.55	149-346	258.11-284.98	291.77	184-350	283.07-300.46	0.010
	Bone mineral densitometry	2.68	0-9	2.03-3.33	4.07	0-8	3.59-4.54	0.001
	Total	735.52	476-1024	693.13-777.91	869.22	553-1016	845.88-892.55	< 0.0001

10% and 37% in adult imaging volumes by modality during the first wave of the pandemic. Nuclear Medicine was the modality most impacted, and angiography the least impacted. While periods analysed may differ slightly, the findings for adult imaging volumes were less than those reported in Germany (41%, all modalities)[14], New York (14% to 53%)[15], California, Florida, Michigan, Massachusetts and New York (40% to 70%)[16], and Ohio (53%)[17]. During the second wave of the pandemic, all adult radiology modalities reported a reduction of between 2% and 32% in imaging volumes and between 9% and 24% in imaging volumes across all patient classes. Adult computed tomography imaging volumes experienced a 2% increase. Nuclear medicine was the modality most impacted. This is less than the data obtained from Medicare reported by Sreedharan *et al*[12], who found that general radiography and ultrasound were most impacted, while computed tomography and nuclear medicine services were less

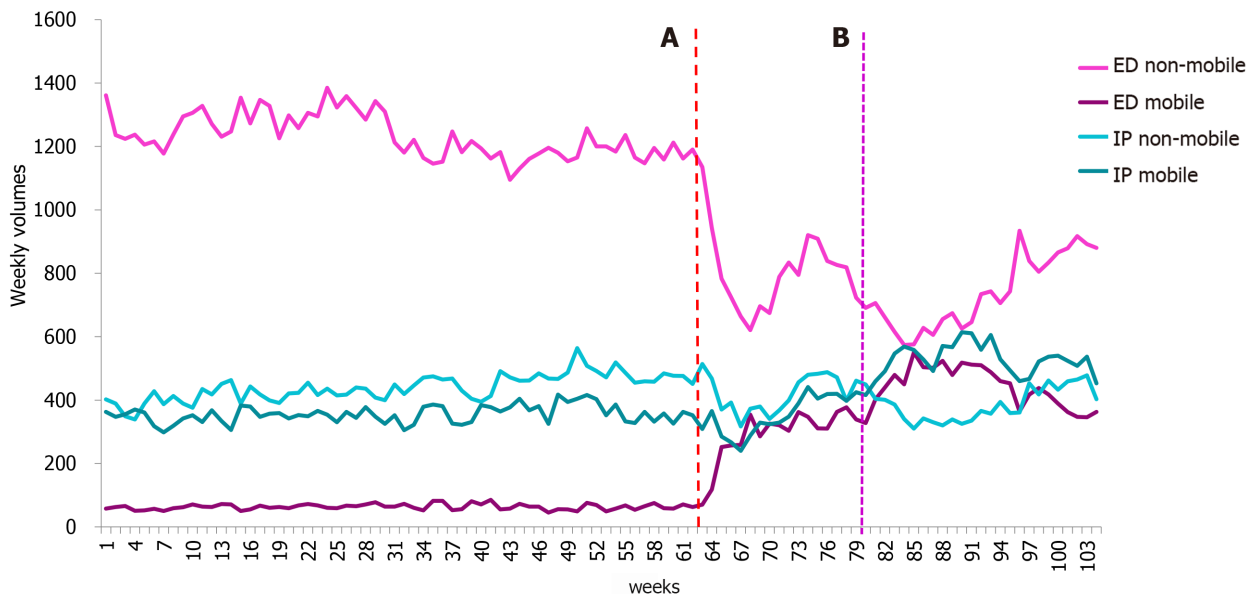
Table 12 Summed imaging volumes and percentage change in paediatric mobile imaging volume across patient class in waves 1 and 2

Wave 1	2020 (weeks 63-68)	2019 (weeks 11-16)	% change	Wave 2	2020 (weeks 80-95)	2019 (weeks 28-43)	% change
ED	44	32	37.5	ED	370	151	145.0
IP	400	415	-3.6	IP	1021	1340	-23.8
Overall	444	447	-0.7	Overall	1391	1491	-6.7

ED: Emergency department; IP: Inpatient.

Table 13 Comparison of mean paediatric weekly imaging volumes for 2019 and 2020 including 95% CIs, by mobile and non-mobile imaging categorised by patient setting

Paediatric Setting	Modality	2020			2019			P value
		Mean	Min-max	95%CI	Mean	Min-max	95%CI	
Emergency	Mobile	18.70	1-38	16.08-21.33	6.62	1-17	5.69-7.54	< 0.0001
	Non-mobile	142.07	63-251	126.62 - 157.52	199.97	121-261	192.12 - 207.81	< 0.0001
Inpatient	Mobile	66.89	44-95	63.13-70.64	72.95	46-102	69.31- 76.59	0.025
	Non-mobile	18.95	7-33	17.22-20.69	25.00	9-42	23.24-26.76	< 0.0001



DOI: 10.4329/wjr.v14.i8.293 Copyright ©The Author(s) 2022.

Figure 4 Weekly adult X-ray mobile and non-mobile imaging volumes from January 2019 to December 2020 (Weeks 1 to 104). A: Week 63-commencement of first wave; B: Week 80 commencement of second wave. ED: Emergency department; IP: Inpatient.

affected. It was unclear whether paediatric data were included in their analysis[12].

Similarly, during the first wave of the pandemic, there was a reduction in paediatric imaging volumes of between 19% and 48% across all modalities except for angiography reporting a 50% increase in the imaging volume. There was a 4%-46% reduction across all paediatric patient classes. Nuclear Medicine was the modality most impacted, with ultrasound being the least impacted. While paediatric emergency patient presentations decreased by 25% in one Sydney health service, we observed a larger decrease in paediatric imaging service utilisation in the emergency department and inpatient settings[18].

During the second wave of the pandemic, there was a reduction of between 5% and 37% in paediatric modality cases and between 16% and 28% across paediatric patient classes. Nuclear Medicine was most impacted, while magnetic resonance imaging was least affected.

Decline in adult services (2% IP, 30% OP, 26% ED) were generally less to those reported by Naidich *et al*[15] (ED (27%), OP (57%), IP (14%)). Furthermore, outpatient services were reported in South Africa (40% over six months)[5]. outpatient imaging (58%, 72%[14,17], inpatient imaging (41%, 43%)[14,17],

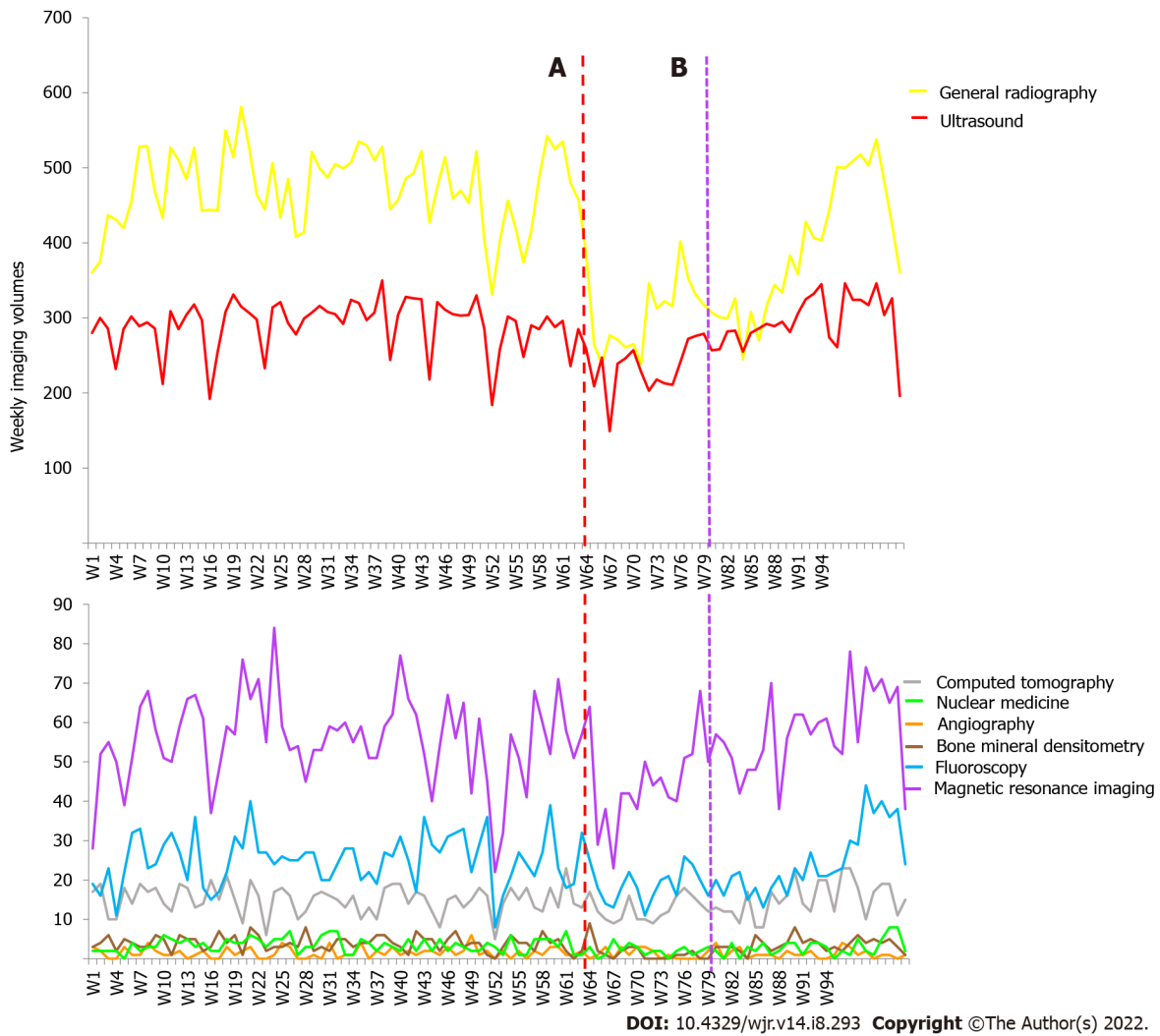


Figure 5 Weekly paediatric imaging volumes by modality from January 2019 to December 2020 (Weeks 1 to 104). A: Week 63-commencement of first wave; B: Week 80 commencement of second wave.

and emergency department imaging (39%, 49%)[14,17] in Ohio and Berlin highlighted greater declines in demands than we observed. Australia utilised the experience of other nations in preparation for COVID-19. For example, Australia reduced elective medical procedures in line with other countries and implemented PPE measures, social distancing, and stay-at-home measures for non-essential workers[5]. We found that most of our outpatient imaging services were severely impacted (19%-50% loss in imaging volume) by new social distancing and appropriate cleaning measures. Inpatient services were also affected by the decline in elective surgeries, while emergency patient volume was reduced due to more people isolating at home.

From July to September 2020, Australia experienced the pandemic’s second wave. This was most prevalent in Victoria. The government implemented border closures, curfews, limiting movement to a five-kilometre radius, working from home for non-essential workers, business and education closures, wearing masks indoors and outdoors, and physical distancing measures to reduce COVID-19 cases[5]. During this phase of the pandemic, we observed a minor reduction in patient volume across all modalities at our institution compared to the first wave’s impact. This could be due to health services becoming better equipped, informed and organised to manage pandemic outbreaks[5]; earlier diagnosis of COVID-19 *via* more rigorous PCR testing[5,20]; patients were better informed about the risks of contracting COVID-19, thus more likely to seek medical care. Earlier in the pandemic, it had been reported that patients were afraid to come to the hospital, potentially compromising their health[21,22].

Angiography

Our angiography statistics represented interventional radiology procedures performed in the angiography suite primarily guided by fluoroscopy or ultrasound. Like other modalities, the angiography suite was substantially impacted in outpatient volume when the Department of Health and Human Services ruled that only Category 1 patients could attend. In April and August 2020, there was a decrease in inpatient studies. However, recovery in this patient class was swift, with patient

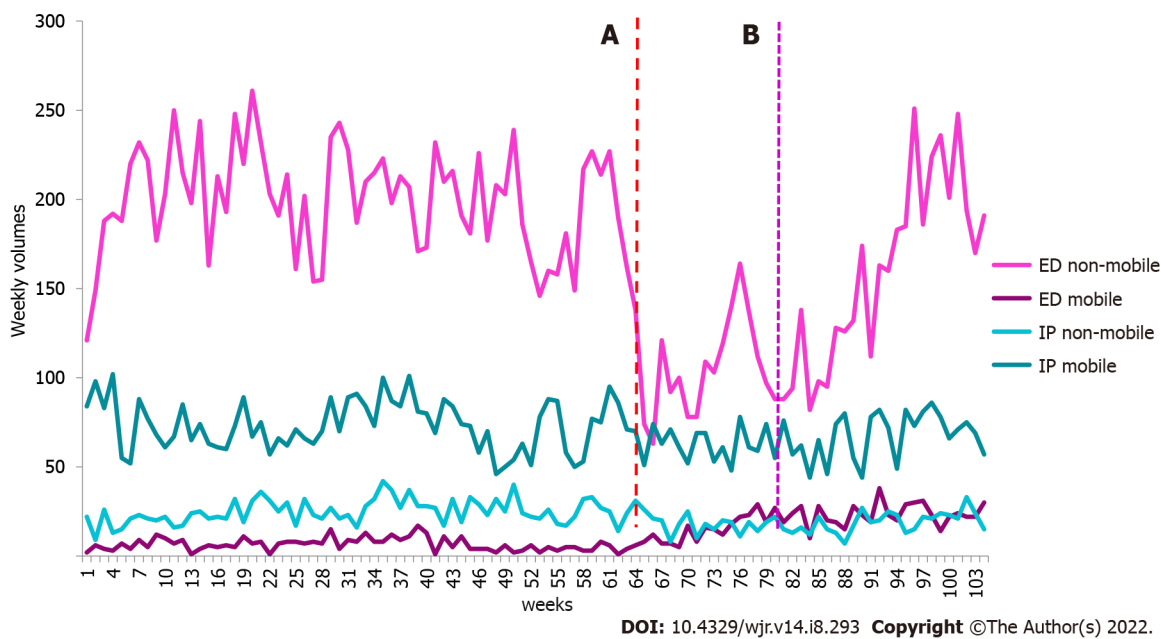


Figure 6 Weekly paediatric X-ray mobile and non-mobile imaging volumes from January 2019 to December 2020 (Weeks 1 to 104). A: Week 63-commencement of first wave; B: Week 80 commencement of second wave. ED: Emergency department; IP: Inpatient.

volume surpassing pre-COVID attendances. Patients delayed procedures during the first wave of COVID-19 for fear of contracting the virus while in hospital.[7] This increased unplanned hospital admissions with patients requiring procedures, leading to increased service demand. Some patients may have also been scheduled to relieve burgeoning waitlist times.

Bone mineral densitometry

United Kingdom bone mineral densitometry (BMD) wait lists increased during the pandemic, resulting in treatment delays for osteoporosis[23]. We observed the same relative reduction in imaging volumes during the first and second waves of the pandemic, likely determined by clinic closures[24], use of telehealth to minimise hospital visits[5], staff redeployment[25], or delaying medical treatment[26].

CT

CT was one of the modalities least impacted by new policies and guidelines implemented during the pandemic. This is not surprising given the importance of CTPA for early contribution to patient diagnosis[5]. While early in the pandemic, CT was the modality of choice for assisting in COVID-19 diagnosis[5], this changed due to the high radiation doses and availability of PCR testing[5]. While there was a reduction in CT demand during the peak waves of the pandemic, we observed an increase in CT utilisation during the second wave of the pandemic, consistent with other reports[27]. During the pandemic, outpatient CT studies for malignancy staging were delayed based on criteria set by senior management due to the risk of cross-contamination between inpatients and outpatients. Access to an independent CT scanner within the hospital at an onsite research facility improved workflow for this patient cohort. During the pandemic, elderly Victorians in aged care died from the virus as transmission rates among staff members in certain aged care facilities increased. The government intervened by placing aged care residents into Victorian hospitals as a safety measure for our most vulnerable. The increase in inpatient CT scans during this period can likely be attributed to this mandate.

Fluoroscopy

Many non-clinically urgent fluoroscopy studies, such as barium swallows for outpatient studies, were placed on hold or rescheduled during the pandemic. Following Victoria's second wave, there was a resurgence of patient bookings from October 2020. The end of September 2020 marked the easing of stage 4 restrictions, with COVID-19 infections decreasing significantly. Thus outpatient and inpatient bookings were rescheduled over the coming months to cope with demand. A significant change in imaging volume was observed between June and July, with a below-average patient number in July (Figure S2). This can be likely attributed to the similar timing of outbreaks in COVID-19 at aged care centres, prompting the Victorian government to move aged care residents to hospitals to prevent further COVID-19-related deaths.

General radiography

While adult general X-ray was particularly impacted during the pandemic's first wave, likely due to the cancellation of elective surgery and outpatient clinics, less impact was observed during the second wave. Conversely, paediatric general X-ray imaging volumes significantly reduced during both pandemic waves. In 2020, the utilisation of mobile imaging saw significant growth. This can be attributed to workflow changes such as infection control measures to reduce patient movement[28]. Senior management purchased extra mobile imaging systems to manage the increased demand, contributing to the observed changes. Other imaging protocol modifications to reduce the risk of contracting COVID-19, such as imaging through glass, were performed but not used routinely at our institution[8]. The utilisation of mobile imaging more than doubled during the peak of the pandemic at our institution, particularly in the emergency setting. This is comparable with the findings of others. Surveyed Western Australian medical imaging professionals perceived increased mobile chest imaging, particularly in the public hospital setting[29]. At the same time, in Singapore, there was a three-fold increase in emergency department mobile imaging usage[30]. Although mobile imaging utilisation increased, there was little change in radiographer-reported doses[31]. There was a slight shift in imaging regions other than the chest (data not shown)[31]. We also observed that fixed X-ray imaging decreased when adult mobile imaging increased in the emergency setting. This was likely to reduce transmission risk and manage potential increased demand[8,32]. The greatest impact on adult mobile imaging usage was observed during the pandemic's second wave, when the risk of cold and influenza was heightened (July-September 2020)[33].

MRI

We observed appreciable declines due to work practice changes implemented in adult and paediatric MRI services during the pandemic contributed to long waiting lists across our network. Elective general anaesthetic cases were placed "on hold" as per Victorian Government recommendations and aerosol-generating procedure policies to allow room resting and cleaning that extended the total examination time, particularly impacted paediatric services[3,34,35].

Mammography

As with other imaging modalities, our mammography service also experienced a reduction in imaging volumes during the first and second waves of the pandemic. This is consistent with other findings, though to a lesser extent, in our health service[15,36,37]. In Australia, breast screening services were temporarily suspended, with services reopening based upon government recommendations. Similarly, changes in workflow required stricter patient management protocols and cleaning protocols to minimise transmission risk[28,37,38].

Nuclear medicine

We found that nuclear medicine, then mammography were the modalities most impacted by the pandemic and consistent with the findings of others[15,16,36,37]. This could, in part, be due to logistical changes to isotope supply. From March to July and October to November 2020, there were significant issues with isotope transportation locally and overseas, particularly during the first wave of the pandemic. Due to unforeseen mechanical problems at the Australian Nuclear Science and Technology Organisation manufacturing site, there were also supply interruptions. These included a broken conveyer belt, storm causing electrical faults, production failure, isotope refinement and contamination issues. Other challenges included scheduled reactor shutdown, with difficulty in alternate isotope sourcing to meet demand. These interruptions could have contributed to the significant changes observed.

Ultrasound

At our institution, ultrasound was less impacted than other modalities, which is consistent with other experiences[16,19]. However, data from Germany found ultrasound was the most significantly affected imaging modality, though not all modalities were included in their analysis[14]. Ultrasound services were transformed considerably in the early weeks of the outbreak, with the expansion of ambulatory centres to provide 'clean' sites. In the main hospital centres, there was a substantive need for mobile ultrasound examination both in ED and in the wards. In the lead-up to the pandemic, we observed a decrease in ED patients. ED patient imaging volume stabilised during the pandemic, with some growth observed. The reason for this surge was thought to be multi-factorial. There seemed to be a tendency for patients to attend an ED rather than their local GP. It was also believed that patients' examinations were initially delayed, and the surge compensated for this. There was no obvious change in the referral patterns for the types of examinations requested. Anecdotally, point of care ultrasound (PoCUS) examinations decreased across this period. This seemed to be related to clinicians minimising patient contact and deciding to suspend PoCUS training.

Inpatient services overall increased, but there were small reductions in patient volumes during the first and second waves. While other services reported some value for lung ultrasound, this was not used in evaluating COVID-19-positive patients at our institution[10]. Consistent with the other modalities, we

did see a decrease in outpatient attendances, which returned relatively quickly. This is likely due to outpatient clinic closures, halting non-essential ultrasound intervention, and patients' choice to delay their scans. As with other modalities, ultrasound was less impacted during the second wave. Obstetric cases throughout this period were deemed an essential service and did not change. Sonographers were activated to perform blood pressures as part of a third-trimester pathway as many women were seen *via* telehealth. The Early Pregnancy Bleeding pathway and clinic were also relocated to ultrasound. Minor changes were made to scan protocols. Targeted scans were introduced for high-risk patients. The timing of paediatric hip screening was adjusted to minimise the risk of repeat examinations.

Paediatrics

Overall, there was a decrease of approximately 55% from April to October 2020 compared to 2019. Recovery of paediatric imaging, particularly after the second wave (September to December 2020), was more rapid, coinciding with the gradual reduction in Melbourne's COVID-19 case numbers and the subsequent easing of restrictions. Many patients and families deferred non-urgent imaging during the lockdown. Moreover, lockdown, home-schooling and suspension of group sports further reduced paediatric cases from sporting injuries[39]. We did observe a slight increase in some services, such as MRI, during 2020 despite COVID-19 disruption, as services returned to pre-COVID-19 demand. This was due to the new software and hardware upgrade in February 2020, reducing the total scan time and potentially increasing patient throughput while providing additional time for cleaning. As observed with adult modality data, following lockdowns in April and July-September 2020 and elective surgery deferral, there was a dramatic decrease in paediatric imaging across all modalities, except for angiography (minimal imaging volume). Recovery was observed between the first and second waves. However, it did not reach the pre-COVID-19 Levels. We also observed an increase in mobile usage in emergencies to help reduce the transmission risk.

Study limitations

While our health service cared for the first Australian COVID-19 patient, other health services across Melbourne, particularly in the north and west, experienced higher caseloads. Consequently, these health services may have experienced more significant declines in radiology services than we observed across our health services. Our institution purchased additional mobile X-ray units to prepare for the pandemic, contributing to the increased use. Of note, the MRI software and hardware upgrades did not significantly increase the imaging volume. However, they did provide additional time for practice changes, such as improved infection control measures. Nuclear medicine experienced even more significant challenges during the pandemic due to unforeseen interruptions to isotope supplies as a confounding variable. This required additional patient rescheduling, often at short notice. Given that data was analysed between 2019 and 2020, some underlying baseline year-to-year variability may be contributing to the findings. Timeframes defining COVID-19 may vary worldwide, making data comparison somewhat difficult.

This work represents one large Victorian health service; however, it may not be generalisable to other health services.

Lessons learned: (1) Once-in-a-lifetime events such as a global pandemic can significantly impact workflow across imaging modalities, with the need to implement new processes; (2) Our experience during the pandemic was not the same as those experiences described by other nations due to the variation in severity and (3) Modalities across our health network were impacted differently due to changes in service demands, closures of outpatient clinics, and rescheduling elective surgeries.

CONCLUSION

Collected data provides an evidence-based insight into changing imaging volume related to COVID-19. This information will allow the network to predict the dynamic demands in imaging more accurately and promptly adapt its policies. We found that adult CT, angiography and ultrasound recovery following the first and second waves of the pandemic recovered faster than nuclear medicine, BMD and MRI. Paediatric MRI and ultrasound recovered faster than nuclear medicine and general radiography following the first and second waves of the pandemic. Modalities were less impacted during the second wave (July-September 2020) than during the first wave (April 2020), except for angiography outpatients. At our health network, nuclear medicine was the imaging modality most impacted by COVID-19 in adult and paediatric settings. There may have been other factors, however, influencing these results. Adult CT imaging increased during the second wave, while paediatric ultrasound was the least affected. Radiology departments can minimise the impact of future COVID-19/public health outbreaks on imaging volumes by ensuring each modality is appropriately resourced to continue providing safe and patient-centred care.

ARTICLE HIGHLIGHTS

Research background

Medical imaging modalities worldwide were significantly impacted by the the coronavirus disease 2019 (COVID-19) pandemic; however, each country's experience differed. This study provides an in-depth analysis of the impact on adult, paediatric, inpatient, outpatient, emergency and mobile services across the first and second waves of the COVID-19 pandemic in a large public health network in Victoria, Australia.

Research motivation

This work provides evidence for managing and redeploying resources during "once in a lifetime" events such as a pandemic and impact duration. Using this work, modelling and forecasting anticipated changes to imaging demand can be performed, allowing optimal utilisation of departmental staffing to manage workloads.

Research objectives

To identify adult and paediatric imaging volume changes, including mobile imaging across a large Victorian public hospital network. We realised our objectives, and the findings highlighted significant differences across the modalities analysed. Future research could monitor the long-term impacts of such events, such as staff burnout or opportunities for additional training to address deficiencies identified.

Research methods

The use of statistical methods in data analysis highlighted the modalities, patient classes and differences between adult and paediatric imaging. Particularly, methods to identify any correlation between mobile and non-mobile imaging volumes were novel.

Research results

We identified that the greatest impact occurred in Nuclear Medicine during the first and second waves, with all modalities less affected during the second wave; other modalities such as computed tomography were less impacted, requiring greater resources to manage service demand. We observed a shift in regions imaged using mobile imaging. It would be essential to understand this impact regarding image quality, workflow and patient radiation dose.

Research conclusions

Medical imaging modality services across a large Victorian public health network were significantly affected during the COVID-19 pandemic; however, the impact on different modalities varied relative to studies performed in other countries. It is essential to have a broad perspective of the impact to each imaging modality in both the adult and paediatric context to help better address the need for workflow changes. It is essential to consider whether imaging services are inversely correlated to manage optimal departmental resourcing.

Research perspectives

Future research could further investigate the long-term impact of lockdowns and the pandemic on imaging modality volumes and their recovery. This can help inform future budgeting requirements regarding the need for additional equipment and staffing to manage continuous workflow demands.

FOOTNOTES

Author contributions: Pinson JA, Badawy MK, designed and coordinated the study; Pinson JA, Badawy MK, Diep ML, Krishnan V, Aird C, Cooper C, Leong C, Chen J, Paul E and Ardley N performed the data collection, analysed and interpreted the data; Pinson JA, Badawy MK, Diep ML, Krishnan V, Aird C, Cooper C, Leong C, Chen J, Paul E and Ardley N wrote the manuscript; all authors have read, edited and approved the final version of the manuscript.

Institutional review board statement: The study was reviewed and approved by the Monash Health Human Research Ethics Committee Institutional Review Board [(Approval No. QA/69362/MonH-2020-235260(v1))].

Informed consent statement: Patients were not required to give informed consent to the study because the analysis used anonymous clinical data that were obtained after each patient agreed to treatment by written consent. For full disclosure, the details of the study are published on the home page of Fukushima Medical University.

Conflict-of-interest statement: We have no financial relationships to disclose.

Data sharing statement: Technical appendix, statistical code, and dataset available from the corresponding author at

mohamed.badawy@monashhealth.org.

Open-Access: This article is an open-access article that was selected by an in-house editor and fully peer-reviewed by external reviewers. It is distributed in accordance with the Creative Commons Attribution NonCommercial (CC BY-NC 4.0) license, which permits others to distribute, remix, adapt, build upon this work non-commercially, and license their derivative works on different terms, provided the original work is properly cited and the use is non-commercial. See: <https://creativecommons.org/licenses/by-nc/4.0/>

Country/Territory of origin: Australia

ORCID number: Jo-Anne Pinson 0000-0001-6654-0278; My Linh Diep 0000-0001-5007-3046; Vinay Krishnan 0000-0002-0062-5348; Caroline Aird 0000-0002-3942-4375; Cassie Cooper 0000-0001-8504-8086; Christopher Leong 0000-0001-9496-799X; Jeff Chen 0000-0003-4553-9221; Nicholas Ardley 0000-0002-2251-8754; Eldho Paul 0000-0003-1263-7255; Mohamed Khaldoun Badawy 0000-0001-8029-9951.

Corresponding Author's Membership in Professional Societies: The Australasian Radiation Protection, 63506470.

S-Editor: Wang LL

L-Editor: A

P-Editor: Wang LL

REFERENCES

- 1 **Cucinotta D**, Vanelli M. WHO Declares COVID-19 a Pandemic. *Acta Biomed* 2020; **91**: 157-160 [PMID: 32191675 DOI: 10.23750/abm.v91i1.9397]
- 2 **Islam MS**, Rahman KM, Sun Y, Qureshi MO, Abdi I, Chughtai AA, Seale H. Current knowledge of COVID-19 and infection prevention and control strategies in healthcare settings: A global analysis. *Infect Control Hosp Epidemiol* 2020; **41**: 1196-1206 [PMID: 32408911 DOI: 10.1017/ice.2020.237]
- 3 **COVIDSurg Collaborative**. Elective surgery cancellations due to the COVID-19 pandemic: global predictive modelling to inform surgical recovery plans. *Br J Surg* 2020; **107**: 1440-1449 [PMID: 32395848 DOI: 10.1002/bjs.11746]
- 4 **Weissman GE**, Crane-Droesch A, Chivers C, Luong T, Hanish A, Levy MZ, Lubken J, Becker M, Draugelis ME, Anesi GL, Brennan PJ, Christie JD, Hanson CW 3rd, Mikkelsen ME, Halpern SD. Locally Informed Simulation to Predict Hospital Capacity Needs During the COVID-19 Pandemic. *Ann Intern Med* 2020; **173**: 21-28 [PMID: 32259197 DOI: 10.7326/M20-1260]
- 5 **Tan BS**, Dunnick RN, Gangi A, Goergen S, Jin Z-Y, Neri E, Nomura CH, Pitcher RD, Yee J, Mahmood U. RSNA International Trends: A Global Perspective on the COVID-19 Pandemic and Radiology in Late 2020. *Radiology* 2021; **299**: E193-E203 [DOI: 10.1148/radiol.2020204267]
- 6 **Currie G**. COVID19 impact on nuclear medicine: an Australian perspective. *Eur J Nucl Med Mol Imaging* 2020; **47**: 1623-1627 [PMID: 32296883 DOI: 10.1007/s00259-020-04812-z]
- 7 **Amukotuwa SA**, Bammer R, Maingard J. Where have our patients gone? *J Med Imaging Radiat Oncol* 2020; **64**: 607-614 [DOI: 10.1111/1754-9485.13093]
- 8 **Brady Z**, Scoullar H, Grinsted B, Ewert K, Kavvoudias H, Jarema A, Crocker J, Wills R, Houston G, Law M, Varma D. Technique, radiation safety and image quality for chest X-ray imaging through glass and in mobile settings during the COVID-19 pandemic. *Phys Eng Sci Med* 2020; **43**: 765-779 [PMID: 32662037 DOI: 10.1007/s13246-020-00899-8]
- 9 **Seghers MC**, Seghers VJ, Sher AC, Jadhav SP, States LJ, Trout AT, Alazraki AL, Sammer MBK. Working from home during the COVID-19 pandemic: surveys of the Society for Pediatric Radiology and the Society of Chiefs of Radiology at Children's Hospitals. *Pediatr Radiol* 2022; **52**: 1242-1254 [PMID: 35229184 DOI: 10.1007/s00247-022-05299-6]
- 10 **Blažić I**, Brkljačić B, Frija G. The use of imaging in COVID-19-results of a global survey by the International Society of Radiology. *Eur Radiol* 2021; **31**: 1185-1193 [PMID: 32939620 DOI: 10.1007/s00330-020-07252-3]
- 11 **Eastgate P**, Neep MJ, Steffens T, Westerink A. COVID-19 Pandemic-considerations and challenges for the management of medical imaging departments in Queensland. *J Med Radiat Sci* 2020; **67**: 345-351 [PMID: 32827241 DOI: 10.1002/jmrs.423]
- 12 **Sreedharan S**, Mian M, McArdle DJT, Rhodes A. The impact of the COVID-19 pandemic on diagnostic imaging services in Australia. *J Med Imaging Radiat Oncol* 2022; **66**: 377-384 [PMID: 34288493 DOI: 10.1111/1754-9485.13291]
- 13 **Vöö S**, Dizdarevic S. Single photon emission computed tomography lung perfusion imaging during the COVID-19 pandemic: does nuclear medicine need to reconsider its guidelines? *Nucl Med Commun* 2020; **41**: 991-993 [PMID: 32796489 DOI: 10.1097/MNM.0000000000001246]
- 14 **Fleckenstein FN**, Maleitzke T, Böning G, Kahn J, Büttner L, Gebauer B, Aigner A, Hamm B. Decreased Medical Care During the COVID-19 Pandemic-A Comprehensive Analysis of Radiological Examinations. *Rofö* 2021; **193**: 937-946 [PMID: 33735933 DOI: 10.1055/a-1368-5047]
- 15 **Naidich JJ**, Boltyenkov A, Wang JJ, Chusid J, Hughes D, Sanelli PC. Impact of the Coronavirus Disease 2019 (COVID-19) Pandemic on Imaging Case Volumes. *J Am Coll Radiol* 2020; **17**: 865-872 [PMID: 32425710 DOI: 10.1016/j.jacr.2020.05.004]
- 16 **Norbash AM**, Moore AV Jr, Recht MP, Brink JA, Hess CP, Won JJ, Jain S, Sun X, Brown M, Enzmann D. Early-Stage Radiology Volume Effects and Considerations with the Coronavirus Disease 2019 (COVID-19) Pandemic: Adaptations, Risks, and Lessons Learned. *J Am Coll Radiol* 2020; **17**: 1086-1095 [PMID: 32717183 DOI: 10.1016/j.jacr.2020.07.001]

- 17 **Vagal A**, Mahoney M, Allen B, Kapur S, Udstuen G, Wang L, Braley S, Makramalla A, Chadalavada S, Choe KA, Scheler J, Brown A, England E, Hudepohl J, Rybicki FJ. Rescheduling Nonurgent Care in Radiology: Implementation During the Coronavirus Disease 2019 (COVID-19) Pandemic. *J Am Coll Radiol* 2020; **17**: 882-889 [PMID: [32473108](#) DOI: [10.1016/j.jacr.2020.05.010](#)]
- 18 **Kam AW**, Chaudhry SG, Gunasekaran N, White AJ, Vukasovic M, Fung AT. Fewer presentations to metropolitan emergency departments during the COVID-19 pandemic. *Med J Aust* 2020; **213**: 370-371 [PMID: [32946589](#) DOI: [10.5694/mja2.50769](#)]
- 19 **Naidich JJ**, Boltyenkov A, Wang JJ, Chusid J, Hughes D, Sanelli PC. Coronavirus Disease 2019 (COVID-19) Pandemic Shifts Inpatient Imaging Utilization. *J Am Coll Radiol* 2020; **17**: 1289-1298 [PMID: [32622817](#) DOI: [10.1016/j.jacr.2020.06.011](#)]
- 20 **Wang C**, Horby PW, Hayden FG, Gao GF. A novel coronavirus outbreak of global health concern. *Lancet* 2020; **395**: 470-473 [PMID: [31986257](#) DOI: [10.1016/S0140-6736\(20\)30185-9](#)]
- 21 **Iezzi R**, Valente I, Cina A, Posa A, Contegiacomo A, Alexandre A, D'Argento F, Lozupone E, Barone M, Giubolini F, Milonia L, Romi A, Scrofani AR, Pedicelli A, Manfredi R, Colosimo C. Longitudinal study of interventional radiology activity in a large metropolitan Italian tertiary care hospital: how the COVID-19 pandemic emergency has changed our activity. *Eur Radiol* 2020; **30**: 6940-6949 [PMID: [32607633](#) DOI: [10.1007/s00330-020-07041-y](#)]
- 22 **Wong LE**, Hawkins JE, Langness S, L. MK, Iris P, Sammann A. Where Are All the Patients? *N Engl J Med Catalyst Innovations in Care Delivery* 2020; **1**: 12. [DOI: [10.1056/CAT.20.0193](#)]
- 23 **Sapkota HR**, Nune A, Bateman J, Venkatachalam S. A pragmatic proposal for triaging DXA testing during the COVID-19 global pandemic. *Osteoporos Int* 2021; **32**: 1-6 [PMID: [33146750](#) DOI: [10.1007/s00198-020-05722-4](#)]
- 24 **Andrikopoulos S**, Johnson G. The Australian response to the COVID-19 pandemic and diabetes-Lessons learned. *Diabetes Res Clin Pract* 2020; **165**: 108246 [PMID: [32502693](#) DOI: [10.1016/j.diabres.2020.108246](#)]
- 25 **Shi J**, Giess CS, Martin T, Lemaire KA, Curley PJ, Bay C, Mayo-Smith WW, Boland GW, Khorasani R. Radiology Workload Changes During the COVID-19 Pandemic: Implications for Staff Redeployment. *Acad Radiol* 2021; **28**: 1-7 [PMID: [33036897](#) DOI: [10.1016/j.acra.2020.09.008](#)]
- 26 **Czeisler MÉ**, Kennedy JL, Wiley JF, Facer-Childs ER, Robbins R, Barger LK, Czeisler CA, Rajaratnam SMW, Howard ME. Delay or avoidance of routine, urgent and emergency medical care due to concerns about COVID-19 in a region with low COVID-19 prevalence: Victoria, Australia. *Respirology* 2021; **26**: 707-712 [PMID: [34081819](#) DOI: [10.1111/resp.14094](#)]
- 27 **Garg M**, Prabhakar N, Bhalla AS. Cancer risk of CT scan in COVID-19: Resolving the dilemma. *Indian J Med Res* 2021; **153**: 568-571 [PMID: [34596597](#) DOI: [10.4103/ijmr.ijmr_1476_21](#)]
- 28 **ACR Recommendations for the use of Chest Radiography and Computed Tomography (CT) for Suspected COVID-19 Infection.** *Am Coll Radiol* 2020, March 11. [cited 15 July 2021]. Available from: <https://psnet.ahrq.gov/issue/acr-recommendations-use-chest-radiography-and-computed-tomography-ct-suspected-covid-19>
- 29 **Dann C**, Sun Z. The impact of COVID-19 on Western Australian medical imaging clinical practice and workplace. *J Med Radiat Sci* 2022 [PMID: [35555866](#) DOI: [10.1002/jmrs.594](#)]
- 30 **Goh Y**, Chua W, Lee JKT, Ang BWL, Liang CR, Tan CA, Choong DAW, Hoon HX, Ong MKL, Quek ST. Operational Strategies to Prevent Coronavirus Disease 2019 (COVID-19) Spread in Radiology: Experience From a Singapore Radiology Department After Severe Acute Respiratory Syndrome. *J Am Coll Radiol* 2020; **17**: 717-723 [PMID: [32298643](#) DOI: [10.1016/j.jacr.2020.03.027](#)]
- 31 **Yeung P**, Pinson JA, Lawson M, Leong C, Badawy MK. COVID-19 pandemic and the effect of increased utilisation of mobile X-ray examinations on radiation dose to radiographers. *J Med Radiat Sci* 2022; **69**: 147-155 [PMID: [35180810](#) DOI: [10.1002/jmrs.570](#)]
- 32 **Koehler D**, Ozga AK, Molwitz I, May P, Görlich HM, Keller S, Adam G, Yamamura J. Time series analysis of the demand for COVID-19 related chest imaging during the first wave of the SARS-CoV-2 pandemic: An explorative study. *PLoS One* 2021; **16**: e0247686 [PMID: [33657140](#) DOI: [10.1371/journal.pone.0247686](#)]
- 33 **Reichert TA**, Simonsen L, Sharma A, Pardo SA, Fedson DS, Miller MA. Influenza and the winter increase in mortality in the United States, 1959-1999. *Am J Epidemiol* 2004; **160**: 492-502 [PMID: [15321847](#) DOI: [10.1093/aje/kwh227](#)]
- 34 **van Doremalen N**, Bushmaker T, Morris DH, Holbrook MG, Gamble A, Williamson BN, Tamin A, Harcourt JL, Thornburg NJ, Gerber SI, Lloyd-Smith JO, de Wit E, Munster VJ. Aerosol and Surface Stability of SARS-CoV-2 as Compared with SARS-CoV-1. *N Engl J Med* 2020; **382**: 1564-1567 [PMID: [32182409](#) DOI: [10.1056/NEJMc2004973](#)]
- 35 **Raissaki M**, Shelmerdine SC, Damasio MB, Toso S, Kvist O, Lovrenski J, Hirsch FW, Görkem SB, Paterson A, Arthurs OJ, Rossi A, van Schuppen J, Petit P, Argyropoulou MI, Offiah AC, Rosendahl K, Caro-Domínguez P. Management strategies for children with COVID-19: ESPR practical recommendations. *Pediatr Radiol* 2020; **50**: 1313-1323 [PMID: [32621013](#) DOI: [10.1007/s00247-020-04749-3](#)]
- 36 **Parikh KD**, Ramaiya NH, Kikano EG, Tirumani SH, Pandya H, Stovicek B, Sunshine JL, Plecha DM. COVID-19 Pandemic Impact on Decreased Imaging Utilization: A Single Institutional Experience. *Acad Radiol* 2020; **27**: 1204-1213 [PMID: [32665091](#) DOI: [10.1016/j.acra.2020.06.024](#)]
- 37 **Sprague BL**, O'Meara ES, Lee CI, Lee JM, Henderson LM, Buist DSM, Alsheik N, Macarol T, Perry H, Tosteson ANA, Onega T, Kerlikowske K, Miglioretti DL. Prioritizing breast imaging services during the COVID pandemic: A survey of breast imaging facilities within the Breast Cancer Surveillance Consortium. *Prev Med* 2021; **151**: 106540 [PMID: [34217424](#) DOI: [10.1016/j.ypmed.2021.106540](#)]
- 38 **Spuur KM**. The COVID-19 BreastScreen Department-beyond the pandemic. *J Med Radiat Sci* 2020; **67**: 352-355 [PMID: [33026711](#) DOI: [10.1002/jmrs.430](#)]
- 39 **Johnson MA**, Halloran K, Carpenter C, Pascual-Leone N, Parambath A, Sharma J, Seltzer R, Ellis HB, Shea KG, Ganley TJ. Changes in Pediatric Sports Injury Presentation During the COVID-19 Pandemic: A Multicenter Analysis. *Orthop J Sports Med* 2021; **9**: 23259671211010826 [PMID: [33997072](#) DOI: [10.1177/23259671211010826](#)]

Retrospective Study

Triple rule-out computed tomography angiography: Evaluation of acute chest pain in COVID-19 patients in the emergency department

Suzan Bahadir, Sonay Aydın, Mecit Kantarci, Edhem Unver, Erdal Karavas, Düzgün Can Şenbil

Specialty type: Radiology, nuclear medicine and medical imaging**Provenance and peer review:**

Invited article; Externally peer reviewed.

Peer-review model: Single blind**Peer-review report's scientific quality classification**Grade A (Excellent): 0
Grade B (Very good): 0
Grade C (Good): C, C
Grade D (Fair): D
Grade E (Poor): 0**P-Reviewer:** Luo W, China; Ren S, China**A-Editor:** Ferreira GSA, Brazil**Received:** April 11, 2022**Peer-review started:** April 11, 2022**First decision:** May 30, 2022**Revised:** May 30, 2022**Accepted:** August 5, 2022**Article in press:** August 5, 2022**Published online:** August 28, 2022**Suzan Bahadir**, Department of Radiology, Baskent University, Antalya 07000, Turkey**Sonay Aydın, Erdal Karavas, Düzgün Can Şenbil**, Department of Radiology, Erzincan Binali Yıldırım University, Erzincan 24100, Turkey**Mecit Kantarci**, Department of Radiology, Ataturk University, Erzurum 25100, Turkey**Edhem Unver**, Department of Chest Disease, Erzincan Binali Yıldırım University, Erzincan 24100, Turkey**Corresponding author:** Düzgün Can Şenbil, MD, Academic Research, Doctor, Department of Radiology, Erzincan Binali Yıldırım University, Hacı Ali Akın Street, Erzincan 24100, Turkey. can.senbil@erzincan.edu.tr**Abstract****BACKGROUND**

The aim of this study was to define clinical evidence supporting that triple rule-out computed tomography angiography (TRO CTA) is a comprehensive and feasible diagnostic tool in patients with novel coronavirus disease 2019 (COVID-19) who were admitted to the emergency department (ED) for acute chest pain. Optimizing diagnostic imaging strategies in COVID-19 related thromboembolic events, will help for rapid and noninvasive diagnoses and results will be effective for patients and healthcare systems in all aspects.

AIM

To define clinical evidence supporting that TRO CTA is a comprehensive and feasible diagnostic tool in COVID-19 patients who were admitted to the ED for acute chest pain, and to assess outcomes of optimizing diagnostic imaging strategies, particularly TRO CTA use, in COVID-19 related thromboembolic events.

METHODS

TRO CTA images were evaluated for the presence of coronary artery disease, pulmonary thromboembolism (PTE), or acute aortic syndromes. Statistical analyses were used for evaluation of significant association between the variables. A two tailed *P*-value < 0.05 was considered statistically significant.

RESULTS

Fifty-three patients were included into the study. In 31 patients (65.9%), there was

not any pathology, while PTE was diagnosed in 11 patients. There was no significant relationship between the rates of pathology on CTA and history of hypertension. On the other hand, the diabetes mellitus rate was much higher in the acute coronary syndrome group, particularly in the PTE group (8/31 = 25.8% *vs* 6/16 = 37.5%, $P = 0.001$). The rate of dyslipidemia was significantly higher in the group with pathology on CTA while compared to those without pathology apart from imaging findings of the pneumonia group (62.5% *vs* 38.7%, $P < 0.001$). Smoking history rates were similar in the groups. Platelets, D-dimer, fibrinogen, C-reactive protein, and erythrocyte sedimentation rate values were higher in COVID-19 cases with additional pathologies.

CONCLUSION

TRO CTA is an effective imaging method in evaluation of all thoracic vascular systems at once and gives accurate results in COVID-19 patients.

Key Words: COVID-19; Pulmonary thromboembolism; Coronary artery disease; Acute aortic syndromes; Triple rule-out computed tomography angiography

©The Author(s) 2022. Published by Baishideng Publishing Group Inc. All rights reserved.

Core Tip: Acute chest pain might be due to pneumonia itself or accompanying vascular events in novel coronavirus disease 2019 (COVID-19) cases. Triple rule-out computed tomography angiography (TRO CTA) is an effective and non-invasive diagnostic method in COVID-19 patients who were admitted to the emergency department with acute chest pain. TRO CTA is an imaging method that evaluates all thoracic vascular systems at once and gives accurate results in the COVID-19 patient group with acute chest pain, which has been proven to be susceptible to thrombotic events.

Citation: Bahadir S, Aydın S, Kantarci M, Unver E, Karavas E, Şenbil DC. Triple rule-out computed tomography angiography: Evaluation of acute chest pain in COVID-19 patients in the emergency department. *World J Radiol* 2022; 14(8): 311-318

URL: <https://www.wjgnet.com/1949-8470/full/v14/i8/311.htm>

DOI: <https://dx.doi.org/10.4329/wjr.v14.i8.311>

INTRODUCTION

Acute chest pain is one of the major complaints among the admissions to the emergency department (ED)[1,2]. In some patients, diagnoses can be made by electrocardiographic (ECG) changes, elevated cardiac laboratory biomarkers, and typical symptoms. However, a normal ECG or cardiac biomarkers do not rule out acute cardiovascular disease and symptoms might be atypical[3]. Moreover, after the novel coronavirus disease 2019 (COVID-19) pandemic, it has been more complicated to make a differential diagnosis list of acute chest pain in the ED. To date, many studies have presented that COVID-19 causes hypercoagulability[4]. Hypercoagulability is attributed to endothelial cell dysfunction, hypoxia-induced pathways, and increased blood viscosity[5]. Therefore, to make a rapid and accurate diagnosis in COVID-19 patients presenting with acute chest pain is of utmost importance.

Triple rule-out computed tomography angiography (TRO CTA) covers all thoracic vascular systems and has advantages in the detection of coronary artery disease, pulmonary thromboembolism (PTE), or acute aortic syndromes[6]. TRO CTA has ability to rule out pathology in all three vascular systems, particularly in COVID-19 patients who have already increased risk of thrombosis and myocardial injury [7].

The aim of this study was to define clinical evidence supporting that TRO CTA is a comprehensive and feasible diagnostic tool in patients with COVID-19 who were admitted to the ED for acute chest pain. Optimizing diagnostic imaging strategies in COVID-19 related thromboembolic events, will help for rapid and noninvasive diagnoses and results will be effective for patients and healthcare systems in all aspects.

MATERIALS AND METHODS

This study was approved by our Institutional Review Board and as it was a retrospective study, written informed consent was waived. No author has any conflict of interest to declare in this study. Our radiology archiving system was searched for patients who applied to the ED for acute chest pain and

underwent TRO CTA between September 2020 and January 2021. Patients older than 18 years, who had COVID-19 pneumonia and applied to the emergency department for acute chest pain, and underwent TRO CTA for further evaluation were included in this study. The exclusion criteria were as follows: Unreachable clinical or laboratory data and incomplete documentation of imaging data or inadequate imaging quality. Six of the patients were excluded from the study and the remaining 47 patients fulfilled the inclusion criteria. Medical records were used for the collection of demographics and clinical and laboratory findings. TRO CTA images were evaluated for the presence of the coronary artery disease, PTE, or acute aortic syndromes.

In our center, TRO CTA examination is performed according to the eligibility criteria in the article of Eltabbakh AR *et al*[8].

TRO-CTA protocol

All TRO CTA scans were acquired using a third-generation dual-source CT scanner (Somatom Force, Siemens Healthineers). The protocol begins with a noncontrast prospectively ECG-triggered acquisition between the levels of the carina and the base of the diaphragm for coronary artery calcium scoring. After this, CTA was acquired from the lung apices to the diaphragm after the administration of intravenous contrast. According to patients' condition, prospectively ECG-triggered, retrospectively ECG-gated, or prospectively ECG-triggered high pitch spiral acquisition was used. An intravenous iodinated contrast material of 60 to 90 mL was administered at an injection rate of 4 to 6 mL/s, followed by a saline chaser of 50 mL. Nitroglycerin or beta-blocker administration was not used. Primarily, the coronary arteries were opacified during image acquisition, while homogeneous enhancement of the pulmonary arteries happened. For the evaluation of the maximum intensity projection of the aorta, coronary and pulmonary arteries, curved planar and volume-rendered reconstructions were obtained; findings were then confirmed on the axial CT source images.

Statistical analysis

Data were analyzed using the Statistical Package for Social Sciences (SPSS) for Windows 20 software (IBM SPSS Inc., Chicago, IL, United States). Normal distribution of the data was evaluated using the Kolmogorov-Smirnov test. Numerical variables with a normal distribution are shown as minimum-maximum values. Categorical variables are shown as percentages. Differences in normally distributed variables between groups were evaluated using Student's *t*-test. Categorical variables were evaluated by the chi-square test between groups.

A two tailed *P*-value < 0.05 was considered statistically significant.

RESULTS

In this study, 53 patients who were previously diagnosed with laboratory-proven (real-time PCR) COVID-19 pneumonia and underwent triple rule-out computed tomography angiography due to sudden chest pain between September 2020-January 2021, were retrospectively searched. Six of these patients were excluded from the study because of insufficient quality of the images or because the necessary laboratory and/or clinical data could not be reached. The study population consisted of 47 patients. The creatinine values of 47 patients included in the study were within the physiological range.

Twenty-nine (61.7%) of 47 patients were men and 18 (38.3%) of them were women. Mean age was 61.7 ± 13.6 years and median age was 59 years (min-max: 47-84 years).

In 31 patients (65.9%), there was not any pathology except for parenchymal findings of COVID-19 pneumonia. PTE was diagnosed in 11 patients (Figure 1), significant stenosis in the coronary arteries diagnosed in 4 (Figures 2 and 3), and dissection in the descending aorta diagnosed in 1 (Figure 4). All coronary artery stenoses were observed in the left anterior descending artery and its branches. The patient with thoracic aortic dissection had a history of previous abdominal aortic dissection.

Forty-one (41/47, 87.2%) of the patients included in this study had a history of hypertension. All patients with hypertension were using antihypertensive drugs and blood pressures were under control. There was no significant relationship between the rates of pathology on CTA and history of hypertension. When patients with findings on CTA and those without findings other than COVID-19 pneumonia on CTA were compared, HT rates were similar (normal group 14/16, 87.5% *vs* pathologic group 27/31, 87%, *P* = 0.09).

Fourteen patients had a history of diabetes mellitus (DM) (14/47, 29.7%). Eight of these 14 patients were in the group with no imaging findings other than pneumonia, 5 of them were in the PTE group, and 1 was in the acute coronary syndrome group. When compared with those without any imaging findings other than pneumonia on CTA, the DM rate was much higher in the acute coronary syndrome group, particularly in the PTE group (8/31 = 25.8% *vs* 6/16 = 37.5%, *P* = 0.001).

Dyslipidemia was detected in the blood test taken just before (1-3 d) the CTA examination in 22 (22/47, 46.8%) patients. Nine of these patients also had a history of DM. Fourteen of these patients were previously aware of the history of hypercholesterolemia and were using statin derivatives.



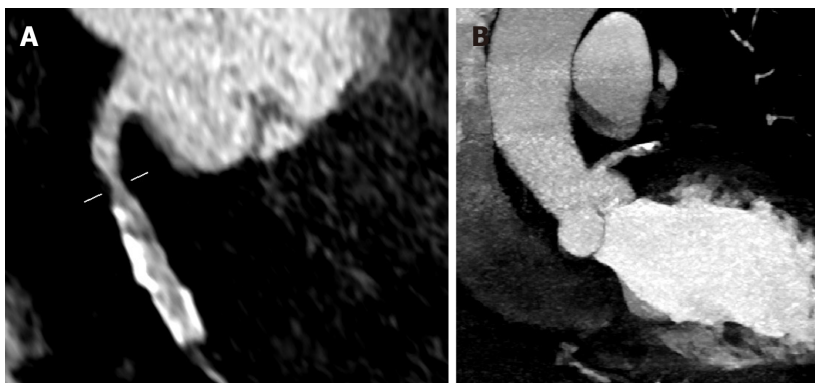
DOI: 10.4329/wjr.v14.i8.311 Copyright ©The Author(s) 2022.

Figure 1 A 77-year-old male patient. Curved multiplanar reformatted image shows embolus in the right lung lower lobe artery (arrow).



DOI: 10.4329/wjr.v14.i8.311 Copyright ©The Author(s) 2022.

Figure 2 A 73-year-old male patient. A: Diffuse calcific and soft plaque formations are seen in the left main, left anterior descending (LAD), and left circumflex arteries on axial maximum intensity projection image; B: Moderate stenosis (50% to 69%) is present (linear marker) in the proximal segment of LAD on curved multiplanar reformatted image.



DOI: 10.4329/wjr.v14.i8.311 Copyright ©The Author(s) 2022.

Figure 3 A 63-year-old female patient. A: Moderate stenosis (50% to 69%; linear marker); B: Calcific plaque formations are seen in the right coronary artery on coronal maximum intensity projection images.

The mean total cholesterol level of these patients was 243.9 ± 71.2 mg/dL, and the low-density lipoprotein cholesterol level was 171.5 ± 42.6 mg/dL. All of the patients with significant findings on TRO CTA had a total cholesterol level above 240 mg/dL and low-density lipoprotein cholesterol level above 175 mg/dL. Twelve of these 22 patients were in the group without imaging findings other than pneumonia, 7 were in the PTE detected group, 2 were in the acute coronary syndrome group, and 1 was in the group with aortic dissection. The rate of dyslipidemia was significantly higher in the group with pathology on CTA while compared to those without pathology apart from imaging findings of the



DOI: 10.4329/wjr.v14.i8.311 Copyright ©The Author(s) 2022.

Figure 4 A 78-year-old male patient. Sagittal maximum intensity projection image depicts Stanford type B dissection.

pneumonia group (10/16 = 62.5% *vs* 12/31 = 38.7%, $P < 0.001$).

Nine of the patients included in this study (9/47, 19.1%) had a smoking history. There was not any significant relationship between smoking history and the rate of pathology detected using TRO CTA. Smoking history rates were similar in the group who had pathology on CTA, compared to those without pathology apart from imaging findings of the pneumonia group (3/16 = 18.7%, 6/31 = 19.3%, $P < 0.08$).

Two patients (2/47, 4.2%) had a history of cancer (breast cancer and lymphoma). There was not any pathology except for imaging findings of pneumonia detected on CTA in these patients.

The mean PLT value of the whole population was 231.99 ± 64.15 ($\times 10^9/L$), the D-dimer value was 854.75 ± 347.65 $\mu g/L$, the fibrinogen value was 333.05 ± 66.3 mg/dL, the C-reactive protein (CRP) value was 37.31 ± 2.01 mg/dL, and the erythrocyte sedimentation rate (ESR) value was 55.9 ± 8.2 mm/h (Table 1).

DISCUSSION

Our study revealed that TRO CTA is an effective and non-invasive diagnostic method in COVID-19 patients who were admitted to the ED with acute chest pain. Acute chest pain might be due to pneumonia itself or accompanying vascular events which are related to an increased risk of thrombosis, endothelial dysfunction, and myocardial injury in COVID-19 cases[5,7,8].

TRO CTA accelerates the precise diagnosis and utilizes the evaluation of the aorta, coronary arteries, and pulmonary vascular systems with a single examination for safe and rapid decisions[9]. However, it requires a larger amount of contrast medium and higher radiation dose, and might not be easily reachable in all centers[10]. But still instead of separate examinations, it is plausible to choose TRO CTA not only for acute thoracic vascular emergencies but for parenchymal pathologies in COVID-19 patients. Because the correct diagnosis of PTE, acute coronary syndrome, and aortic dissection, influences early treatment and thus, it is life-saving[11].

It has been previously emphasized that COVID-19 increases the risk for pulmonary thromboembolic events, so the thromboprophylaxis is suggested to prevent PTE[12]. Being a common cause of acute chest pain, coronary vascular pathologies can be encountered as a potential differential diagnosis for COVID-19. In addition to being an alternative diagnosis, coronary vascular pathologies can also increase the mortality of COVID-19 cases[13]. The results of the current study demonstrated that pathologies that can be easily diagnosed *via* the TRO CTA method, such as PTE and coronary vascular pathologies, were also frequently encountered in COVID-19 cases. Therefore, easy, accurate, and rapid diagnosis of accompanying pathologies can help guide treatment and reduce mortality/morbidity rates. Moreover, the effective use of TRO CTA in the ED can enable clinicians to both detect comorbidities and eliminate the mimickers of COVID-19 pneumonia.

Performing TRO CTA in every patient with acute chest pain might be challenging and it will not be a cost-effective method. According to our results, accompanying pathologies were mostly seen in COVID-19 patients with DM and dyslipidemia. These data can help the clinicians to select the more eligible patients for TRO CTA examinations. In addition to clinical properties, laboratory parameters can also help to define suitable patients. We showed that PLT, D-dimer, fibrinogen, CRP, and ESR values were higher in COVID-19 cases with additional pathologies other than pneumonia. The relationship between D-dimer and fibrinogen levels with thromboembolic events, and the relationship between CRP/ESR levels with severity of inflammation and the course of disease were previously studied for COVID-19 cases[14]. Hence, it would be a wise choice to prefer TRO CTA examinations in cases with severe

Table 1 Mean values and statistical significance according to subgroups

	Normal group	Pathological group	P value
PLT ($\times 10^9/L$)	202.18 \pm 45.59	289.75 \pm 109.68	0.003
D-Dimer ($\mu g/L$)	651.53 \pm 167.71	1248.49 \pm 520.11	0.001
Fibrinogen (mg/dL)	307.49 \pm 61	382.59 \pm 80.1	0.002
CRP (mg/dL)	28.75 \pm 3.02	53.91 \pm 2.2	0.001
ESR (mm/hr)	43.1 \pm 7.3	81.23 \pm 12.2	0.003

inflammation and who are prone to thromboembolic events.

To the best of our knowledge, there is no research to date that has examined the TRO CTA findings in COVID-19 cases and related them to the clinical features. By examining the TRO CTA findings, performed in the emergency setting of COVID-19 cases, the current study might increase the awareness about the diagnostic utility and effectiveness of the technique, and increase its use.

The limitations of this study are that it is a retrospective single-center study with a small sample size. Although our center is a third-level university hospital and has a wide variety of facilities, future studies in larger populations are required to support the use of TRO CTA in COVID-19 patients with acute chest pain. Subsequently in times to come, our findings should be confirmed in well-powered clinical studies in multicenter hospitals. Since our study was retrospective, ECG data of some patients could not be accessed.

CONCLUSION

Our study has shown that TRO CTA is an imaging method that evaluates all thoracic vascular systems at once and gives accurate results in the COVID-19 patient group with acute chest pain, which has been proven to be susceptible to thrombotic events.

ARTICLE HIGHLIGHTS

Research background

The aim of this study was to define clinical evidence supporting that triple rule-out computed tomography angiography (TRO CTA) is a comprehensive and feasible diagnostic tool in patients with novel coronavirus disease 2019 (COVID-19) who were admitted to the emergency department for acute chest pain. Optimizing diagnostic imaging strategies in COVID-19 related thromboembolic events, will help for rapid and noninvasive diagnoses and results will be effective for patients and healthcare systems in all aspects.

Research motivation

Acute chest pain in COVID 19 patients becomes more difficult due to increasing differential diagnosis. TRO CTA helps diagnosis by excluding pulmonary thromboembolism (PTE), coronary artery disease, and acute aortic syndrome at the same time.

Research objectives

To decrease the morbidity and mortality rates in patients.

Research methods

Our study is a retrospective study.

Research results

No pathology was detected in 31 of 57 patients included in the study. PTE was detected in 11 patients. The diabetes mellitus rate was much higher in the acute coronary syndrome group, particularly in the PTE group. The rate of dyslipidemia was significantly higher in the group with pathology on CTA while compared to those without pathology apart from imaging findings of the pneumonia group

Research conclusions

TRO CTA can be a useful method in the differential diagnosis of COVID-19 patients who present to the emergency department with chest pain.

Research perspectives

The use of TRO CTA will reduce mortality and morbidity as it will accelerate the diagnosis and treatment process in the future. Studies will proceed in this direction.

FOOTNOTES

Author contributions: Aydın S, Bahadır S, Kantarcı M, and Karavas E designed the research study; Bahadır S, Ünver E, Şenbil DC, and Karavas E performed the research; Aydın S and Bahadır S contributed new reagents and analytic tools; Aydın S, Karavas E, and Şenbil DC analyzed the data and wrote the manuscript; all authors have read and approved the final manuscript.

Institutional review board statement: This study was approved by our Institutional Review Board (Erzincan Binali Yıldırım University Faculty of Medicine protocol number kaek-ebyu-2020/03/14) and as it was a retrospective study, written informed consent was waived.

Informed consent statement: Patients were not required to give informed consent to the study because the analysis used anonymous clinical data that were obtained after each patient agreed to treatment by written consent.

Conflict-of-interest statement: No author has any conflict of interest to declare in this study.

Data sharing statement: No additional data are available.

Open-Access: This article is an open-access article that was selected by an in-house editor and fully peer-reviewed by external reviewers. It is distributed in accordance with the Creative Commons Attribution NonCommercial (CC BY-NC 4.0) license, which permits others to distribute, remix, adapt, build upon this work non-commercially, and license their derivative works on different terms, provided the original work is properly cited and the use is non-commercial. See: <https://creativecommons.org/licenses/by-nc/4.0/>

Country/Territory of origin: Turkey

ORCID number: Suzan Bahadır 0000-0002-0019-5851; Sonay Aydın 0000-0002-3812-6333; Mecit Kantarcı 0000-0002-1043-6719; Edhem Ünver 0000-0002-0322-8102; Erdal Karavas 0000-0001-6649-3256; Düzgün Can Şenbil 0000-0003-0233-7371.

S-Editor: Wang LL

L-Editor: Wang TQ

P-Editor: Wang LL

REFERENCES

- 1 **Backus BE**, Six AJ, Kelder JH, Gibler WB, Moll FL, Doevendans PA. Risk scores for patients with chest pain: evaluation in the emergency department. *Curr Cardiol Rev* 2011; **7**: 2-8 [PMID: 22294968 DOI: 10.2174/157340311795677662]
- 2 **Lee TH**, Goldman L. Evaluation of the patient with acute chest pain. *N Engl J Med* 2000; **342**: 1187-1195 [PMID: 10770985 DOI: 10.1056/NEJM200004203421607]
- 3 **Pope JH**, Aufderheide TP, Ruthazer R, Woolard RH, Feldman JA, Beshansky JR, Griffith JL, Selker HP. Missed diagnoses of acute cardiac ischemia in the emergency department. *N Engl J Med* 2000; **342**: 1163-1170 [PMID: 10770981 DOI: 10.1056/NEJM200004203421603]
- 4 **Tang N**, Li D, Wang X, Sun Z. Abnormal coagulation parameters are associated with poor prognosis in patients with novel coronavirus pneumonia. *J Thromb Haemost* 2020; **18**: 844-847 [PMID: 32073213 DOI: 10.1111/jth.14768]
- 5 **Gupta N**, Zhao YY, Evans CE. The stimulation of thrombosis by hypoxia. *Thromb Res* 2019; **181**: 77-83 [PMID: 31376606 DOI: 10.1016/j.thromres.2019.07.013]
- 6 **Lee HY**, Yoo SM, White CS. Coronary CT angiography in emergency department patients with acute chest pain: triple rule-out protocol vs dedicated coronary CT angiography. *Int J Cardiovasc Imaging* 2009; **25**: 319-326 [PMID: 18853277 DOI: 10.1007/s10554-008-9375-4]
- 7 **Zhou F**, Yu T, Du R, Fan G, Liu Y, Liu Z, Xiang J, Wang Y, Song B, Gu X, Guan L, Wei Y, Li H, Wu X, Xu J, Tu S, Zhang Y, Chen H, Cao B. Clinical course and risk factors for mortality of adult inpatients with COVID-19 in Wuhan, China: a retrospective cohort study. *Lancet* 2020; **395**: 1054-1062 [PMID: 32171076 DOI: 10.1016/S0140-6736]
- 8 **Eltabbakh AR**, Dawoud MA, Langer M, Moharm MA, Hamdy EA, Hamisa MF. 'Triple-rule-out' CT angiography for clinical decision making and early triage of acute chest pain patients: use of 320-multislice CT angiography. *Egypt J Radiol Nuc M* 2019; **50**: 1-10 [DOI: 10.1186/s43055-019-0003-1]
- 9 **Chae MK**, Kim EK, Jung KY, Shin TG, Sim MS, Jo IJ, Song KJ, Chang SA, Song YB, Hahn JY, Choi SH, Gwon HC, Lee SH, Kim SM, Eo H, Choe YH, Choi JH. Triple rule-out computed tomography for risk stratification of patients with acute chest pain. *J Cardiovasc Comput Tomogr* 2016; **10**: 291-300 [PMID: 27375202 DOI: 10.1016/j.jcct.2016.06.002]
- 10 **Yoon YE**, Wann S. Evaluation of acute chest pain in the emergency department: "triple rule-out" computed tomography angiography. *Cardiol Rev* 2011; **19**: 115-121 [PMID: 21464639 DOI: 10.1097/CRD.0b013e31820f1501]

- 11 **Takx RAP**, Wichmann JL, Otani K, De Cecco CN, Tesche C, Baumann S, Mastrodicasa D, Litwin SE, Bayer RR 2nd, Nance JW, Suranyi P, Jacobs BE, Duguay TM, Vogl TJ, Carr CM, Schoepf UJ. In-Hospital Cost Comparison of Triple-Rule-Out Computed Tomography Angiography Versus Standard of Care in Patients With Acute Chest Pain. *J Thorac Imaging* 2020; **35**: 198-203 [PMID: 32032251 DOI: 10.1097/RTI.0000000000000474]
- 12 **Sakr Y**, Giovini M, Leone M, Pizzilli G, Kortgen A, Bauer M, Tonetti T, Duclos G, Zieleskiewicz L, Buschbeck S, Ranieri VM, Antonucci E. Pulmonary embolism in patients with coronavirus disease-2019 (COVID-19) pneumonia: a narrative review. *Ann Intensive Care* 2020; **10**: 124 [PMID: 32953201 DOI: 10.1186/s13613-020-00741-0]
- 13 **Dan S**, Pant M, Upadhyay SK. The Case Fatality Rate in COVID-19 Patients With Cardiovascular Disease: Global Health Challenge and Paradigm in the Current Pandemic. *Curr Pharmacol Rep* 2020; 1-10 [PMID: 32953401 DOI: 10.1007/s40495-020-00239-0]
- 14 **Eljilany I**, Elzouki AN. D-Dimer, Fibrinogen, and IL-6 in COVID-19 Patients with Suspected Venous Thromboembolism: A Narrative Review. *Vasc Health Risk Manag* 2020; **16**: 455-462 [PMID: 33223833 DOI: 10.2147/VHRM.S280962]



Published by **Baishideng Publishing Group Inc**
7041 Koll Center Parkway, Suite 160, Pleasanton, CA 94566, USA
Telephone: +1-925-3991568
E-mail: bpgoffice@wjgnet.com
Help Desk: <https://www.f6publishing.com/helpdesk>
<https://www.wjgnet.com>

